

Description of coherent elastic neutrino-nucleus scattering cross sections



Samuel Thierry WAUTHIER

Supervisor: Prof. R. Raabe
KU Leuven

Co-supervisor: *Prof. N. Jachowicz*
UGent

Mentor: *N. Van Dessel*
UGent

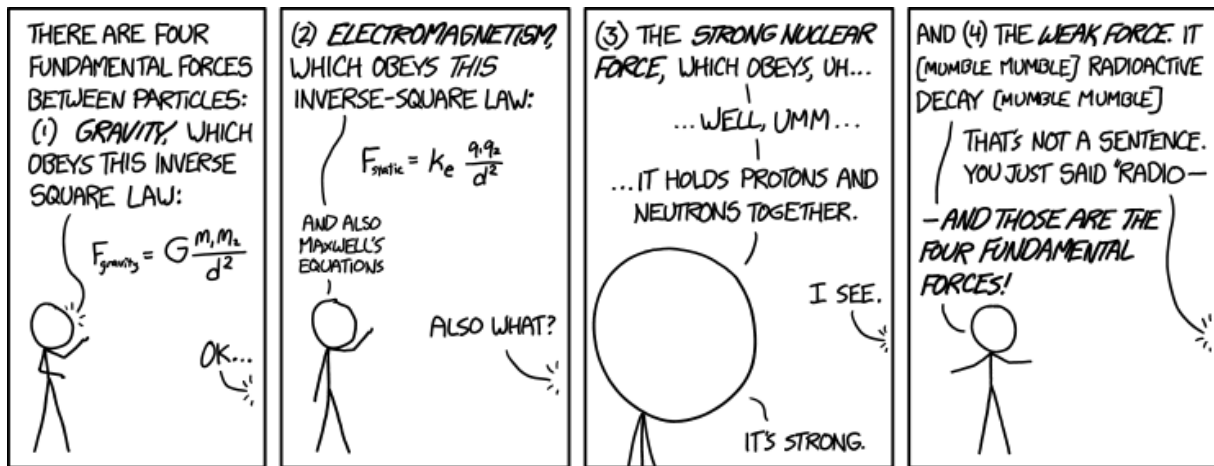
Thesis presented in
fulfillment of the requirements
for the degree of Master of Science
in Physics

Academic year 2016-2017

© Copyright by KU Leuven

Without written permission of the promotors and the authors it is forbidden to reproduce or adapt in any form or by any means any part of this publication. Requests for obtaining the right to reproduce or utilize parts of this publication should be addressed to KU Leuven, Faculteit Wetenschappen, Geel Huis, Kasteelpark Arenberg 11 bus 2100, 3001 Leuven (Heverlee), Telephone +32 16 32 14 01.

A written permission of the promotor is also required to use the methods, products, schematics and programs described in this work for industrial or commercial use, and for submitting this publication in scientific contests.



“Of these four forces, there’s one we don’t really understand.” “Is it the weak force or the strong-” “It’s gravity.”

Contents

Preface	v
Summary	vi
Summary in layman's terms	viii
Abbreviations	ix
Symbols	xi
1 Introduction	1
1.1 Coherent elastic neutrino-nucleus scattering	2
1.2 CE ν NS detection	3
1.2.1 Neutrino sources	3
1.2.2 CE ν NS experiments	6
1.3 Supernova neutrinos	8
1.4 Standard Model tests	10
1.5 Outline	11
2 Neutrino-nucleus cross sections	12
2.1 Electroweak sector of the SM	13
2.2 Charged scalar QED	14
2.3 CE ν NS cross section	16
2.4 Nuclear form factor	19
2.5 Other neutrino-nucleus reaction channels	20
2.5.1 Neutral current quasielastic scattering	20
2.5.2 Charged current quasielastic scattering	22
3 Description of the nucleus	23
3.1 Hartree-Fock method	24
3.2 Random phase approximation	26
3.3 Interactions and potentials	28
3.3.1 Skyrme interaction	28
3.3.2 Woods-Saxon	31
4 Properties of CEνNS	33
4.1 Maximum recoil energy	34
4.2 Influence of nuclear parameters	35

4.2.1	Mass and weak charge	35
4.2.2	Form factor	37
4.2.3	Combined results	39
4.2.4	Woods-Saxon vs. Hartree-Fock + SkE2	42
4.2.5	Influence of RPA effects	42
4.2.6	Comparison with literature	44
4.3	Comparison to other interactions	46
4.4	Sensitivity to the weak mixing angle	48
5	Conclusion and future prospects	51
A	Evaluation of $\mathcal{M} ^2$	53
B	Derivation of $\frac{d\sigma}{dq^2}$	55
C	Second quantization formalism	56
C.1	Many-body states	56
C.2	Operators	57
	Bibliography	58

Preface

This thesis is the denouement of years of hard work. It was accomplished through the expertise, motivation and support of a great number of people. As such, I find it of the utmost importance that these people receive a word of thanks.

First and foremost, I would like to thank my supervisors, prof. Riccardo Raabe and prof. Natalie Jachowicz, for the opportunity to work on neutrinos in collaboration with the department of physics and astronomy at UGent and allowing me to choose a topic of my liking. I am also very grateful to Nils van Dessel for committing so much of his time to me and for putting up with my countless questions. Furthermore, I would like to thank prof. Nathal Severijns and prof. Hugues Sana for taking the time to read this thesis.

I want to express my gratitude to my family for believing in me these years as a student and all the ones before it, in particular, my father for being someone I can look up to, my mother for mental support and my sister for her interest in what I do. Also a big ‘thank you’ to all the cousins, aunts and uncles who’ve helped me out whenever I needed help and showed interest in my topic.

My years in Leuven wouldn’t have been complete without the people I met along the way. Alexis, Bram, Bob, Jeroen, Koen, Simon and Vincent (ordered alphabetically to avoid jealousy), the times we spent together were some of the greatest, the discussions where we excluded anyone that didn’t know a thing about physics, the birthdays where we gifted each other stuff we would never need, the holidays we spent together and many more. I enjoyed how different we all were and how, collectively, our interests spanned most of humanity’s knowledge. Thank you for the motivation and help, without which my studies would have been significantly more difficult. Furthermore, a big thanks to Marta, who delivered the much needed trash talk and less needed nerdiness to keep my wits sharp and my batman alive. Finally, I want to thank my girlfriend, María, for taking care of me and being there when I needed her. Thank you for making the past year immensely more bearable.

I must thank all my friends from my past lives. Dieter, my friendship with whom has lasted for many countries. Our initial rivalry has brought me to the point of finalizing my Master’s degree. Camiel, Manu, Esmée and Dimi, thank you for the motivation you have given me.

Last, but not least, I would like to thank Kamiel for the sick, nasty carrying, Ben for feeding the enemy and Sybren for raging at bad teammates so that no one else had to.

A last thanks goes out to Yasmine Wauthier for the picture on the cover.

June 11, 2017
Samuel Wauthier

Summary

Coherent elastic neutrino nucleus scattering (CE ν NS) is the scattering of neutrinos off nuclei as a whole. In this process, the neutrino loses kinetic energy, while the nucleus recoils and is left in its ground state. This reaction channel has never been observed due to the fact that the recoil energy of the nucleus is very small. In addition, it is only possible to measure the recoil, since no additional particles are created and detection of the scattered neutrino is virtually impossible. On the other hand, the predicted cross section for CE ν NS is larger than other neutrino-nucleus reaction channels at low energies. This makes it an important interaction to study.

CE ν NS is expected to play a big role in core-collapse supernova. As the iron core of the progenitor star shrinks and becomes denser, neutrinos become less likely to escape. The point at which the collapse halts likely depends on neutrino-nucleus interactions. Likewise, neutrinos diffusing out of the hot core are free to deposit their energy into the stellar matter above. This causes neutrino-driven winds. In this case, neutrino-nucleus interactions are essential for energy transfer to the stellar matter.

Since the CE ν NS cross section is cleanly predicted by the Standard Model (SM), it can be used for tests of the SM. In addition, the existence of non-standard interactions (NSI), interactions beyond the SM, can also be researched. Other applications include neutrino magnetic moment investigation and nuclear form factor probing.

The CE ν NS cross section can be calculated using quantum field theory. In this work, the nucleus is assumed spherically symmetric and even-even, so that its ground state is $J^\pi = 0^+$. The incoming particle can be either a neutrino or antineutrino of any flavor. The cross section then includes a form factor F in order to account for underlying physics. This form factor can be calculated in any model for the nucleus. The wave functions were calculated through (i) the Hartree-Fock (HF) method with an extended Skyrme interaction (SkE2 parametrization), (ii) the Woods-Saxon (WS) potential and (iii) the HF+SkE2 method with occupation numbers from an extended random phase approximation (RPA).

The maximum recoil energy for ^{12}C , ^{16}O , ^{40}Ar , ^{40}Ca and ^{56}Fe was calculated as a function of the energy of the neutrino. This has shown that the maximum recoil increases with neutrino energy. Moreover, the lighter nuclei gave larger values for the same neutrino energy.

The effect of nuclear parameters on the cross section was demonstrated. The cross section is larger for heavier nuclei. In addition, sensitivity to the neutron number was illustrated. Comparison of the nuclear models showed that the cross section is larger for the WS model than for HF+SkE2. The extended RPA results did not differ much from the HF ones. The cross sections calculated in HF+SkE2 corresponded rather well with literature.

The $\text{CE}\nu\text{NS}$ cross section was compared with neutral- and charged-current quasielastic neutrino-nucleus scattering. $\text{CE}\nu\text{NS}$ showed to be larger for energies up to around 60 MeV for ^{12}C , ^{16}O , ^{40}Ar and ^{40}Ca .

Sensitivity of the $\text{CE}\nu\text{NS}$ interaction to the weak mixing angle was demonstrated. The cross section was calculated for different values of $\sin^2\theta_W$. The differences were likely not distinguishable for experiments.

Summary in layman's terms

In the mid-1900s, physicists developed the Standard Model of particle physics. This model aimed to describe the four known fundamental forces. These forces are: the two that everyone knows, i.e. gravity and electromagnetism, the one that holds nuclei together, i.e. the strong nuclear force, and the one that causes nuclear decay, i.e. the weak nuclear force. In its final form in the 1970s, the Standard Model was very successful in providing experimental predictions. It led to the discovery of a number of other particles, including the elusive Higgs boson.

Despite its success, the Standard Model leaves certain phenomena unexplained. For example, it does not incorporate a theory of gravity. Additionally, experimental data on particle interactions, properties, etc. can be difficult to acquire due to the requirement of advanced or specialized detector technology. To put this into perspective, it took 60 years before technology was advanced enough to confirm the existence of the Higgs boson.

Neutrinos and their antiparticles, antineutrinos, are examples of particles that are very difficult to detect. The reason that they are slippery is that their only ways of interacting are the weak nuclear force and gravity. In other words, they cannot be detected through the methods used for protons, neutrons, photons, etc. Furthermore, the weak nuclear force and gravity are very weak in comparison to electromagnetism, meaning that their effect on individual particles is very small. To top it all off, the range of the former is very small, so that an interaction can only happen if two particles come in extremely close proximity of each other. As a consequence, lots of neutrinos fly through the earth every second without ever interacting with another particle.

Nevertheless, it is possible to detect neutrinos and antineutrinos. The fact that there are so many flying around means that occasionally one will come close enough to another particle to cause an interaction. The way the neutrino interacts depends on its target, the flavor of the neutrino and the energy of the neutrino and the target. For example, the neutrino could scatter off an electron or be absorbed by a neutron to form a proton and an electron.

It is possible for neutrinos to scatter off nuclei. Since, generally, nuclei consist of many particles, there are many possible ways for the neutrino to interact. In this work, we deal with the scattering of neutrinos and antineutrinos off nuclei as a whole. This means the neutrino acts on all the nucleons equally and the nucleus can be considered as a single particle. Coherent elastic neutrino-nucleus scattering, as this type of interaction is called, is the most likely interaction for a low-energy neutrino incident on a nucleus. It is important in the evolution of supernovae and for tests of the Standard Model. This dissertation explores some of the properties of this interaction.

Abbreviations

$\overline{\text{MS}}$ modified minimal subtraction

AGN Active Galactic Nuclei

BCS Bardeen-Cooper-Schrieffer

BNB Booster Neutrino Beam

CCQE charged current quasielastic

CE ν NS coherent elastic neutrino-nucleus scattering

CENNS Coherent Elastic Neutrino-Nucleus Scattering

CKM Cabibbo-Kobayashi-Maskawa

CLEAN Cryogenic Low Energy Astrophysics with Noble gases

HF Hartree-Fock

IVB intermediate vector boson

KSNL Kuo-Sheng Neutrino Laboratory

NCQE neutral current quasielastic

NINs neutrino induced neutrons

NSI non-standard interactions

ORNL Oak Ridge National Laboratory

PDG Particle Data Group

PNS protoneutron star

PPC p-type point-contact

QED quantum electrodynamics

r-process rapid neutron capture process

RPA random phase approximation

SM Standard Model

SNS Spallation Neutron Source

TDDM time-dependent density-matrix

TEXONO Taiwan EXperiment On Neutrino

ULEGe Ultra-Low-Energy Germanium

WIMP Weakly Interacting Massive Particle

WS Woods-Saxon

Symbols

G_F Fermi constant ($= 1.1663787 \times 10^{-5} \text{ GeV}^{-2}$ [1])

\hbar reduced Planck constant ($= 1.054571800 \times 10^{-34} \text{ m}^2\text{kg/s}$ [1]) (in this work: $\hbar = 1$)

θ_W weak mixing angle ($\sin^2 \theta_W = 0.2223$ [1])

c speed of light ($= 299792458 \text{ m/s}$ [1]) (in this work: $c = 1$)

e elementary electric charge ($1.6021766208 \times 10^{-19} \text{ C}$ [1])

g weak coupling constant

1 | Introduction

Up to this day, a lot of questions remain about neutrinos. “What are their masses?” “Do sterile neutrinos exist?” “Are they Majorana particles?” And many more. The fact that they only interact through the weak interaction means they fly through large objects such as the earth with ease. The consequences of this are two-sided. It allows us to examine environments in space that are too dense for other particles to travel through, high density environments, where the world of neutrinos is a lot more engaging. Yet, it elicits the same phenomenon in detectors, making neutrino physics considerably difficult and finding answers to the aforementioned questions substantially challenging.

This chapter serves as a first acquaintance with coherent elastic neutrino-nucleus scattering. We explain the experimental difficulties and situate the importance of this interaction within modern physics.

1.1 Coherent elastic neutrino-nucleus scattering

A neutrino can induce several reaction processes. The reaction channel depends on the energy of the neutrino, the type of matter it encounters and the state the matter is in, i.e. whether it is bound or free. To illustrate this, envisage a neutrino interacting with a nucleus. This particle could interact with the quarks in the nucleus, it could interact with a nucleon as a whole or it could even interact with the nucleus as a whole.

In this thesis, the main focus lies on the elastic scattering of neutrinos off atomic nuclei as a whole. This is known as coherent elastic neutrino-nucleus scattering (CE ν NS)¹. At the tree level, the reaction can be represented by the exchange of a virtual Z -boson between the neutrino and the nucleus (Fig. 1.1). The consequence is that the neutrino loses some of its kinetic energy and momentum, but more importantly, the nucleus recoils and is left in its ground state.

Unfortunately, CE ν NS has never been observed [2,3]. It is extremely difficult to detect for a few reasons. Foremost, current detectors do not perform well enough. The recoil energy of the nucleus is rather small (\sim keV) as a result of the exceedingly small neutrino mass. Distinguishing the small signals over the large backgrounds has turned out to be quite troublesome. Secondly, in order to obtain high count rates, it is necessary to have strong neutrino sources [2]. Furthermore, the choice of detector material has an influence on the recoil energy, as well as on the count rates. Heavy nuclei give smaller recoil energies, but larger cross sections, thus higher count rates. The use of heavy materials in detectors can thus be both a blessing and a burden.

CE ν NS's appeal lies in its cross section. Its predicted cross section is larger than that of other neutrino-nucleus interactions at energies up to about 50 MeV. This makes it important in models that incorporate neutrinos in this energy range at high density. Specifically in supernova dynamics, CE ν NS is expected to have a big impact, since typical neutrino energies in supernova type-II conditions lie around 20 MeV (section 1.3). In addition, the fact the cross section is cleanly predicted by the Standard Model (SM) indicates that it is valuable for tests of the SM and so-called non-standard interactions (NSI) (section 1.4). Further applications include nuclear form factor probing and neutrino

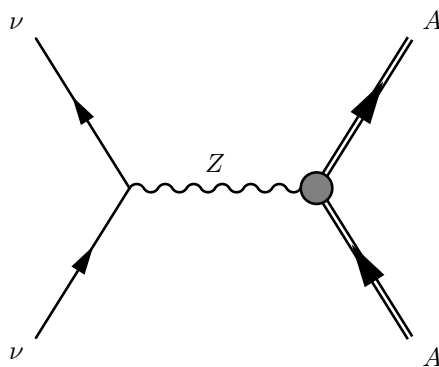


Figure 1.1: Basic diagram of the CE ν NS interaction.

¹The pronunciation of this abbreviation has been declared by the community to be “sevens”.

magnetic moment investigation [3].

In order to research neutrinos accurately, it is important to understand the way they interact with their surroundings, especially with their target material. We may ask ourselves how, in a theoretical approach, the interaction will change depending on the model of the target material, or more specifically, the nuclei inside the target material. An answer to this question may help build and expand upon models of supernova dynamics or help in the construction of neutrino detectors. To this end, the aim of this work is to provide a description of the CE ν NS interaction and characterize the interaction with different even-even nuclei.

1.2 CE ν NS detection

Neutrino sources are abundant in the universe, neutrino detectors not so much. The current issue with experiments is that the particles do not interact strongly. This means neutrinos are hard to detect and count rates in experiments are low. Two obvious solutions are: improving detectors and finding suitable sources.

A good neutrino detector has several properties, such as high sensitivity, good energy resolution, a robust way to deal with background and a way to identify detected particles. The detector can be improved by enhancing these properties. Detection through CE ν NS offers high sensitivity and high count rates in the 0-50 MeV region through a relatively large cross section, since the CE ν NS cross section is larger than other charged-current and neutral-current cross sections in the low energy range [3]. A detector using the CE ν NS principle would therefore be more sensitive than existing detectors. In fact, it would be sensitive to all types of neutrinos [4]. Moreover, it would allow for direct measurement of the neutrino energy through analysis of the nuclear recoil [4]. It is important to note, however, that only the nuclear recoil is measurable, since no particles are emitted in the interaction².

A suitable neutrino source, in general, must provide a high count rate through large particle flux. Some additional desiderata for a good source for CE ν NS are: a well-understood spectrum, multiple flavors to test new physics and a pulsed beam for background rejection [3]. Keep in mind that not only the CE ν NS cross section increases with increasing neutrino energy (section 2.3), but also the maximum recoil energy ([3], section 4.1). It is, therefore, convenient to have a source that emits neutrinos in the upper half of the 0-50 MeV range, since the count rate will be higher and the recoil of the nucleus will be easier to detect. Both natural and artificial sources exist, examples of this are the sun and nuclear reactors, respectively [3].

1.2.1 Neutrino sources

Stopped pions

Stopped-pion sources are created by bombarding protons on a heavy nuclear target. This method is traditionally used to produce neutrons, but can also be used to make pions. The pions that are generated in the bombardment are stopped in the target material in a

²Apart from the scattered neutrino, which, generally, cannot be detected.

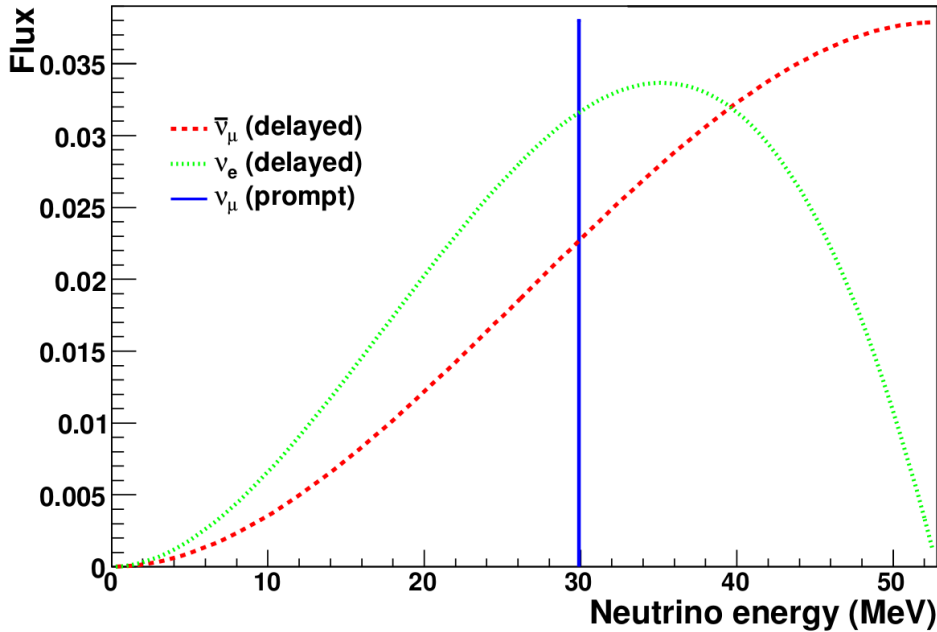


Figure 1.2: Stopped-pion neutrino spectrum. Figure taken from [3].

matter of 10^{-10} s. The negative pions are captured and absorbed by nuclei, while positive pions are slowed down and decay at rest [5].

The decay process is as follows. The pion with a mean lifetime of $\tau_\pi = 26$ ns decays through:

$$\pi^+ \rightarrow \mu^+ + \nu_\mu. \quad (1.1)$$

The positive muon with a mean lifetime of $\tau_\mu = 2.2$ μ s, subsequently, decays as well:

$$\mu^+ \rightarrow e^+ + \nu_e + \bar{\nu}_\mu. \quad (1.2)$$

The first decay is a two-particle decay and produces a monoenergetic muon-neutrino with energy $E_{\nu_\mu} = 29.8$ MeV. The second decay is a three-particle decay and thus produces a spectrum of electron-neutrinos and muon-antineutrinos with energies up to 52.8 MeV. Note that the quantity of neutrinos produced per pion is the same for each flavor. Therefore, the flux is the same for each flavor (at Spallation Neutron Source (SNS), e.g. total flux $\sim 10^{15}$ /s) [3, 5, 6].

With regards to CE ν NS, the energy of the emitted neutrinos has the desired spectrum, i.e. energies in the upper half of the 0-50 MeV range. In this range, the largest fraction of neutrinos will interact through CE ν NS, while the nuclei will have larger recoil energies (> 1 keV) than in the lower half of the 0-50 MeV range. Additionally, the technique allows for pulsed neutrino patterns, which is beneficial for background reduction.

Reactors

Another source of neutrinos is nuclear reactors. Reactors produce a steady stream of large amounts of neutrinos due to the decay of the fission products. The resulting flux is around 2×10^{20} /GW per second. The flow consists almost entirely of electron-neutrinos with energies up to around 7 MeV [3].

Reactors have the advantage of having a high particle flux. However, the single flavor and low energy character of the neutrinos are less favorable for CE ν NS experiments. The low energy means neutrinos will be harder to detect, since the recoil energies of the nuclei will lie in sub-keV region. Stopped-pion sources seem more favorable owing to this [3].

Natural sources

Natural sources of neutrinos include geoneutrinos, low energy atmospheric neutrinos, solar neutrinos and supernova neutrinos. Geoneutrinos originate from decays of nuclei in the earth. This kind of particles has very low energy, a very small particle flux ($\sim 10^6 \text{ cm}^{-2}\text{s}^{-1}$ at the surface [7]) and only consists of electron-neutrinos. Atmospheric neutrinos, on the other hand, can have very high energies. The low-lying part of the spectrum, unfortunately, has very low particle flux. Solar neutrinos, created in the sun, do have a large flux ($\sim 10^{11} \text{ cm}^{-2}\text{s}^{-1}$ from pp-chain, $\sim 10^6 \text{ cm}^{-2}\text{s}^{-1}$ from ^8B -decay [8]), but this is mostly for energies smaller than 1 MeV [3].

Supernova neutrinos come in two forms: relic neutrinos and burst neutrinos. The first kind are diffuse neutrinos from previous collapses, i.e. supernovae that happened at an earlier point in time. They have a low flux (estimated 12-16 $\text{cm}^{-2}\text{s}^{-1}$ [7]) and are

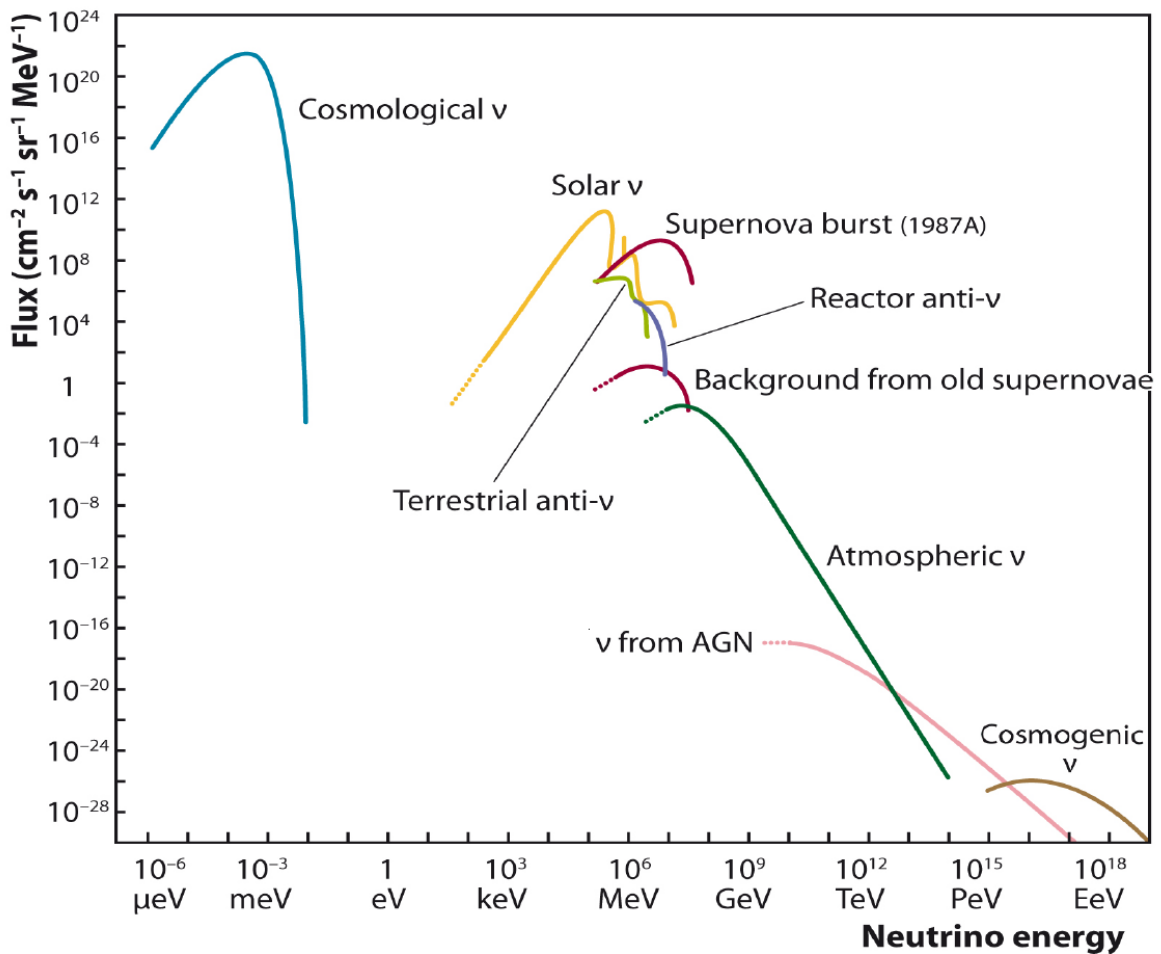


Figure 1.3: Flux and energy of neutrinos from various sources. Figure taken from [9]. In order to avoid confusion: numbers on horizontal axis are in eV.

composed of all flavors. The second kind appears only around the time that a supernova appears. As their name gives away, they come in a short pulse of high flux (starting at gravitational collapse and lasting about 20s [10]) and are also composed of all flavors [3].

The first three kinds of neutrinos (geoneutrinos, low energy atmospheric neutrinos, solar neutrinos) and supernova relic neutrinos are not suitable for CE ν NS measurements due to their low flux, even though they are, in principle, measurable. They are mostly background. Supernova burst neutrinos have the desired properties, however, supernovae are rather rare events, only occurring on average once every 30 years in our galaxy. As such, they cannot be used as a regular neutrino source, although they are a very important source (see section 1.3) [3].

Fig. 1.3 shows a comparison in flux and energy of the neutrinos from different natural sources [7]. Reactor antineutrinos are also displayed. Additional natural sources listed are generally not of interest for CE ν NS. Cosmological neutrinos (the 1.9 K cosmic neutrino background) are too low in energy for detection. Neutrinos from Active Galactic Nuclei (AGN) and cosmogenic neutrinos (from interactions of ultra-energetic protons with the 2.7 K cosmic microwave background) are too high in energy for CE ν NS.

1.2.2 CE ν NS experiments

Following the discovery of the weak neutral current in 1973, it was pointed out that CE ν NS should exist [4, 11]. Freedman et al. [11] pointed out the importance of neutrino-nucleus interactions, and the CE ν NS interaction specifically, in different astrophysical processes, such as stellar evolution, supernovae and nucleosynthesis (section 1.3). In 1984, Drukier and Stodolsky [4] proposed a way of detecting neutrinos through the CE ν NS interaction using a superconducting-grain method. This method made use of superconducting grains of a few micrometers in metastability inside a dielectric material in a magnetic field. The neutrino would flip the grain, causing the Meissner effect to disappear around the grain, which would lead to an electromagnetic signal. Their work emphasized the advantages of detection through CE ν NS, which included the large cross section, equal detection of all flavors and ready determination of the spectrum. However, detector technology was not yet advanced enough at the time and an experiment could never be realized.

In 2000, McKinsey and Doyle [12] and later, in 2003, Horowitz et al. [13] proposed neutrino detection based on scintillation in noble gases. The approach of this Cryogenic Low Energy Astrophysics with Noble gases (CLEAN) detector utilized the weak ionization signal produced by the nuclear recoil in the liquid. The same principle was employed for the two-phase argon ionization detector proposed by Haggmann and Bernstein [14] in 2004. In 2002, Oberauer [15] suggested the use of cryogenic detectors, similar to the ones developed for the search of dark matter, for the detection of neutrinos. This method would measure phonons produced in the detector material through the use of low temperature calorimeters with superconducting phase transition thermometers [12]. In [16], Scholberg (2006) describes the progress in ultra-low threshold detector technology of the preceding years. Among the various proposed detectors are noble element scintillator detectors, ionization detectors, solid state detectors, bubble detectors and superheated droplet detectors.

At present, several groups are working on the detection of CE ν NS. The COHERENT collaboration, established in 2014, is located at the Spallation Neutron Source (SNS) at

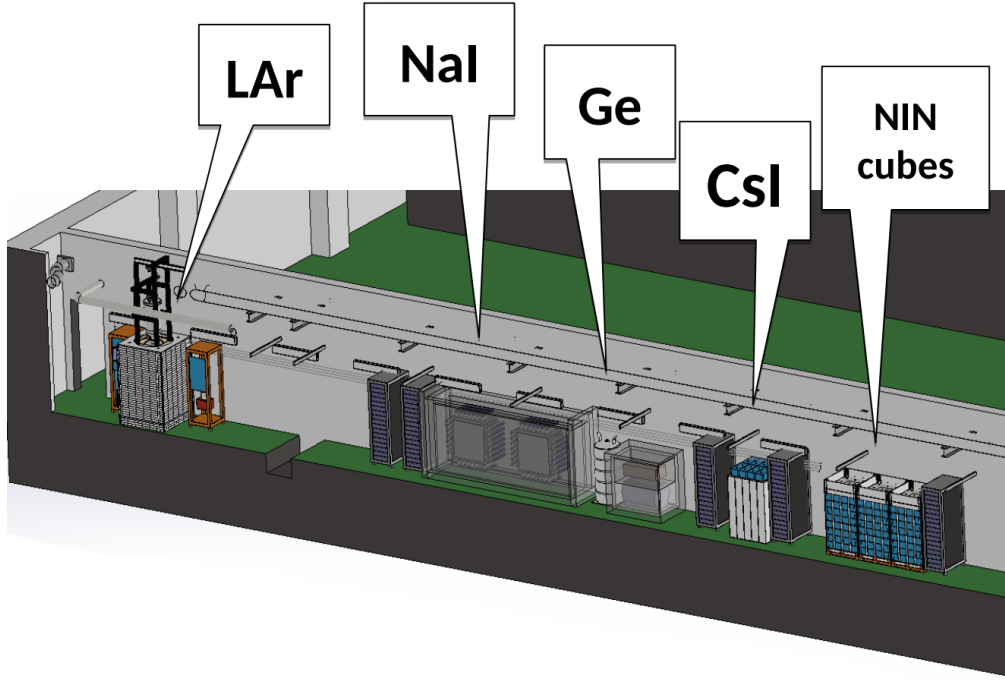


Figure 1.4: COHERENT experiment setup [18].

Oak Ridge National Laboratory (ORNL) [17]. The SNS is one of the most potent stopped-pion sources in the world at the moment, capable of producing around 8×10^{14} neutrinos per flavor per second as a result of the 1 GeV proton beam incident on a liquid mercury target [3]. COHERENT plans to measure $CE\nu NS$ and use it to search for physics beyond the standard model [2]. Their setup will employ a system of multiple detectors and will be located in the basement of the SNS. The original proposal consisted of three detectors: CsI[Na] scintillating crystals, p-type point-contact (PPC) germanium detectors and a two-phase liquid xenon (LXe) time projection chamber, which should “enable unambiguous discovery of $CE\nu NS$ ” [2]. Since then, the system has been changed to a combination of CsI[Na] scintillators, NaI[Tl] scintillators, a single-phase liquid argon (LAr) detector (named CENNS-10) and p-type point-contact germanium detectors [17]. The experiment is expected to accomplish a few primary goals. Firstly, it will measure $CE\nu NS$ for the first time. Secondly, it will precisely measure the cross section on a number of targets to test for non-standard interactions. Lastly, it will enable the characterization of low-threshold detectors to verify the background and detector response models. The latter is largely for the purpose of Weakly Interacting Massive Particle (WIMP) searches, since $CE\nu NS$ forms a background for this [2].

Background reduction will be possible through the pulsed SNS. The short SNS duty cycle is expected to reduce background by a factor of 10^3 to 10^4 . Since 2013, background neutron measurements have been ongoing in order to find the ideal location for the COHERENT experiment and reduce neutron-induced nuclear recoils. This has turned out to be the basement as this is the most neutron-quiet and is protected against cosmic rays by around 8 meters-water-equivalent [2].

The proposed final setup is shown in Fig. 1.4 [18]. The CsI[Na] scintillators were deployed in the facility in 2015. These detectors have low thresholds, yet large neutron numbers, beneficial for $CE\nu NS$ measurements. About 500 events above threshold per

year are expected [2, 17]. The CENNS-10 LAr detector has been deployed in December 2016. The use of argon should enable a light yield of around 40 photons per keV, as well as the distinction between nuclear recoil signals and electron background. About 240 events per year are expected [17]. The NaI[Tl] scintillator detectors had become available due to a discontinued United States Department of Homeland Security program and were deployed in July 2016. Currently studies of the detector characteristics are in progress. The PPC germanium detectors are expected to be deployed in early 2017 [17, 19]. This type of detector has low thresholds, high energy resolution and low internal backgrounds [17]. Additional detectors have been installed in order to study the neutron background caused by neutrino induced neutrons (NINs) from charged and neutral current interactions [17]. More information about COHERENT can be found in [2] and [17].

Another proposal using a stopped-pion source is the Coherent Elastic Neutrino-Nucleus Scattering (CENNS) experiment at the Fermilab Booster Neutrino Beam (BNB) [20]. The experiment would be placed at a very far off-axis (>45 degrees) position where pion-decay is the dominant source of neutrinos. Simulations have indicated that at maximum BNB power (5×10^{12} protons on target per pulse) the resulting neutrino flux would be around $5 \times 10^5 \text{ cm}^{-2}\text{s}^{-1}$ [20]. The proposed detector is a single-phase liquid argon detector. With the earlier mentioned flux, the detector is expected to have 250 $\text{CE}\nu\text{NS}$ events per ton of liquid argon per year at a recoil energy of 25 keV after background subtraction. Beam-related background would be suppressed using shielding. Background originating from sources other than the BNB such as cosmic rays, internal and external radioactivity are expected to be reduced by the beam duty cycle [20].

A number of different groups have also proposed $\text{CE}\nu\text{NS}$ experiments at nuclear reactors. The CoGeNT collaboration, which primarily focuses on the detection of very weak signals (~ 100 keV) in the context of dark matter such as WIMPs, have attempted measurements at the San Onofre Nuclear Generating Station using a p-type point contact germanium detector in 2008 [21]. A report in 2012 [22], explained the detector's electronic noise yielded a threshold too high for $\text{CE}\nu\text{NS}$ observation, although it was the first stable operation at very-low threshold in a long-term deployment. Similarly, Wong (2008) [23] proposed an experiment at the Kuo-Sheng Reactor Laboratory using Ultra-Low-Energy Germanium (ULEGe) detectors. The proposal was approved by the Taiwan EXperiment On Neutrino (TEXONO) collaboration at Kuo-Sheng Neutrino Laboratory (KSNL). Currently, research is being done to advance the technologies and techniques of the germanium detectors [24].

1.3 Supernova neutrinos

At the end of the life of a massive star ($\geq 8M_{\odot}$), the core has burnt through most of its fuel, since burning nuclei past iron no longer provides energy, and loses pressure until it can no longer support its own mass [25–27]. It collapses. When the center reaches and exceeds nuclear densities, it bounces back. The shock wave caused by the bounce may drive the star to expel its outer matter in a dramatic explosion called a supernova. The core's in-falling material causes a lowering in gravitational energy of the order of 10^{53} erg^3 [26, 27]. Around 99% of this energy is released in the form of neutrinos [26].

³1 erg = 10^{-7} J

The mechanism behind core-collapse supernovae is not fully understood. The most promising model seems to be the neutrino heating mechanism [29]. In core-collapse supernovae, the core shrinks due to gravitational collapse caused by pressure loss from photodisintegration of heavy nuclei and electron captures. The electron capture is illustrated by the following reaction,



As the volume of the core decreases, the electron Fermi energy increases [25]. The electron-neutrinos created in the process become less and less likely to escape the core as it becomes denser, inevitably resulting in electron-neutrino scattering inside the core. The inner core collapse eventually halts once beta equilibrium is reached, i.e. the rate of reaction (1.3) becomes the same as its inverse, at around nuclear densities ($\approx 2.6 \times 10^{14} \text{g cm}^{-3}$). Neutrino-nucleus interactions, both charged- and neutral-current, likely play an essential role in how the system reaches equilibrium, as the different interaction rates depend on their cross sections [25].

While the inner core's collapse halts, outer core material continues to fall onto the inner core. Due to this, the core overshoots the beta equilibrium condition and bounces back, creating a shock wave that propagates outward [27]. As the shock travels through the outer layers of the core, most of its energy is lost through dissociation and excitation of heavy nuclei, as well as electron capture [25, 27]. At a certain time after the bounce, the shock reaches the outermost layers of the protoneutron star (PNS), the surface of which is defined by the electron-neutrinosphere. Beyond this sphere, stellar material is transparent for electron-neutrinos, i.e. electron-neutrinos can freely travel through the stellar matter. This transparency causes the neutrinos to carry away large amounts of energy ($\sim 10^{53} \text{ erg/s}$ in $\sim 15 \text{ ms}$). The energy loss, eventually, causes the shock to stall and turn into a standing accretion shock (Fig. 1.5), i.e. a standing shock wave through which mass is accreted. Outward expansion stops and additional infalling material accretes to

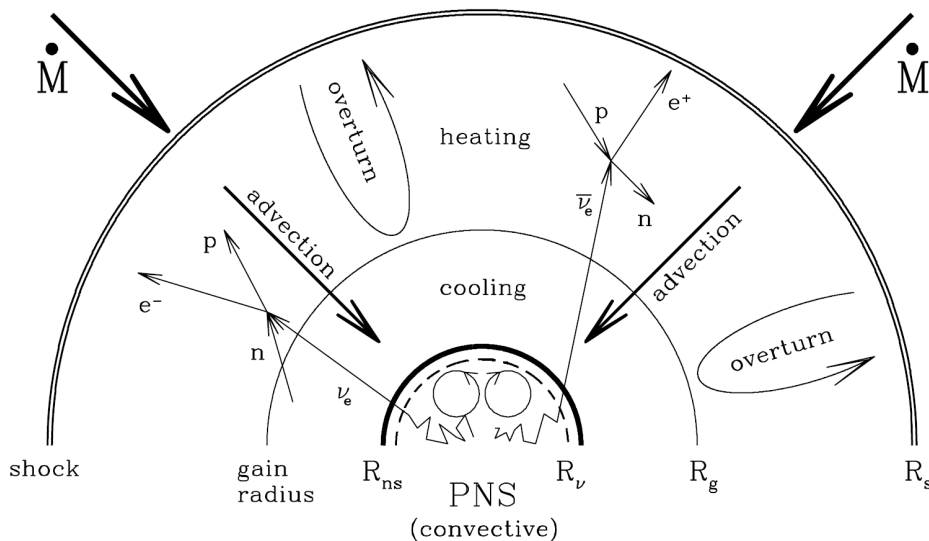


Figure 1.5: Depiction of a stalled supernova shock after bounce. Figure taken from [28]. Processes that determine the evolution of the shock are indicated. R_s is the radius of the shock. R_ν is the neutrinosphere. R_{ns} is the radius of the neutron star. At the gain radius R_g , heating balances cooling. \dot{M} indicates the mass accretion rate.

the existing core [30]. This can last for 300 ms, an eternity in supernova terms [27, 31].

Revival of the shock is where neutrino heating is key. Neutrinos diffusing out of the PNS heat the material above the surface and propel it outwards, reviving the shock and causing neutrino-driven winds (indicated in Fig. 1.5 by the arrows coming out of the PNS) [27, 29]. In this case, neutrino-nucleus interactions are expected to be crucial for the energy deposition. Additionally, neutrino-driven winds are thought to be an important site for the rapid neutron capture process (r-process), which suggests that neutrino-nucleus interactions are essential for nucleosynthesis [25].

A wide range of information on the supernova mechanism and neutrino properties can be extracted from neutrinos of core collapse supernovae. Information on the neutrino masses can potentially be derived from, for example, time-of-flight experiments. Furthermore, the direction of a supernova can be assumed before its light reaches us [26]. Additionally, supernovae are a valuable source of neutrinos for oscillation experiments [13].

Detection of these neutrinos through CE ν NS is desired for a few different reasons. Firstly, the cross section is relatively large, which gives high count rates. Secondly, detection through this method yields information on the total neutrino flux of a supernova, because the neutral current is flavor blind. Not to mention, it measures the nuclear recoil energy, so that the neutrino spectrum is readily deduced [13].

1.4 Standard Model tests

As will be seen in the chapter 2, the CE ν NS cross section is cleanly predicted by the Standard Model. As a consequence, it is sensitive to parameters in the SM; it depends

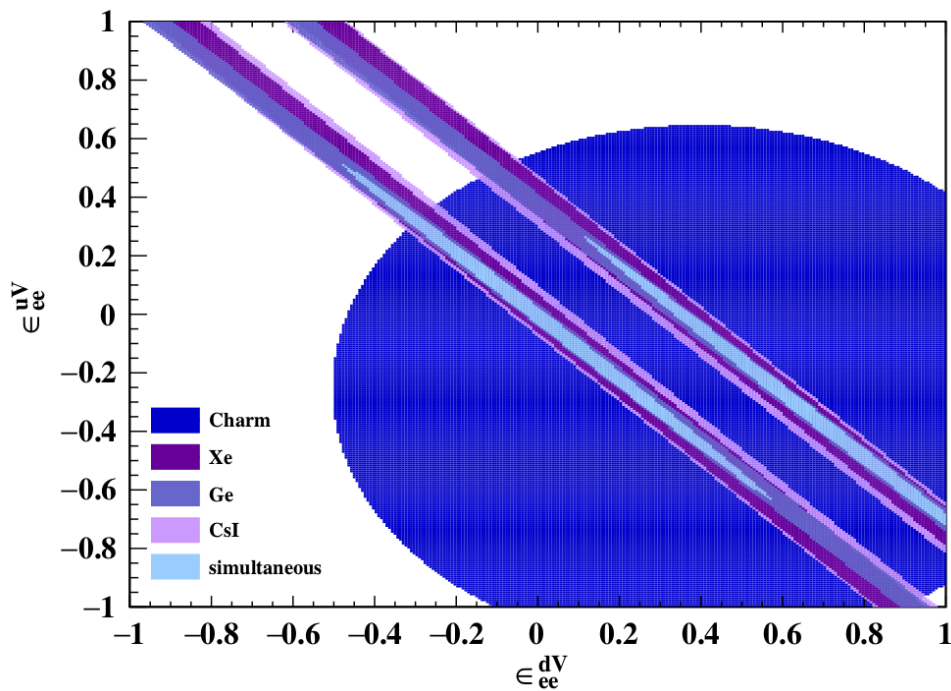


Figure 1.6: Parameter space for ϵ_{ee}^{uV} and ϵ_{ee}^{dV} NSI coupling constants by the CHARM collaboration together with the predicted sensitivity of the original COHERENT detector system. Figure taken from [2].

on a number of physical constants, such as the weak mixing angle θ_W , the weak coupling constant g and the vector and axial-vector couplings of the proton, neutron, neutrino and antineutrino, g_V^i and g_A^i . For this reason, CE ν NS provides a way to probe these constants [3].

Likewise, the SM very clearly describes what kind of interactions are allowed for each kind of particle. A deviation from the predicted cross section could then also point to new physics [3]. In the case of the weak interaction, and neutrinos specifically, experimental evidence for certain interactions can be difficult to acquire due to the small coupling constant of the weak interaction. Consequently, numerous interactions which do not appear in the SM, non-standard interactions (NSI), have been theorized. The possible existence of NSI was first mentioned by Wolfenstein [32, 33].

An NSI is usually represented by an effective four-point interaction [34]

$$\mathcal{L}_{\text{NSI}} = \varepsilon_{\alpha\beta}^{fP} \sqrt{2} G_F \bar{\nu}_\alpha \gamma^\mu (1 - \gamma^5) \nu_\beta \bar{f} \gamma^\mu P f. \quad (1.4)$$

Here, $\varepsilon_{\alpha\beta}^{fP}$ is the non-standard coupling constant, P is a chiral projection operator, f is a fermion and α and β are the neutrino flavors.

In the case of neutrino-quark coupling, the Lagrangian density can be given by [35]

$$\mathcal{L}_{\nu H}^{\text{NSI}} = \frac{G_F}{\sqrt{2}} \sum_{q,\alpha,\beta} \bar{\nu}_\alpha \gamma^\mu (1 - \gamma^5) \nu_\beta \left(\varepsilon_{\alpha\beta}^{qL} \bar{q} \gamma^\mu (1 - \gamma^5) q + \varepsilon_{\alpha\beta}^{qR} \bar{q} \gamma^\mu (1 + \gamma^5) q \right), \quad (1.5)$$

where the sum is taken over the quarks $q = u, d$ and the leptons $\alpha, \beta = e, \mu, \tau$. The parameters $\varepsilon_{\alpha\beta}^{qP}$ describe both non-universal interactions, $\alpha = \beta$, and flavor changing interactions, $\alpha \neq \beta$ [10]. Currently, the best constraints on these parameters are from the CHARM collaboration [36]. The parameter space for $\alpha = \beta = e$ together with the predicted sensitivity of the original COHERENT proposal is shown in Fig. 1.6 [2].

1.5 Outline

This thesis is structured as follows.

A short overview of the electroweak sector of the SM is given in chapter 2. Subsequently, the coherent elastic neutrino-nucleus scattering cross section is derived and the herein inserted form factor is defined. A short description of other neutrino-nucleus reaction channels is also presented.

In chapter 3, different frameworks for the description of the nucleus are described. Firstly, the Hartree-Fock method will be described, followed by the random phase approximation. Lastly, the Skyrme interaction and Woods-Saxon potential will be presented.

In chapter 4, an original study of the CE ν NS cross section is done. This includes a comparison of the cross section for different nuclei, as well as the effect of the form factor. Furthermore, a comparison of the cross section for different models of the nucleus is given. CE ν NS is also compared to other reaction channels. Finally, the sensitivity of CE ν NS to the weak mixing angle is demonstrated.

In chapter 5, a global conclusion will be given. The results will be summarized and some expectations for the future are laid out.

2 | Neutrino-nucleus cross sections

The purpose of a cross section is to provide a measure of the probability that a certain reaction occurs. Indeed, the cross section is calculated using the scattering amplitude of the reaction. The scattering amplitude of particle-particle interactions, such as quark-quark or lepton-quark, can be calculated relatively straightforward at the tree level, given the Feynman rules. The complexity increases rapidly once the particles are given internal structure. Protons, neutrons and nuclei all consist of multiple particles.

In this chapter, we derive the $\text{CE}\nu\text{NS}$ cross section and show how one can deal with the internal structure of nuclei. Also, the cross sections for neutral current quasielastic (NCQE) and charged current quasielastic (CCQE) neutrino-nucleus scattering are presented.

2.1 Electroweak sector of the SM

In the Standard Model, the electroweak Lagrangian density after symmetry breaking is given by [37]

$$\begin{aligned} \mathcal{L}_{\text{EW}} = & -e \sum_i Q_i \bar{\psi}_i \gamma^\mu \psi_i A_\mu \\ & - \frac{g}{2\sqrt{2}} \sum_i \bar{\Psi}_i \gamma^\mu (1 - \gamma^5) (T^+ W_\mu^+ + T^- W_\mu^-) \Psi_i \\ & - \frac{g}{2 \cos \theta_W} \sum_i \bar{\psi}_i \gamma^\mu (g_V^i - g_A^i \gamma^5) \psi_i Z_\mu. \end{aligned} \quad (2.1)$$

The ψ_i are the fermion fields, while Ψ_i are fermion doublets $\begin{pmatrix} \nu_{l_i} \\ l_i \end{pmatrix}$ and $\begin{pmatrix} u_i \\ d_i \end{pmatrix}$, where $d' = \sum_j V_{ij} d_j$ with V the Cabibbo-Kobayashi-Maskawa (CKM) matrix.

The first term in expression 2.1 represents electromagnetic interactions. A_μ is the massless photon field. Q_i is the electric charge of the fermion in units of e . The second term describes charged weak interactions. The W_μ^\pm are the charged weak boson fields with mass M_W . T^+ and T^- are weak isospin raising and lowering operators, respectively. The last term describes neutral weak interactions. Z_μ is the neutral weak boson field with mass $M_Z = \frac{M_W}{\cos \theta_W}$. The vector and axial-vector couplings, g_V^i and g_A^i , are given by

$$g_V^i = T_3^i - 2Q_i \sin^2 \theta_W \quad (2.2)$$

$$g_A^i = T_3^i, \quad (2.3)$$

where T_3^i is the weak isospin. Table 2.1 gives a list of the couplings for different types of particles [37].

With this, it is possible to define the different types of currents, i.e. the electromagnetic current, the weak charged current and the weak neutral current:

$$J_{\text{EM}}^\mu \equiv \sum_i Q_i \bar{\psi}_i \gamma^\mu \psi_i \quad (2.4)$$

$$J_{\text{CC}}^\mu \equiv \sum_i \bar{\Psi}_i \gamma^\mu (1 - \gamma^5) (T^+ + T^-) \Psi_i \quad (2.5)$$

$$J_{\text{NC}}^\mu \equiv \sum_i \bar{\psi}_i \gamma^\mu (g_V^i - g_A^i \gamma^5) \psi_i. \quad (2.6)$$

The neutral current (2.6) can also be written in its chiral form [35]

$$J_{\text{NC}}^\mu = 2 \sum_i \left[g_L^i \bar{\psi}_i^L \gamma^\mu \psi_i^L + g_R^i \bar{\psi}_i^R \gamma^\mu \psi_i^R \right], \quad (2.7)$$

with the left- and right-handed chiral projection operators

$$\psi_i^L = P_L \psi_i = \frac{1 - \gamma^5}{2} \psi_i, \quad \psi_i^R = P_R \psi_i = \frac{1 + \gamma^5}{2} \psi_i, \quad (2.8)$$

and

$$g_V^i = g_L^i + g_R^i, \quad g_A^i = g_L^i - g_R^i. \quad (2.9)$$

Table 2.1: Vector and axial-vector couplings for different types of particles.

Particle	g_V	g_A
ν	$\frac{1}{2}$	$\frac{1}{2}$
e	$-\frac{1}{2} + 2 \sin^2 \theta_W$	$-\frac{1}{2}$
u	$\frac{1}{2} - \frac{4}{3} \sin^2 \theta_W$	$\frac{1}{2}$
d	$-\frac{1}{2} + \frac{2}{3} \sin^2 \theta_W$	$-\frac{1}{2}$

It is relevant for the discussion in the next sections to have a look at the low energy limit in the case of neutral weak interactions. For energies small compared to the mass of the Z -boson, M_Z , the Z -boson propagator can be approximated through [38]

$$\frac{g_{\mu\nu} - \frac{p_\mu p_\nu}{M_Z^2}}{q^2 - M_Z^2} = -\frac{g_{\mu\nu}}{M_Z^2} + \mathcal{O}\left(\frac{1}{M_Z^4}\right). \quad (2.10)$$

In that case, it is convenient to write the neutral current sector as an effective four field interaction with the Fermi constant G_F : [35]

$$\mathcal{L}_{\text{NC}} = \frac{G_F}{\sqrt{2}} J_{\text{NC}}^\mu J_{\text{NC}\mu}. \quad (2.11)$$

2.2 Charged scalar QED

In the context of quantum field theory, nuclei are difficult to handle since they have an internal structure, i.e. they consist of nucleons, which in turn consist of quarks. The number of quarks in a nucleus rapidly increases with the amount of nucleons, since three valence quarks form a nucleon. Usually every nucleon (or even quark), would have to be considered individually, however, at low enough energies, there exist effective methods that deal with the nucleus as a whole. For our purposes, the nucleus will be approximated as a charged scalar particle. Later on, reaction amplitudes can be multiplied by a form factor to take into account the internal structure (see section 2.4).

For reasons that will become clear in section 2.3, it is instructive to take a look at an approximation to quantum electrodynamics (QED), called scalar QED. Recall that the phenomenon of charge appears, in the context of gauge theory, as the coupling strength to the gauge field. Therefore, if one wants to couple a scalar field ϕ to the gauge field A_μ , it is necessary to first verify the global symmetry. In the case of electric charge, this is global $U(1)$ -symmetry. Thus, the theory must be invariant under a transformation [39]

$$\phi \rightarrow e^{i\theta} \phi. \quad (2.12)$$

This is only possible if ϕ is complex. Consequently, starting from a free complex scalar field theory

$$\mathcal{L} = \partial^\mu \phi (\partial_\mu \phi)^* - m^2 \phi \phi^*, \quad (2.13)$$

one obtains the scalar QED Lagrangian density by defining the covariant derivative

$$D_\mu \equiv \partial_\mu + i\alpha A_\mu \quad (2.14)$$

and adding the Lagrangian density of electromagnetism

$$\mathcal{L}_{\text{EM}} = -\frac{1}{4}F^{\mu\nu}F_{\mu\nu} \quad (2.15)$$

in terms of the field strength tensor $F_{\mu\nu} = \partial_\mu A_\nu - \partial_\nu A_\mu$. The Lagrangian density of the theory becomes

$$\mathcal{L} = D^\mu\phi(D_\mu\phi)^* - m^2\phi\phi^* - \frac{1}{4}F^{\mu\nu}F_{\mu\nu}. \quad (2.16)$$

The classical equations of motion for this theory are [39]

$$(\square + m^2)\phi - i\alpha A_\mu\partial^\mu\phi = 0 \quad (2.17)$$

$$(\square + m^2)\phi^* + i\alpha A_\mu\partial^\mu\phi^* = 0. \quad (2.18)$$

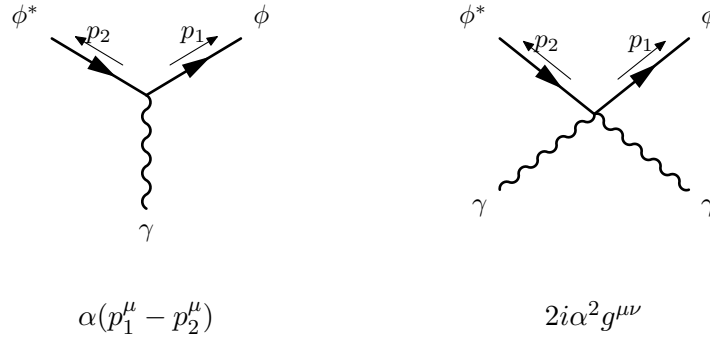
Both ϕ and ϕ^* , then, have the same mass and couple to the electromagnetic field, but with opposite charge.

Writing out the full Lagrangian density gives [39]

$$\mathcal{L} = \partial^\mu\phi\partial_\mu\phi^* - m^2\phi\phi^* - \frac{1}{4}F^{\mu\nu}F_{\mu\nu} - i\alpha A_\mu(\phi^*\partial^\mu\phi - \phi\partial^\mu\phi^*) + \alpha^2 A^\mu A_\mu\phi\phi^*. \quad (2.19)$$

Note that α in this expression is the coupling strength of the field A_μ to the scalar fields. If one were to approximate QED with scalar QED, the coupling strength would be $\alpha_i = eQ_i$.

Subsequently, the Feynman rules are easily found. A Lagrangian density of the form (2.19) gives two types of interaction vertices: one that couples ϕ and ϕ^* to A_μ and one that couples ϕ and ϕ^* to two A_μ s.



The corresponding vertex factors are $\alpha(p_1^\mu - p_2^\mu)$ and $2i\alpha^2 g^{\mu\nu}$, respectively. [39]

Internal lines represent the propagators. The complex scalar and photon propagators, respectively, are [39]

$$iG_F(p) = \frac{i}{p^2 - m^2 + i\varepsilon}, \quad iD_F^{\mu\nu}(k) = \frac{ig^{\mu\nu}}{k^2 + i\varepsilon}. \quad (2.20)$$

External lines represent the polarization or spinor of the incoming and outgoing particles and antiparticles. This factor for both incoming and outgoing scalar particles is simply 1 [39]. For photons, the factors are the polarization $\epsilon_r^\mu(k)$ for ingoing photons and $\epsilon_r^{*\mu}(k)$ for outgoing photons, where $r = 0, 1, 2, 3$. The $\epsilon_r^\mu(k)$ and $\epsilon_r^{*\mu}(k)$ have the property that [40]

$$\epsilon_{r\mu}(k)\epsilon_s^\mu(k) = \epsilon_{r\mu}^*(k)\epsilon_s^{*\mu}(k) = -\zeta_r\delta_{rs} \quad (2.21)$$

where $\zeta_0 = -1$ and $\zeta_1 = \zeta_2 = \zeta_3 = 1$.

2.3 CE ν NS cross section

With the necessary groundwork set, it is now possible to calculate the CE ν NS cross section. The CE ν NS interaction can be represented by the Feynman diagram in Fig. 2.2. The right-hand side of this diagram shows the nucleus interacting as a whole. The left-hand side shows a neutrino interacting through the exchange of a Z -boson. Since the neutral weak interaction is flavor blind, the flavor has not been specified. Additionally, it is assumed that the particle is a neutrino as opposed to an antineutrino. For reasons that will later become clear, if the nucleus is assumed to be even-even with ground state $J^\pi = 0^+$, the cross section is independent of the choice of neutrino or antineutrino, i.e. the cross section is the same for neutrinos and antineutrinos.

Simply following the Feynman rules gives the amplitude

$$i\mathcal{M}_{rr'} = \frac{-ig}{2\cos\theta_W} g_L^\nu \bar{u}_{r'}(p_1) \gamma^\mu (1 - \gamma^5) u_r(k_1) \frac{-i \left(g_{\mu\nu} - \frac{p_\mu p_\nu}{M_Z^2} \right)}{q^2 - M_Z^2} J_{\text{nuc}}^\nu, \quad (2.22)$$

where $u_r(k_1)$ and $\bar{u}_{r'}(p_1)$ are the initial and final states of a Dirac particle, in this case the neutrino, the Z -boson propagator was used in the middle and the nuclear side has been abstractified into the nuclear current J_{nuc}^ν .

To evaluate J_{nuc}^ν , certain assumptions need to be made. The nucleus must be in its ground state with quantum number $J^\pi = 0^+$. If so desired, it is possible to do the calculation for spin- $\frac{1}{2}$ or spin-1 nuclei, but that is beyond the scope of this work. Additionally, the nucleus is a spherically symmetric even-even nucleus. The interaction, therefore, does not violate parity.

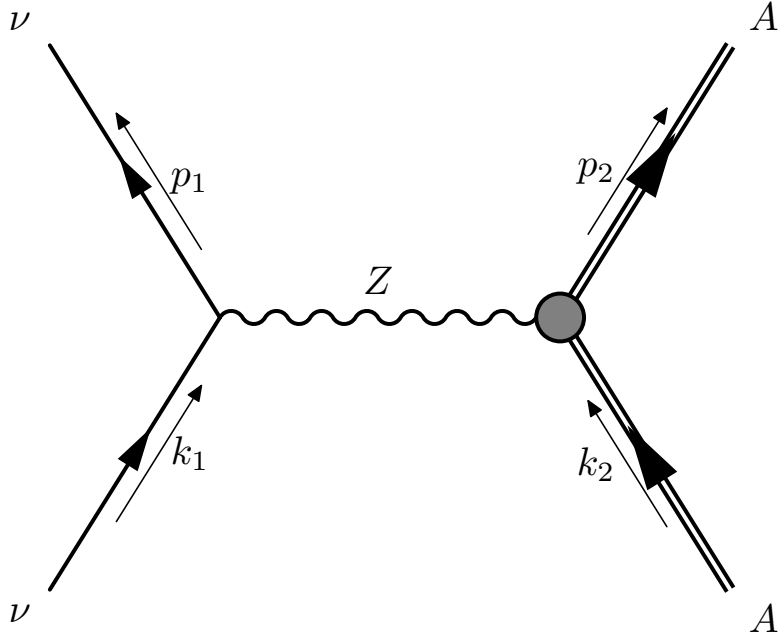


Figure 2.2: Feynman diagram of the CE ν NS interaction.

Observe that, since there is no parity violation, the Z -boson can essentially be regarded as a massive photon. The interaction for the nucleus can thus be approximated by that of the Lagrangian density (2.19) with an added mass term for the photon set to mass M_Z . The gauge boson propagator for this theory is the same as the Z -boson propagator, so that the two theories fit together nicely. Note that adding a mass term introduces the problem that the theory loses its $U(1)$ -symmetry. However, similarly to intermediate vector boson (IVB) theory, this does not pose much of an issue, since we are working with low energies.

Using the Feynman rules, one finds

$$J_{\text{nuc}}^\nu = \alpha(k_2 + p_2)^\nu, \quad (2.23)$$

where α does not represent the electric charge of the scalar particle, but instead becomes the weak interaction-equivalent to the electric charge, i.e. the weak coupling strength. The value of α can be found by consideration of the neutral current sector of (2.1). Since nuclei consist only of quarks, J_{nuc}^ν will only depend on the quark section of J_{NC}^μ . In particular, we only deal with nuclei made of u and d quarks. Additionally, using the assumptions made about the nucleus results in parity conservation:

$$\bar{u}^L \gamma^\mu u^L = \bar{u}^R \gamma^\mu u^R \quad (2.24)$$

$$\bar{d}^L \gamma^\mu d^L = \bar{d}^R \gamma^\mu d^R. \quad (2.25)$$

Thus, in the u and d section of J_{NC}^μ ,

$$J_{\text{NC}}^\mu = g_V^u \bar{u} \gamma^\mu u + g_V^d \bar{d} \gamma^\mu d. \quad (2.26)$$

By comparison with the neutral current sector of (2.1), we deduce that u and d quarks contribute a weak coupling strength of $\frac{g}{2 \cos \theta_W} g_V^u$ and $\frac{g}{2 \cos \theta_W} g_V^d$, respectively. For a nucleus with Z protons and N neutrons, i.e. $2Z + N$ u quarks and $2N + Z$ d quarks, the weak coupling strength of the nucleus becomes

$$\begin{aligned} \alpha &= (2Z + N) \frac{g}{2 \cos \theta_W} g_V^u + (2N + Z) \frac{g}{2 \cos \theta_W} g_V^d \\ &= \frac{g}{2 \cos \theta_W} \left((2Z + N) \left(\frac{1}{2} - \frac{4}{3} \sin^2 \theta_W \right) + (2N + Z) \left(-\frac{1}{2} + \frac{2}{3} \sin^2 \theta_W \right) \right) \\ &= \frac{g}{2 \cos \theta_W} \frac{1}{2} \left((1 - 4 \sin^2 \theta_W) Z - N \right) \\ &\equiv \frac{g}{2 \cos \theta_W} \frac{1}{2} Q_W. \end{aligned} \quad (2.27)$$

Here, the weak charge Q_W of the nucleus has been introduced to simplify the notation.

As mentioned earlier, with this approximation for the nuclear current, the nucleus is modeled as a point-like particle. In order to take into account internal structure, one can multiply the result by a form factor. A detailed discussion of the nuclear form factor can be found in section 2.4. For now, the form factor $F(q^2)$ will just be introduced into J_{nuc}^μ .

$$J_{\text{nuc}}^\nu = \alpha(k_2 + p_2)^\nu F(q^2). \quad (2.28)$$

Inserting this result into (2.22), one obtains

$$i\mathcal{M}_{rr'} = \frac{-g^2}{8 \cos^2 \theta_W} Q_W F(q^2) g_L^\nu \bar{u}_{r'}(p_1) \gamma^\mu (1 - \gamma^5) u_r(k_1) \frac{\left(g_{\mu\nu} - \frac{p_\mu p_\nu}{M_Z^2}\right)}{q^2 - M_Z^2} (k_2 + p_2)_\mu. \quad (2.29)$$

In the low energy limit, i.e. $q^2 \ll M_Z^2$, it is possible to approximate the Z -boson propagator by [38]

$$\frac{g_{\mu\nu} - \frac{p_\mu p_\nu}{M_Z^2}}{q^2 - M_Z^2} = -\frac{g_{\mu\nu}}{M_Z^2} + \mathcal{O}\left(\frac{1}{M_Z^4}\right). \quad (2.30)$$

With this approximation, the interaction becomes the effective four field interaction of equation (2.11). The amplitude becomes

$$-\frac{g^2}{8 \cos^2 \theta_W M_Z^2} Q_W F(q^2) g_L^\nu \bar{u}_{r'}(p_1) \gamma^\mu (1 - \gamma^5) u_r(k_1) (k_2 + p_2)_\mu \quad (2.31)$$

or, since $M_W = M_Z \cos \theta_W$ and $\frac{g^2}{8M_W^2} = \frac{G_F}{\sqrt{2}}$,

$$i\mathcal{M}_{rr'} = -\frac{G_F}{\sqrt{2}} Q_W F(q^2) g_L^\nu \bar{u}_{r'}(p_1) \gamma^\mu (1 - \gamma^5) u_r(k_1) (k_2 + p_2)_\mu. \quad (2.32)$$

The calculation of $|\mathcal{M}|^2$ is done by multiplying $i\mathcal{M}_{rr'}$ with its complex conjugate and summing over the spin states. Only the result will be stated here. The full evaluation of $|\mathcal{M}|^2$ can be found in Appendix A. The amplitude becomes

$$|\mathcal{M}|^2 = 32 G_F^2 Q_W^2 |F(q^2)|^2 (g_L^\nu)^2 E^2 M^2 \left(1 - \frac{T}{E} - \frac{MT}{2E^2}\right). \quad (2.33)$$

From 2.32, it is easy to see that substituting the neutrino for an antineutrino, i.e. substituting $\bar{v}_r(k_1)$ and $v_{r'}(p_1)$ for $u_r(k_1)$ and $\bar{u}_{r'}(p_1)$, will give the same $|\mathcal{M}|^2$. Indeed, since the interaction does not violate parity, the amplitude is the same for neutrinos and antineutrinos.

By Fermi's golden rule (Appendix B), the expression for the scattering cross section of a massless particle with a massive particle in the lab frame is

$$\frac{d\sigma}{dq^2} = -\frac{|\mathcal{M}|^2}{64\pi E^2 M^2}. \quad (2.34)$$

Additionally,

$$\frac{d\sigma}{dq^2} = \frac{d\sigma}{dT} \frac{dT}{dq^2}, \quad (2.35)$$

so that with eq. (A.15)

$$\frac{d\sigma}{dT} = -2M \frac{d\sigma}{dq^2}. \quad (2.36)$$

Therefore, the recoil differential cross section in the lab frame is

$$\frac{d\sigma}{dT} = \frac{G_F^2}{4\pi} Q_W^2 |F(-2MT)|^2 M \left(1 - \frac{T}{E} - \frac{MT}{2E^2}\right). \quad (2.37)$$

2.4 Nuclear form factor

The form factor F provides a way of characterizing certain particle interactions without having to incorporate the underlying physics. As a result, it incorporates the greatest uncertainty on the cross section. In the case of coherent elastic scattering, one mainly wants to correct for the finite size of the nucleus. Other effects can be included, such as the magnetic moment and strangeness. These will not be discussed, however. The form factor, then, is a function that describes the internal structure of the nucleus through the spatial distribution of the nucleons. Much like in electromagnetism, one can associate a weak charge with each nucleon, which in turn gives a weak charge distribution. Since one deals with low energies, this can be treated non-relativistically.

In order for the neutrino to see the nucleus and its details, the wavelength of the Z -boson must be smaller than the dimensions of the nucleus [41]. At low energies, the wavelength of the Z -boson is larger than the dimensions of the nucleus, so that the neutrino sees the nucleus more or less as a point-like particle. This limit is valid when $|\mathbf{q}| < 1/R$, with R the radius of the nucleus. At higher energies, i.e. when $|\mathbf{q}|$ approaches $1/R$, the neutrino sees an object with finite size and the internal structure of the nucleus starts becoming important [11].

The neutral weak form factor can be defined as the Fourier transform of the weak charge distribution of the nucleus $\rho_W(\mathbf{r})$:

$$F(q) \equiv \frac{1}{Q_W} \int \rho_W(\mathbf{r}) e^{i\mathbf{q}\cdot\mathbf{r}} d^3\mathbf{r}, \quad (2.38)$$

where $q = (T, \mathbf{q})$ is the 4-momentum transfer and ρ_W is normalized through

$$Q_W = \int_{\mathbb{R}^3} \rho_W(\mathbf{r}) d^3\mathbf{r}. \quad (2.39)$$

This definition ensures that $F(q^2) = 1$ for a point-like particle, as one would expect.

Assuming that the nucleus is spherically symmetric,

$$F(q^2) \equiv \frac{4\pi}{Q_W} \int \rho_W(|\mathbf{r}|) \frac{\sin(|\mathbf{q}||\mathbf{r}|)}{|\mathbf{q}||\mathbf{r}|} \mathbf{r}^2 d|\mathbf{r}|. \quad (2.40)$$

Here, the form factor has been written as $F(q^2)$ to symbolize the fact that in a spherically symmetric system, F only depends on the magnitude of q . F can also be defined as a function of Q^2 , for which $Q^2 = -q^2$, so that $F(Q^2) = F(q^2)$.

In terms of the proton and neutron distributions $\rho_p(\mathbf{r})$ and $\rho_n(\mathbf{r})$, if one associates the weak charge $1 - 4\sin^2\theta_W$ with the proton and -1 with the neutron, $F(q^2)$ becomes [13]

$$F(q^2) = \frac{4\pi}{Q_W} \int ((1 - 4\sin^2\theta_W)\rho_p(|\mathbf{r}|) - \rho_n(|\mathbf{r}|)) \frac{\sin(|\mathbf{q}||\mathbf{r}|)}{|\mathbf{q}||\mathbf{r}|} \mathbf{r}^2 d|\mathbf{r}|. \quad (2.41)$$

ρ_p and ρ_n are normalized through

$$Z = \int_{\mathbb{R}^3} \rho_p(\mathbf{r}) d^3\mathbf{r}, \quad N = \int_{\mathbb{R}^3} \rho_n(\mathbf{r}) d^3\mathbf{r}, \quad (2.42)$$

where Z and N are the number of protons and neutrons, respectively. It can be seen that the form factor depends mainly on the neutron distribution, considering the factor $1 - 4\sin^2\theta_W$ is small.

The weak form factor can be obtained both theoretically and experimentally. Since experimental set-ups are currently being built to measure the CE ν NS cross section, experimental results are not yet available. The theoretical form factor, on the other hand, can be obtained in different ways.

A logical way of calculating $F(q^2)$ is to first obtain an expression for $\rho(|\mathbf{r}|)$. Given the wave function Ψ of a nucleus, the nuclear density is derived through

$$\rho(\mathbf{r}) = |\Psi(\mathbf{r})|^2. \quad (2.43)$$

In a shell model description of the nucleus, wave functions ϕ_{α_i} of the nucleons are required, with α_i the collection of quantum numbers of particle i and space, spin and isospin coordinates \mathbf{r} , σ and τ . The nucleon density is then given by [42]

$$\rho_\tau(\mathbf{r}) = \sum_{i,\sigma} |\phi_{\alpha_i}(\mathbf{r}, \sigma, \tau)|^2 \quad (\tau = n, p). \quad (2.44)$$

For a doubly-closed-shell nucleus, one can make the ansatz [42]

$$\phi_{q,n,l,s,j,m}(\mathbf{r}, \sigma, \tau) = \frac{R_{q,n,l,j}(|\mathbf{r}|)}{|\mathbf{r}|} Y_{l,s,j,m}(\hat{\mathbf{r}}, \sigma) \chi(\tau). \quad (2.45)$$

The nucleon density will then only depend on the radial factor:

$$\rho_\tau(|\mathbf{r}|) = \frac{1}{4\pi|\mathbf{r}|^2} \sum_{\alpha} (2j_{\alpha} + 1) R_{\alpha}^2(|\mathbf{r}|). \quad (2.46)$$

2.5 Other neutrino-nucleus reaction channels

2.5.1 Neutral current quasielastic scattering

In neutral current quasielastic (NCQE) neutrino-nucleus scattering, the incoming neutrino or antineutrino is inelastically scattered off a nucleus A through a Z -boson:

$$\nu(\bar{\nu}) + A \rightarrow \nu'(\bar{\nu}') + X. \quad (2.47)$$

X denotes the hadronic final state. The neutrino interacts with a bound nucleon, which is subsequently emitted from the nucleus [43]. Essentially, the nucleus is left in an excited state where the nucleon is excited to the continuum [44]. Only the final nucleon or, with better detectors, the nucleus can be detected [45].

A full derivation of the cross section is beyond the scope of this work, only the result will be stated. The incoming neutrino has 4-momentum $k_1 = (\varepsilon_i, \mathbf{k}_1)$. The nucleus is spherically symmetrical and initially in its ground state with $J_i^{\pi_i} = 0^+$ and 4-momentum $k_2 = (E_i, \mathbf{k}_2)$. The outgoing neutrino has 4-momentum $p_1 = (\varepsilon_f, \mathbf{p}_1)$ and the nucleus is an excited state with $J_f^{\pi_f}$ and 4-momentum $p_2 = (E_f, \mathbf{p}_2)$. The 4-momentum transfer $q = k_1 - k_2 = p_2 - p_1 = (\omega, \mathbf{q})$.

The double differential cross section is given by [44]

$$\frac{d^2\sigma}{d\omega d\Omega} = (2\pi)^4 |\mathbf{p}_1| \varepsilon_f \sum_{s_f, s_i} \frac{1}{2J_i + 1} \sum_{M_f, M_i} |\langle f | \hat{H}_W | i \rangle|^2, \quad (2.48)$$

where the first sum is over the final and initial spin of the lepton and the second spin is over the final and initial magnetic quantum number of the nucleus. \hat{H}_W is the weak interaction Hamiltonian with

$$\hat{H}_W = \frac{G_F}{\sqrt{2}} \int d^3\mathbf{x} \hat{J}_{\text{NC:neutrino},\mu}(\mathbf{x}) \hat{J}_{\text{hadronic}}^\mu(\mathbf{x}), \quad (2.49)$$

where $\hat{J}_{\text{NC:neutrino}}^\mu$ is the part of J_{NC}^μ (2.6) that includes neutrinos and $\hat{J}_{\text{hadronic}}^\mu$ is defined by

$$\hat{J}_{\text{hadronic}}^\mu = \sum_{N=p,n} \bar{\psi}_N \left(G_E^V(q^2) \gamma^\mu + \frac{\sigma_{\mu\nu} q^\nu}{2M} G_M^V(q^2) + G^A(q^2) \gamma^\mu \gamma^5 \right) \psi_N \quad (2.50)$$

with ψ_N the nucleon wave function and the nucleon form factors obtained from the conserved vector current theorem

$$G_E^V = \frac{1}{2}(1 - 4 \sin^2 \theta_W) \tau_3 - \sin^2 \theta_W, \quad (2.51)$$

$$G_M^V = \frac{1}{2}(1 - 4 \sin^2 \theta_W) (\mu_p - \mu_n) \tau_3 - \sin^2 \theta_W (\mu_p + \mu_n), \quad (2.52)$$

$$G^A = -1.262 \tau_3. \quad (2.53)$$

μ_p and μ_n are the magnetic moments of the proton and neutron respectively, and τ_3 is the third isospin component.

At low energies, i.e. $|\mathbf{q}| < 400$ MeV, the cross section simplifies to [44]

$$\left(\frac{d^2\sigma}{d\omega d\Omega} \right)_{\nu}^{\bar{\nu}} = \frac{G_F^2 \varepsilon_f^2}{\pi} \frac{2 \cos^2 \left(\frac{\theta}{2} \right)}{2J_i + 1} \left(\sum_{J=0}^{\infty} \sigma_{\text{CL}}^J + \sum_{J=1}^{\infty} \sigma_{\text{T}}^J \right), \quad (2.54)$$

with θ the neutrino scattering angle and

$$\sigma_{\text{CL}}^J = |\langle J_f || \left(\hat{\mathcal{M}}_J(|\mathbf{q}|) + \frac{\omega}{|\mathbf{q}|} \hat{\mathcal{L}}_J(|\mathbf{q}|) \right) || J_i \rangle|^2 \quad (2.55)$$

$$\begin{aligned} \sigma_{\text{T}}^J &= \left(-\frac{q^2}{2|\mathbf{q}|^2} + \tan^2 \left(\frac{\theta}{2} \right) \right) \left[|\langle J_f || \hat{\mathcal{J}}_J^{\text{mag}}(|\mathbf{q}|) || J_i \rangle|^2 + |\langle J_f || \hat{\mathcal{J}}_J^{\text{el}}(|\mathbf{q}|) || J_i \rangle|^2 \right] \\ &\mp \tan \left(\frac{\theta}{2} \right) \sqrt{-\frac{q^2}{|\mathbf{q}|^2} + \tan^2 \left(\frac{\theta}{2} \right)} \left[2 \text{Re} \left(\langle J_f || \hat{\mathcal{J}}_J^{\text{mag}}(|\mathbf{q}|) || J_i \rangle \langle J_f || \hat{\mathcal{J}}_J^{\text{el}}(|\mathbf{q}|) || J_i \rangle^* \right) \right]. \end{aligned} \quad (2.56)$$

The operators $\hat{\mathcal{M}}_{JM}$, $\hat{\mathcal{L}}_{JM}$, $\hat{\mathcal{J}}_{JM}^{\text{el}}$ and $\hat{\mathcal{J}}_{JM}^{\text{mag}}$ are the Coulomb, longitudinal, transverse electric and magnetic operators, respectively. They are defined as follows:

$$\hat{\mathcal{M}}_{JM} = \int d^3\mathbf{x} (j_J(|\mathbf{q}|r) Y_J^M(\Omega_x)) \hat{J}_0(\mathbf{x}) \quad (2.57)$$

$$\hat{\mathcal{L}}_{JM} = \frac{i}{|\mathbf{q}|} \int d^3\mathbf{x} (\nabla [j_J(|\mathbf{q}|r) Y_J^M(\Omega_x)]) \hat{\mathbf{J}}(\mathbf{x}) \quad (2.58)$$

$$\hat{\mathcal{J}}_{JM}^{\text{el}} = \frac{1}{|\mathbf{q}|} \int d^3\mathbf{x} (\nabla \times [j_J(|\mathbf{q}|r) \mathcal{Y}_{J,J}^M(\Omega_x)]) \hat{\mathbf{J}}(\mathbf{x}) \quad (2.59)$$

$$\hat{\mathcal{J}}_{JM}^{\text{mag}} = \int d^3\mathbf{x} (j_J(|\mathbf{q}|r) \mathcal{Y}_{J,J}^M(\Omega_x)) \cdot \hat{\mathbf{J}}(\mathbf{x}). \quad (2.60)$$

2.5.2 Charged current quasielastic scattering

In charged current quasielastic (CCQE) neutrino-nucleus scattering, the incoming neutrino or antineutrino is inelastically scattered off a nucleus A through a W^\pm -boson:

$$\nu_l(\bar{\nu}_l) + A \rightarrow l^-(l^+) + X. \quad (2.61)$$

X denotes the unobserved hadronic final state [46]. Like in the neutral current case, a nucleon is emitted after the neutrino interacts with the nucleus. In this case, the final lepton can be detected [45].

A full derivation of the CCQE cross section is beyond the scope of this work. Thus, only the result will be stated. The 4-momenta are defined as in section 2.5.1.

The double differential cross section is given by [46]

$$\left(\frac{d^2\sigma}{d\omega d\Omega} \right)_\nu = \frac{G_F^2 \cos^2 \theta_c}{(4\pi)^2} \frac{2}{2J_i + 1} \varepsilon_f |\mathbf{p}_1| \zeta^2(Z', \varepsilon_f, q) \left(\sum_{J=0}^{\infty} \sigma_{\text{CL},\nu}^J + \sum_{J=1}^{\infty} \sigma_{\text{T},\nu}^J \right), \quad (2.62)$$

where θ_c is the Cabibbo angle and $\zeta(Z', \varepsilon_f, q)$ takes into account the distortion of the lepton wave function in the Coulomb field generated by Z' protons through a Fermi function. The Coulomb-longitudinal $\sigma_{\text{CL},\nu}^J$ and transverse $\sigma_{\text{T},\nu}^J$ parts are given by

$$\sigma_{\text{CL},\nu}^J = v_\nu^{\mathcal{M}} R_\nu^{\mathcal{M}} + v_\nu^{\mathcal{L}} R_\nu^{\mathcal{L}} + 2v_\nu^{\mathcal{ML}} R_\nu^{\mathcal{ML}} \quad (2.63)$$

$$\sigma_{\text{T},\nu}^J = v_\nu^{\mathcal{T}} R_\nu^{\mathcal{T}} + 2v_\nu^{\mathcal{TT}} R_\nu^{\mathcal{TT}} \quad (2.64)$$

where the coefficients v are

$$v_\nu^{\mathcal{M}} = 1 + \frac{|\mathbf{p}_1|}{\varepsilon_f} \cos \theta, \quad (2.65)$$

$$v_\nu^{\mathcal{L}} = 1 + \frac{|\mathbf{p}_1|}{\varepsilon_f} \cos \theta - \frac{2\varepsilon_i \varepsilon_f}{|\mathbf{q}|^2} \left(\frac{|\mathbf{p}_1|}{\varepsilon_f} \right)^2 \sin^2 \theta, \quad (2.66)$$

$$v_\nu^{\mathcal{ML}} = \frac{\omega}{|\mathbf{q}|} \left(1 + \frac{|\mathbf{p}_1|}{\varepsilon_f} \cos \theta \right) + \frac{m_l^2}{\varepsilon_f |\mathbf{q}|}, \quad (2.67)$$

$$v_\nu^{\mathcal{T}} = 1 - \frac{|\mathbf{p}_1|}{\varepsilon_f} \cos \theta + \frac{\varepsilon_i \varepsilon_f}{|\mathbf{q}|^2} \left(\frac{|\mathbf{p}_1|}{\varepsilon_f} \right)^2 \sin^2 \theta, \quad (2.68)$$

$$v_\nu^{\mathcal{TT}} = \frac{\varepsilon_i + \varepsilon_f}{|\mathbf{q}|} \left(1 + \frac{|\mathbf{p}_1|}{\varepsilon_f} \cos \theta \right) - \frac{m_l^2}{\varepsilon_f |\mathbf{q}|}, \quad (2.69)$$

$$(2.70)$$

and the response functions R are

$$R_\nu^{\mathcal{M}} = \langle J_f | | \hat{\mathcal{M}}_J(|\mathbf{q}|) | | J_i \rangle, \quad (2.71)$$

$$R_\nu^{\mathcal{L}} = \langle J_f | | \hat{\mathcal{L}}_J(|\mathbf{q}|) | | J_i \rangle, \quad (2.72)$$

$$R_\nu^{\mathcal{ML}} = \text{Re} \left(\langle J_f | | \hat{\mathcal{L}}_J(|\mathbf{q}|) | | J_i \rangle \langle J_f | | \hat{\mathcal{M}}_J(|\mathbf{q}|) | | J_i \rangle^* \right), \quad (2.73)$$

$$R_\nu^{\mathcal{T}} = |\langle J_f | | \hat{\mathcal{J}}_J^{\text{mag}}(|\mathbf{q}|) | | J_i \rangle|^2 + |\langle J_f | | \hat{\mathcal{J}}_J^{\text{el}}(|\mathbf{q}|) | | J_i \rangle|^2, \quad (2.74)$$

$$R_\nu^{\mathcal{TT}} = \text{Re} \left(\langle J_f | | \hat{\mathcal{J}}_J^{\text{mag}}(|\mathbf{q}|) | | J_i \rangle \langle J_f | | \hat{\mathcal{J}}_J^{\text{el}}(|\mathbf{q}|) | | J_i \rangle^* \right), \quad (2.75)$$

with the $\hat{\mathcal{M}}_J$, $\hat{\mathcal{L}}_J$, $\hat{\mathcal{J}}_J^{\text{mag}}$ and $\hat{\mathcal{J}}_J^{\text{el}}$ defined as in section 2.5.1.

3 | Description of the nucleus

Calculation of nuclear wave functions and energy levels is a rather complex matter. The system is frequently too small to be correctly treated statistically, yet too big for a fully analytical description. Furthermore, nuclear interactions involve three of the four fundamental forces: electromagnetism, the strong nuclear force and the weak nuclear force, making mean field or effective field theories rather cumbersome to conceive. Be that as it may, a number of relatively simple models have been found that describe such many-body systems quite well. Often, these models focus on reproducing a certain phenomenon and therefore lack in portraying others. In order to obtain a more complete description of the nucleus, it is useful to compare different models.

In this chapter, a few ways of computing wave functions and the effective potentials used in these computations will be presented. In what follows, 4-vectors and 4-momenta will not make an appearance. Therefore, it is convenient to define $|\mathbf{x}| = x$.

3.1 Hartree-Fock method

The Hartree-Fock (HF) method finds its purpose in many fields of physics and chemistry, including quantum chemistry, atomic physics, solid-state physics and nuclear physics. The method provides an approximate way of calculating the wave functions and energy levels of many-body systems in a stationary state.

The ultimate goal of the HF method is to solve the Schrödinger equation [47]

$$H|\Psi_i\rangle = E_i|\Psi_i\rangle. \quad (3.1)$$

For a nucleus, the nuclear Hamiltonian has the form

$$H = T + U, \quad (3.2)$$

with T and U the kinetic and potential energy operators. Nuclear interactions are taken into account through the potential U . Possible potentials U can be the Woods-Saxon potential, the Skyrme potential, etc. (See sec. 3.3.)

Note that exact solutions $|\Psi_i\rangle$ are not Slater determinants. Therefore, Ψ_0 is approximated by a Slater determinant Φ [47]. As such, the state of a nucleus with mass number A in the HF method is given by a single Slater determinant (see appendix C)

$$\Phi(\mathbf{x}_1, \mathbf{x}_2, \dots, \mathbf{x}_A) = \frac{1}{\sqrt{A!}} \begin{vmatrix} \phi_{\alpha_1}(\mathbf{x}_1) & \phi_{\alpha_2}(\mathbf{x}_1) & \cdots & \phi_{\alpha_A}(\mathbf{x}_1) \\ \phi_{\alpha_1}(\mathbf{x}_2) & \phi_{\alpha_2}(\mathbf{x}_2) & \cdots & \phi_{\alpha_A}(\mathbf{x}_2) \\ \vdots & \vdots & \ddots & \vdots \\ \phi_{\alpha_1}(\mathbf{x}_A) & \phi_{\alpha_2}(\mathbf{x}_A) & \cdots & \phi_{\alpha_A}(\mathbf{x}_A) \end{vmatrix}, \quad (3.3)$$

where the ϕ_{α_i} are the single particle wave functions of the nucleons with the set of quantum numbers α_i and the \mathbf{x}_i denote the space, spin and isospin coordinates.

Let E_0 be the ground state energy of the nucleus and Φ any Slater determinant of the form (3.3). Through the variational principle, one knows that [47]

$$E_0 \leq \frac{\langle \Phi | H | \Phi \rangle}{\langle \Phi | \Phi \rangle}. \quad (3.4)$$

The aim is, thus, to find a Slater determinant Φ for which the HF energy,

$$E^{\text{HF}} = \frac{\langle \Phi | H | \Phi \rangle}{\langle \Phi | \Phi \rangle}, \quad (3.5)$$

is minimal [47]. This Φ will be the optimal approximation of Ψ_0 , i.e. will most accurately describe the exact solution Ψ_0 .

The minimization process starts by choosing an approximate Slater determinant $\Phi^{(0)}$, i.e. a Slater determinant constructed out of the single particle wave functions obtained from a closely related problem that can be calculated exactly, for example, from the wave functions of a particle in a harmonic potential. This Slater determinant is then used to obtain the HF energy (3.5),

$$E^{\text{HF}}[\rho] = \sum_{\alpha\beta} \rho_{\beta\alpha} + \frac{1}{2} \sum_{\alpha\beta\gamma\delta} \bar{v}_{\alpha\beta\delta\gamma} \rho_{\gamma\alpha} \rho_{\delta\beta} \quad (\rho_{\nu\mu} = \overline{a_{\mu}^{\dagger}} a_{\nu}), \quad (3.6)$$

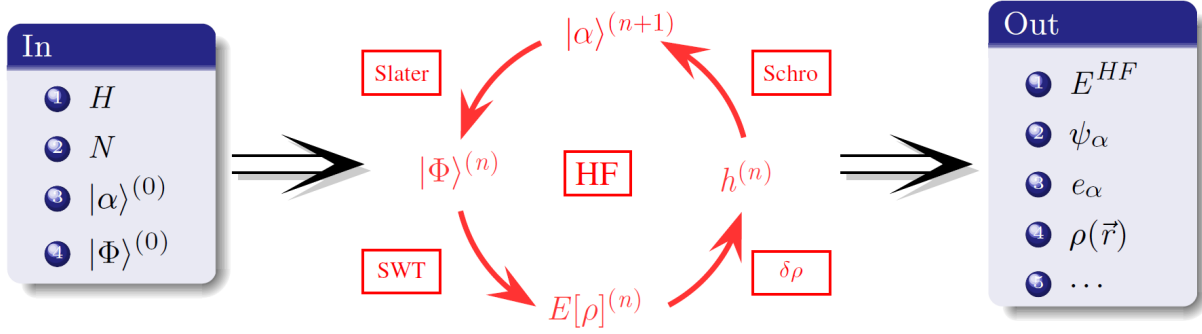


Figure 3.1: Schematic representation of the HF method. Picture taken from [47]. One inputs the Hamiltonian H , particle number N , single particle basis states $|\alpha\rangle^{(0)}$ and Slater determinant $|\Phi\rangle^{(0)}$. Starting from $|\Phi\rangle^{(n)}$, using standard Wick theorem, one obtains the HF energy $E[\rho]^{(n)}$. Subsequently, $E[\rho]^{(n)}$ is minimized w.r.t. ρ . This yields the HF mean field $h^{(n)}$. Through the Schrödinger equation, one obtains new single particle basis states $|\alpha\rangle^{(n+1)}$, which in turn can be used to construct a new Slater determinant $|\Phi\rangle^{(n+1)}$. After a number of cycles, the output is a minimized HF energy E^{HF} , single particle states ψ_α , single particle energies e_α , particle densities $\rho(\mathbf{r})$, etc.

with $\bar{v}_{\alpha\beta\delta\gamma} = v_{\alpha\beta\delta\gamma} - v_{\alpha\beta\gamma\delta}$. Minimization of the HF energy is realized with the Lagrange method of variation of parameters. This yields a new effective Hamiltonian, the Hartree-Fock mean field

$$h_{\alpha\gamma} \equiv \frac{\delta E^{\text{HF}}[\rho]}{\delta \rho_{\gamma\alpha}} = t_{\alpha\gamma} + U_{\alpha\gamma}^{\text{HF}}. \quad (3.7)$$

By diagonalizing the HF mean field, one obtains new single particle wave functions $\phi_{\alpha_i}^{(1)}$ and a new Slater determinant $\Phi^{(1)}$. It is possible to insert this HF mean field (3.7) and new Slater determinant $\Phi^{(1)}$ into equation (3.5) to recalculate the HF energy and minimize again. Iterating in this manner gives more and more accurate results. The process stops after a predefined number of iterations or when a certain threshold is met. One is left with a Slater determinant $\Phi^{(n)}$, which approximately describes the nucleus in the ground state, together with an estimate of the ground state energy [47]. A schematic representation of this process is shown in Fig. 3.1.

In coordinate space, this means that one solves the equations [47]

$$h\psi_\alpha \equiv \frac{\delta E^{\text{HF}}[\psi_\alpha]}{\delta \psi_\alpha^*} = -\frac{\hbar^2}{2m}\Delta\psi_\alpha + U^H\psi_\alpha + U^F\psi_\alpha = e_\alpha\psi_\alpha \quad (3.8)$$

with the HF energy given by

$$E^{\text{HF}} = \int d^3\mathbf{r}_1 d^3\mathbf{r}_2 \left[\delta(\mathbf{r}_1 - \mathbf{r}_2) \frac{\hbar^2}{2m} \nabla_1 \cdot \nabla_2 \rho_{\mathbf{r}_1\mathbf{r}_2} + \frac{1}{2} v(\mathbf{r}_1 - \mathbf{r}_2) (\rho_{\mathbf{r}_1\mathbf{r}_1} \rho_{\mathbf{r}_2\mathbf{r}_2} - \rho_{\mathbf{r}_1\mathbf{r}_2} \rho_{\mathbf{r}_2\mathbf{r}_1}) \right], \quad (3.9)$$

where $\rho_{\mathbf{r}_1\mathbf{r}_2} \equiv \sum_{i=1}^A \psi_i^*(\mathbf{r}_2)\psi_i(\mathbf{r}_1)$ and $\langle \mathbf{r}_1, \mathbf{r}_2 | v(1, 2) | \mathbf{r}'_1, \mathbf{r}'_2 \rangle = v(\mathbf{r}_1 - \mathbf{r}_2) \delta(\mathbf{r}_1 - \mathbf{r}'_1) \delta(\mathbf{r}_2 - \mathbf{r}'_2)$. The Hartree and Fock potentials are [47]

$$U^H\psi_\alpha(\mathbf{r}_1) \equiv \int d^3\mathbf{r}_2 v(\mathbf{r}_1 - \mathbf{r}_2) \rho_{\mathbf{r}_1\mathbf{r}_2} \psi_\alpha(\mathbf{r}_2) \quad (3.10)$$

and

$$U^F\psi_\alpha(\mathbf{r}_1) \equiv - \int d^3\mathbf{r}_2 v(\mathbf{r}_1 - \mathbf{r}_2) \rho_{\mathbf{r}_1\mathbf{r}_2} \psi_\alpha(\mathbf{r}_2). \quad (3.11)$$

3.2 Random phase approximation

An approximation method that calculates observables, such as excitation energies and ground-state transition strength directly, is the random phase approximation (RPA). Wave functions are essentially treated as secondary. The RPA can be derived in three ways: the Green's function method, time-dependent Hartree-Fock theory and the method of linearized equations of motion. The method presented here, will be the equations of motion method followed by D. J. Rowe [48].

The equations of motion of a harmonic oscillator are given by

$$[H, O^\dagger] = \omega O^\dagger, \quad [H, O] = -\omega O, \quad (3.12)$$

where ω is the frequency and O^\dagger and O are boson operators with commutation relation

$$[O, O^\dagger] = 1. \quad (3.13)$$

One might suspect that modeling the particle-hole pairs as bosons will violate the Pauli principle. However, this derivation will lead to an exact closed expression which does not violate the Pauli principle.

These operators act on the set of eigenfunctions as

$$O|0\rangle = 0, \quad O^\dagger|0\rangle = |1\rangle, \quad (3.14)$$

and

$$O|n\rangle = \sqrt{n}|n-1\rangle, \quad O^\dagger|n\rangle = \sqrt{n+1}|n+1\rangle, \quad (3.15)$$

with eigenvalues

$$E_n = \left(n + \frac{1}{2}\right)\omega. \quad (3.16)$$

The solution is

$$O^\dagger = \sum_{n=0}^{\infty} \sqrt{n+1}|n+1\rangle\langle n|. \quad (3.17)$$

It would be convenient if this approach could be used for a more general Hamiltonian, such as a nuclear Hamiltonian. For this purpose, postulate a Hamiltonian that is harmonic up to some level m , i.e.

$$E_{n+1} - E_n = \omega \quad \forall n \leq m. \quad (3.18)$$

This way, one can redefine O^\dagger as

$$O^\dagger = \sum_{n=0}^m \sqrt{n+1}|n+1\rangle\langle n| + \sum_{p,q>m} C_{pq}|p\rangle\langle q|. \quad (3.19)$$

Note that equations (3.12) and (3.13) are still valid for $n \leq m$. These equations can be rewritten in a more general form:

$$[H, O^\dagger] = \omega O^\dagger + P, \quad [H, O] = -\omega O - P^\dagger, \quad (3.20)$$

and

$$[O, O^\dagger] = 1 + Q, \quad (3.21)$$

with $P|n\rangle = P^\dagger|n\rangle = Q|n\rangle = Q^\dagger|n\rangle = 0$ for all $n \leq m$.

This can be put in a more simple form. By multiplying equations (3.20) from the left with the random operators R and R^\dagger , respectively, and subsequently taking the expectation value of both equations with respect to a wave function $|\phi\rangle$, the Hermitian conjugate of the second equation can be added to the first equation to obtain:

$$\langle\phi|[R, [H, O^\dagger]]|\phi\rangle = \omega\langle\phi|[R, O^\dagger]|\phi\rangle, \quad (3.22)$$

given that $|\phi\rangle = \sum_{n=0}^m c_n|n\rangle$. Taking instead the Hermitian conjugate of the first equation yields:

$$\langle\phi|[R, [H, O]]|\phi\rangle = -\omega\langle\phi|[R, O]|\phi\rangle \quad (3.23)$$

Observe, that this is the Hermitian conjugate of expression (3.22), so that only one of them must be solved.

When solving for O^\dagger , solutions of (3.22) are independent of $|\phi\rangle$. It is at this point, however, that one must realize that the nuclear Hamiltonian is generally not harmonic. For this reason, it is necessary to restrict oneself to the ground state wave function $|0\rangle$. Unfortunately, ground-state wave functions are usually not known exactly. An approximate wave function $|\psi\rangle$ must then be used, much like in the HF method. As a matter of fact, the HF wave functions may be used for this purpose. The way this approach is constructed ensures that the solutions are as independent of $|\psi\rangle$ as possible.

Approximate ground state wave functions $|\psi\rangle$ are generally not Hermitian. Note that in the limit where $|\psi\rangle$ is an eigenstate and

$$\langle\psi|[H, [R, O^\dagger]]|\psi\rangle = 0, \quad (3.24)$$

equation (3.22) can be written as

$$\langle\psi|[R, H, O^\dagger]|\psi\rangle = \omega\langle\psi|[R, O^\dagger]|\psi\rangle \quad (3.25)$$

with

$$2[R, H, O^\dagger] \equiv [R, [H, O^\dagger]] + [[R, H], O^\dagger]. \quad (3.26)$$

This way Hermiticity is restored.

Let $\mathcal{B} = \{a_\alpha, a_\alpha^\dagger\}$ be the basis of some Hilbert space \mathcal{H} . Solutions to O and O^\dagger are found by expanding

$$O_\mu^\dagger = \sum_\alpha X_\alpha(\mu) a_\alpha^\dagger. \quad (3.27)$$

Equation 3.25 becomes

$$\sum_\beta \langle\psi|[a_\alpha, H, a_\beta^\dagger]|\psi\rangle X_\beta(\mu) = \omega_\mu \sum_\beta \langle\psi|[a_\alpha, a_\beta^\dagger]|\psi\rangle X_\beta(\mu) \quad (3.28)$$

Let us adopt the Greek letters α, β, γ , etc. for particle states, i.e. states above the Fermi energy, and the Roman letters i, j, k , etc. for hole states, i.e. states below the Fermi energy. The RPA's first assumption is that excited states are created by a linear combination of 1-particle-1-hole excitations of the ground state. The second assumption is that a_α and a_α^\dagger are the creation and annihilation operators, assuming the particle-hole vacuum $|\rangle$, for which

$$\langle|a_i^\dagger[H, a_j]|\rangle = \delta_{ij}e_i \quad (3.29)$$

$$\langle|a_\alpha[H, a_j^\dagger]|\rangle = \delta_{\alpha\beta}e_\alpha. \quad (3.30)$$

This is essentially the HF representation with e the single particle energies.

The operators O^\dagger are of the form

$$O^\dagger = \sum_{\alpha,i} (X_{\alpha,i} a_\alpha^\dagger a_i + Y_{\alpha,i} a_i^\dagger a_\alpha) \quad (3.31)$$

to replicate the particle-hole excitations. By inserting this into (3.28), in matrix form, the RPA equations become

$$\begin{pmatrix} A & B \\ B^\dagger & A^* \end{pmatrix} \begin{pmatrix} X \\ Y \end{pmatrix} = \omega \begin{pmatrix} U & 0 \\ 0 & -U^* \end{pmatrix} \begin{pmatrix} X \\ Y \end{pmatrix} \quad (3.32)$$

where

$$A_{\alpha i \beta j} = \langle \psi | [a_i^\dagger a_\alpha, H, a_\beta^\dagger a_j] | \psi \rangle \quad (3.33)$$

$$B_{\alpha i \beta j} = -\langle \psi | [a_i^\dagger a_\alpha, H, a_j^\dagger a_\beta] | \psi \rangle \quad (3.34)$$

$$U_{\alpha i \beta j} = \langle \psi | [a_i^\dagger a_\alpha, a_\beta^\dagger a_j] | \psi \rangle. \quad (3.35)$$

A and U are Hermitian matrices and B is a symmetric matrix. Setting $|\psi\rangle = | \rangle$,

$$A_{\alpha i \beta j} = \delta_{\alpha\beta} \delta_{ij} (e_\alpha - e_i) + V_{\alpha j i \beta} \quad (3.36)$$

$$B_{\alpha i \beta j} = V_{\alpha \beta i j} \quad (3.37)$$

$$U_{\alpha i \beta j} = \delta_{\alpha\beta} \delta_{ij}. \quad (3.38)$$

A great number of extensions to RPA exist, such as continuum RPA (CRPA), quasi-particle RPA (QRPA), etc.

An extension of the RPA by Tohyama (2014) [49] was used to derive the ground-state occupation numbers of nuclear shells. The occupation numbers are obtained from the one-body density matrix

$$n_{\alpha\alpha'}(t) = \langle \Phi(t) | a_{\alpha'}^\dagger a_\alpha | \Phi(t) \rangle \quad (3.39)$$

with $|\Phi(t)\rangle = e^{-\frac{iHt}{\hbar}} |\Phi(0)\rangle$ the time-dependent total wave function.

3.3 Interactions and potentials

The nuclear interactions in the aforementioned methods still need to be defined, i.e. the Hamiltonian H must be specified. This Hamiltonian is usually an effective interaction that accounts for all the interactions involved in the composition of a bound nucleus (strong and weak nuclear interactions and electromagnetism). A convenient choice is the Skyrme interaction (section 3.3.1).

Alternatively, it is possible to acquire the particle wave functions directly from an effective potential through the Schrödinger equation. This can be done for the Woods-Saxon potential (section 3.3.2).

3.3.1 Skyrme interaction

The Skyrme interaction is an effective nucleon-nucleon interaction used to reproduce ground state energies or excited state energies in nuclei. It is a zero-range interaction

that has both density- and momentum-dependent parts. A lot of different parametrizations of this interaction are possible and a lot of variations exist.

The original Skyrme interaction consists of a two-body and a three-body part, and is of the form [50]

$$U_{\text{Skyrme}} = \sum_{i<j} v_{ij}^{(2)} + \sum_{i<j<k} v_{ijk}^{(3)}. \quad (3.40)$$

The two-body potential in this expression is given by [50]

$$v_{12}^{(2)} = t_0(1 + x_0 P_\sigma) \delta(\mathbf{r}_1 - \mathbf{r}_2) \quad (3.41)$$

$$+ \frac{1}{2} t_1 (\delta(\mathbf{r}_1 - \mathbf{r}_2) k^2 + k'^2 \delta(\mathbf{r}_1 - \mathbf{r}_2)) \quad (3.42)$$

$$+ t_2 \mathbf{k}' \cdot \delta(\mathbf{r}_1 - \mathbf{r}_2) \mathbf{k} \quad (3.43)$$

$$+ i W_0 (\boldsymbol{\sigma}_1 + \boldsymbol{\sigma}_2) \cdot \mathbf{k}' \times \delta(\mathbf{r}_1 - \mathbf{r}_2) \mathbf{k} \quad (3.44)$$

where \mathbf{k} and \mathbf{k}' are the operators $\frac{1}{2i}(\nabla_1 - \nabla_2)$, acting on the right, and $-\frac{1}{2i}(\overleftarrow{\nabla}_1 - \overleftarrow{\nabla}_2)$, acting on the left. P_σ is the spin exchange operator $\frac{1}{2}(1 + \boldsymbol{\sigma}_1 \cdot \boldsymbol{\sigma}_2)$ and $\boldsymbol{\sigma} = (\sigma_x, \sigma_y, \sigma_z)^T$ are the Pauli matrices,

$$\sigma_x = \begin{pmatrix} 0 & 1 \\ 1 & 0 \end{pmatrix}, \quad \sigma_y = \begin{pmatrix} 0 & -i \\ i & 0 \end{pmatrix}, \quad \sigma_z = \begin{pmatrix} 1 & 0 \\ 0 & -1 \end{pmatrix}. \quad (3.45)$$

The three-body potential is given by [42, 50]

$$v_{123}^{(3)} = t_3 \delta(\mathbf{r}_1 - \mathbf{r}_2) \delta(\mathbf{r}_1 - \mathbf{r}_3). \quad (3.46)$$

For HF calculations of even-even nuclei, this last term, the three-body term, can be transformed into a density-dependent two-body potential [42]

$$\frac{1}{6} t_3 (1 + P_\sigma) \delta(\mathbf{r}_1 - \mathbf{r}_2) \rho \left(\frac{\mathbf{r}_1 - \mathbf{r}_2}{2} \right). \quad (3.47)$$

Presently, different variations of the Skyrme interactions are being used. The extended Skyrme interaction (SkE) contains all the original Skyrme two-body terms (3.41) - (3.44) and includes the Coulomb two-body term [50]

$$v_{12}^{\text{C}} = \frac{e^2}{|\mathbf{r}_1 - \mathbf{r}_2|}. \quad (3.48)$$

Additionally, a fraction $1 - x_3$ of the three-body term (3.46) is transformed into the density-dependent two-body potential (3.47), i.e.

$$v_{12}^{\text{D}} = \frac{1}{6} t_3 (1 - x_3) (1 + P_\sigma) \delta(\mathbf{r}_1 - \mathbf{r}_2) \rho \left(\frac{\mathbf{r}_1 - \mathbf{r}_2}{2} \right). \quad (3.49)$$

The remaining fraction x_3 of the three-body potential (3.46) is kept the same:

$$v_{123}^{\text{D}} = x_3 t_3 \delta(\mathbf{r}_1 - \mathbf{r}_2) \delta(\mathbf{r}_2 - \mathbf{r}_3), \quad (3.50)$$

and an additional momentum-dependent three-body term is added: [50]

$$v_{123}^M = \frac{1}{6}t_4[(k_{12}'^2 + k_{23}'^2 + k_{31}'^2)\delta(\mathbf{r}_1 - \mathbf{r}_2)\delta(\mathbf{r}_1 - \mathbf{r}_3) + \delta(\mathbf{r}_1 - \mathbf{r}_2)\delta(\mathbf{r}_1 - \mathbf{r}_3)(k_{12}^2 + k_{23}^2 + k_{31}^2)]. \quad (3.51)$$

In a time-reversal invariant nuclear system, the HF calculations become independent of the fraction parameter x_3 . To visualize this, the contributions to the ground state energy of (3.49) and (3.50) are [51]

$$E^{HF}(v_{12}^D) = \frac{1}{4}t_3(1 - x_3) \int \rho_p(\mathbf{r})\rho_n(\mathbf{r})\rho_{\text{tot}}(\mathbf{r})d^3\mathbf{r} + \frac{1}{12}t_3(1 - x_3) \int \mathbf{S}_p(\mathbf{r}) \cdot \mathbf{S}_n(\mathbf{r})\rho_{\text{tot}}(\mathbf{r})d^3\mathbf{r} \quad (3.52)$$

and

$$E^{HF}(v_{123}^D) = \frac{1}{4}t_3x_3 \int \rho_p(\mathbf{r})\rho_n(\mathbf{r})\rho_{\text{tot}}(\mathbf{r})d^3\mathbf{r} - \frac{1}{4}t_3x_3 \int [\mathbf{S}_p^2(\mathbf{r})\rho_n(\mathbf{r}) + \mathbf{S}_n^2(\mathbf{r})\rho_p(\mathbf{r})] d^3\mathbf{r}, \quad (3.53)$$

where $\rho_{\text{tot}}(\mathbf{r})$ is the total particle density, $\rho_\tau(\mathbf{r})$ is the nucleon density and $\mathbf{S}_\tau(\mathbf{r})$ the spin density

$$\mathbf{S}_\tau(\mathbf{r}) = \sum_{\alpha\gamma} \rho_{\alpha\gamma} \phi_\alpha^*(\mathbf{r}, \sigma, \tau) \boldsymbol{\sigma} \phi_\gamma(\mathbf{r}, \sigma', \tau) \quad (\rho_{\nu\mu} = \overline{a_\mu^+} a_\nu). \quad (3.54)$$

The time-reversal symmetry causes the spin density $\mathbf{S}_\tau(\mathbf{r})$ to vanish, making both contributions equivalent.

Due to the δ functions that appear in the description of the extended Skyrme potential, the HF energy will only depend on three densities: [42, 51]

$$\rho_\tau(\mathbf{r}) = \sum_{i,\sigma} |\phi_{\alpha_i}(\mathbf{r}, \sigma, \tau)|^2, \quad (3.55)$$

$$\tau_\tau(\mathbf{r}) = \sum_{i,\sigma} |\nabla \phi_{\alpha_i}(\mathbf{r}, \sigma, \tau)|^2, \quad (3.56)$$

$$\mathbf{J}_\tau(\mathbf{r}) = -i \sum_{i,\sigma,\sigma'} \phi_{\alpha_i}^*(\mathbf{r}, \sigma, \tau) [(\nabla \phi_{\alpha_i}(\mathbf{r}, \sigma', \tau)) \times \langle \sigma | \boldsymbol{\sigma} | \sigma' \rangle], \quad (3.57)$$

the nucleon density, kinetic energy and spin density, respectively. The HF equations become [51]

$$-\nabla \left[\frac{\hbar^2}{2m_\tau^*(\mathbf{r})} \nabla \phi_\alpha(\mathbf{r}) \right] + [U_\tau(\mathbf{r}) - i\mathbf{W}_\tau(\mathbf{r}) \cdot (\nabla \times \boldsymbol{\sigma})] \phi_\alpha(\mathbf{r}) = e_\alpha \phi_\alpha(\mathbf{r}). \quad (3.58)$$

Herein, the effective mass is

$$\frac{\hbar^2}{2m_\tau^*(\mathbf{r})} = \frac{\hbar^2}{2m_\tau} + \frac{1}{4}(t_1 + t_2)\rho_{\text{tot}}(\mathbf{r}) + \frac{1}{8}(t_2 - t_1)\rho_\tau(\mathbf{r}) + \frac{1}{24}t_4(\rho_{\text{tot}}^2(\mathbf{r}) - \rho_\tau^2(\mathbf{r})). \quad (3.59)$$

Table 3.1: Values of the parameters in SkE2.

t_0 (MeV fm ³)	t_1 (MeV fm ⁵)	t_2 (MeV fm ⁵)	t_3 (MeV fm ⁶)	x_0	W_0 (MeV fm ⁵)	t_4 (MeV fm ⁸)
-1299.30	802.41	-67.89	19558.96	0.270	120	-15808.79

The potential $U_\tau(\mathbf{r})$ is

$$\begin{aligned}
U_\tau(\mathbf{r}) = & t_0 \left[\left(1 + \frac{1}{2}x_0\right)\rho_{\text{tot}} - \left(\frac{1}{2} + x_0\right)\rho_\tau \right] + \frac{1}{4}(t_1 + t_2)\tau_{\text{tot}} + \frac{1}{8}(t_2 - t_1)\tau_\tau \\
& + \frac{1}{8}(t_2 - 3t_1)\nabla^2\rho_{\text{tot}} + \frac{1}{16}(3t_1 + t_2)\nabla^2\rho_\tau + \frac{1}{4}t_3(\rho_{\text{tot}}^2 - \rho_\tau^2) \\
& - \frac{1}{2}W_0(\nabla \cdot \mathbf{J}_{\text{tot}} + \nabla \cdot \mathbf{J}_\tau) + \delta_{\tau\nu}v_{12}^C + \frac{1}{24}t_4 \left[2\rho_{\text{tot}}\tau_{\text{tot}} - 2\rho_\tau\tau_\tau \right. \\
& \left. + \frac{5}{2}\rho_\tau\nabla^2\rho_\tau - \frac{5}{2}\rho_{\text{tot}}\nabla^2\rho_{\text{tot}} + \frac{5}{4}(\nabla\rho_\tau)^2 - \frac{5}{4}(\nabla\rho_{\text{tot}})^2 + \frac{1}{2}\mathbf{J}_{\tau'}^2 \right]. \quad (3.60)
\end{aligned}$$

Finally, $\mathbf{W}_\tau(\mathbf{r})$ is

$$\mathbf{W}_\tau(\mathbf{r}) = \frac{1}{2}W_0(\nabla\rho_{\text{tot}} + \nabla\rho_\tau) + \frac{1}{8}(t_1 - t_2)\mathbf{J}_\tau(\mathbf{r}) + \frac{1}{24}t_4\rho_{\tau'}\mathbf{J}_\tau(\mathbf{r}). \quad (3.61)$$

In these expressions $\tau' \neq \tau$.

The particular parametrization used in this work is SkE2. The values of the parameters are displayed in Table 3.1.

3.3.2 Woods-Saxon

The Woods-Saxon (WS) potential is a mean field potential. The idea behind this potential is a scalar interaction between a nucleon and a core. For a nucleus of Z protons and N neutrons with mass number $A = Z + N$, the mass number of the core is $A' = A - 1$ [52].

The WS potential shape is given by [52]

$$U(r) = -\frac{U_0}{1 + \exp\left(\frac{r-R_0}{a_0}\right)} - \frac{1}{2\mu^2 r} \frac{d}{dr} \left(\frac{U_{\text{so}}}{1 + \exp\left(\frac{r-R_{\text{so}}}{a_{\text{so}}}\right)} \right) \mathbf{1} \cdot \boldsymbol{\sigma} + V_C(r), \quad (3.62)$$

with the reduced mass

$$\mu = \left(\frac{1}{m_{p(n)}} + \frac{1}{M'} \right)^{-1}, \quad (3.63)$$

where $m_{p(n)}$ is the proton (neutron) mass and M' is the mass of the core. The first term is the traditional potential shown in Fig. 3.2. Here U_0 is the depth of the well, a_0 is the surface thickness of the nucleus and R_0 is the nuclear radius. The second term takes care of spin-orbit coupling. Here, m_π is the pion mass. The constants U_{so} , R_{so} and a_{so} are strength, radius and diffuseness of the spin-orbit term, respectively. The last term is the

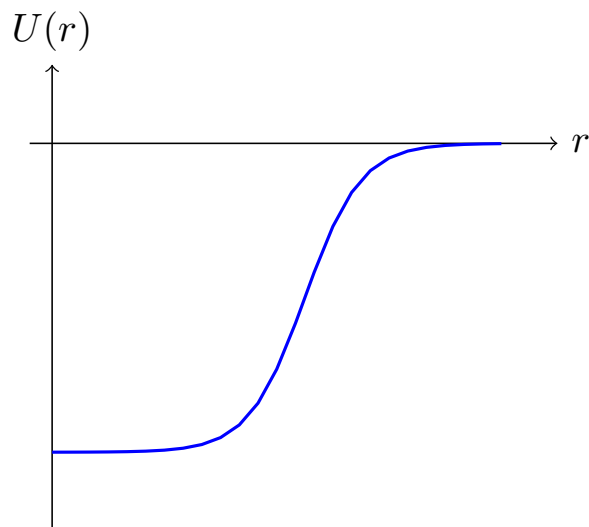


Figure 3.2: Schematic representation of the Woods-Saxon potential.

Coulomb potential for which

$$V_C(r) = \begin{cases} \frac{Ze^2}{2R_C} \left(3 - \left(\frac{r}{R_C} \right)^2 \right) & r \leq R_C \\ \frac{Ze^2}{r} & r > R_C, \end{cases} \quad (3.64)$$

where R_C is the radius of the uniform charge distribution [52, 53]. For calculations, one usually chooses $a_{\text{so}} = a_0$ and $R_{\text{so}} = R_C = R_0$. Also note that $V_C(r) = 0$ for neutrons [53].

4 | Properties of $\text{CE}\nu\text{NS}$

Following the derivation of the $\text{CE}\nu\text{NS}$ cross section in chapter 2 and the description of the nucleus in chapter 3, it is possible to investigate some of the properties of $\text{CE}\nu\text{NS}$.

In this chapter, we look at the maximum recoil energy for different nuclei and how the cross section behaves under the influence of nuclear parameters. How $\text{CE}\nu\text{NS}$ compares to other reaction channels is discussed thereupon. We conclude the chapter with a demonstration of the sensitivity to the weak mixing angle.

4.1 Maximum recoil energy

As substantiated by kinematics, the kinetic energy distribution of the recoiling nucleus is limited from above, i.e. there is a maximum recoil energy. This is the largest amount of kinetic energy that can be transferred from the neutrino to the nucleus. When the recoil energy surpasses its maximum, the CE ν NS differential cross section (2.37) must vanish. Therefore, the maximum recoil energy can be found by equating the differential cross section to zero. This gives

$$T_{\max} = \frac{2E^2}{M + 2E}, \quad (4.1)$$

which can be approximated for large nuclei, since the mass of the nucleus is about two orders of magnitude larger than the energy of the incoming neutrino:

$$T_{\max} = \frac{2E^2}{M}. \quad (4.2)$$

Fig. 4.1 shows the maximum recoil energy as a function of the energy of the incoming neutrino for the nuclei: ^{12}C (blue), ^{16}O (red), ^{40}Ar (yellow), ^{40}Ca (purple) and ^{56}Fe (green). The masses used in the calculation are displayed in Tab. 4.1. The maximum recoil energy increases with increasing energy of the incoming neutrino. Additionally, it is larger for lighter nuclei.

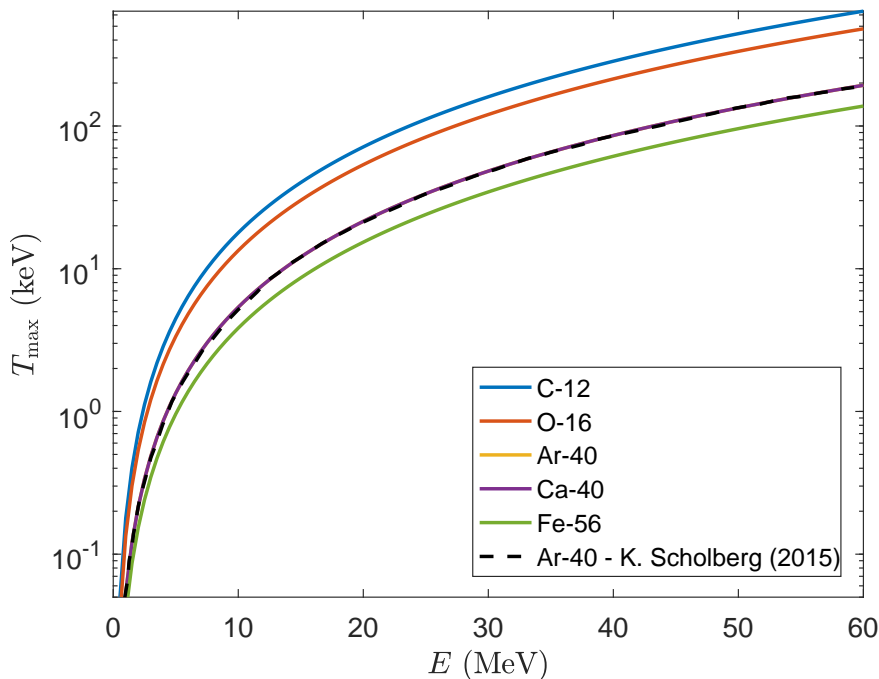


Figure 4.1: The maximal recoil energy for a number of different nuclei as a function of the energy of the incoming neutrino. From low mass to high mass: ^{12}C (blue), ^{16}O (red), ^{40}Ar (yellow), ^{40}Ca (purple) and ^{56}Fe (green). The ^{40}Ar line is not visible since it overlaps with ^{40}Ca . The ^{40}Ar line is compared to the result of K. Scholberg (2015) [3] (black,dashed).

Table 4.1: Nuclear masses and weak charge of the used nuclei. Nuclear masses were calculated using $M = M_A - ZM_e + B_e(Z)$, where M_A is the atomic mass, M_e is the electron mass and $B_e(Z)$ is the total binding energy of all the removed electrons $B_e(Z) = 14.4381Z^{2.39} + 1.55468 \times 10^{-6}Z^{5.35}$ eV [54]. Weak charges were calculated using the definition (2.27).

Nucleus	mass M (amu)	weak charge Q_W
^{12}C	11.996710	-5.3352
^{16}O	15.990528	-7.1136
^{40}Ar	39.952524	-20.0056
^{40}Ca	39.951639	-17.7840
^{56}Fe	55.920710	-27.1192

This is of importance to CE ν NS detectors and sources. Small recoils are difficult to detect. The higher the recoil energy, the easier it is to detect the recoil. It is, therefore, advantageous to use a source that emits neutrinos at a higher energy.

4.2 Influence of nuclear parameters

From the CE ν NS differential cross section (2.37), the nuclear properties that affect the cross section are the weak charge Q_W , the mass M and the form factor $F(q^2)$. The mass and the weak charge are closely related, therefore, they will be treated simultaneously. The form factor is rather complex and will be treated separately.

4.2.1 Mass and weak charge

The mass and the weak charge of a nucleus are closely related since they both depend on the amount of nucleons in the nucleus. A large number of nucleons leads to both a larger mass and, from Eq. (2.27), $Q_W \equiv (1 - 4 \sin^2 \theta_W)Z - N$, a larger weak charge. Overall, larger nucleon numbers leads to larger CE ν NS cross sections. As supported by the definition of the weak charge, every type of nucleus has a unique weak charge. This makes it impossible to vary the mass of the nucleus while keeping the weak charge constant. The opposite is possible to a certain degree. One cannot find nuclei with exactly the same mass, however, isobaric nuclei have approximately the same mass. It makes sense, then, to look at the effect of the number of nucleons on the cross section and to compare the neutron and proton numbers in isobars.

In the following calculations, the form factor is assumed $F(q^2) = 1$. A comparison of the cross section of nuclei with different masses is shown in Fig. 4.2. Additionally, the ratio is plotted in Fig. 4.3. The masses and weak charges used in the calculations are displayed in Tab. 4.1.

The cross section grows with neutrino energy. The increase between 20 MeV and 50 MeV is about an order of magnitude for each nucleus. As expected, the cross section is larger for heavier nuclei. The ratio stays approximately constant over the employed range of neutrino energies.

^{40}Ar and ^{40}Ca are examples of two isobaric nuclei. By comparing the cross sections of these nuclei, the behavior of the cross section with respect to the weak charge of the

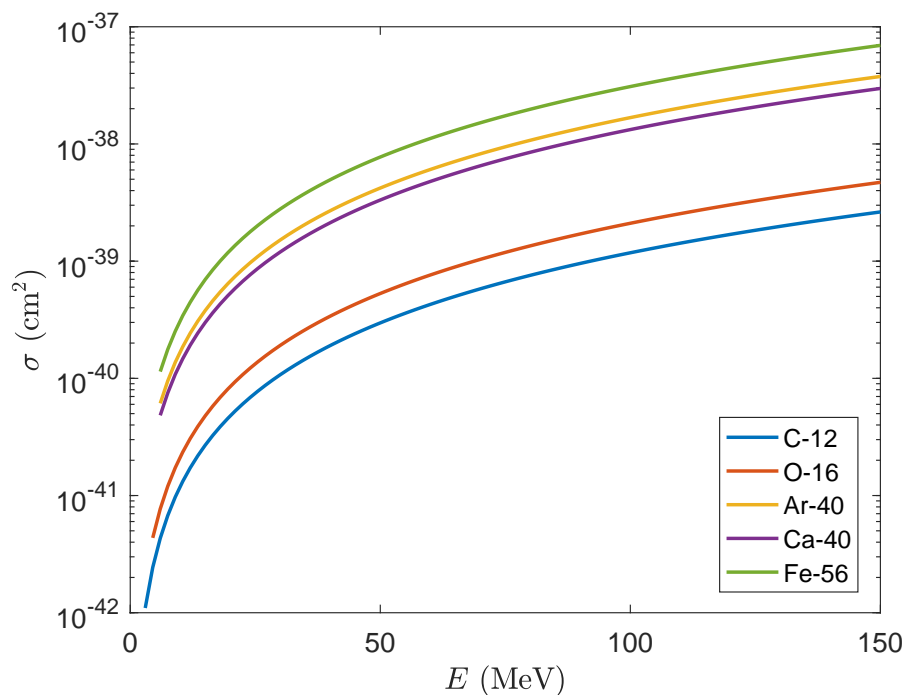


Figure 4.2: Comparison of the cross section for four different nuclei as a function of the energy of the incoming neutrino. From low mass to high mass: ^{12}C (blue), ^{16}O (red), ^{40}Ar (yellow), ^{40}Ca (purple) and ^{56}Fe (green). To emphasize the effect of the increasing mass, no form factor was used in this calculation.

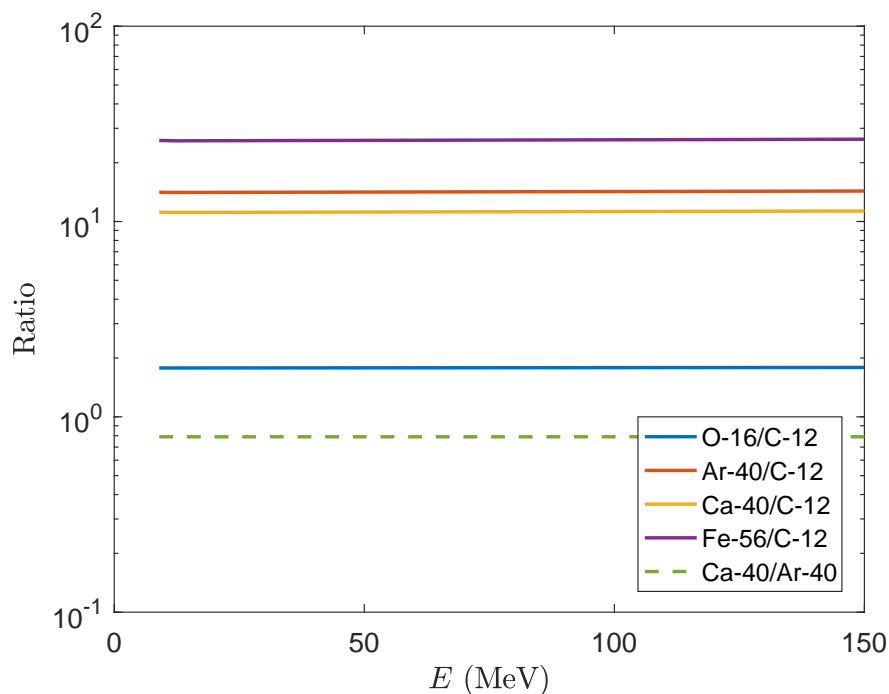


Figure 4.3: Comparison of the ratio of the cross sections of different nuclei as a function of the energy of the incoming neutrino. The used cross sections are from Fig. 4.2.

nucleus becomes apparent. ^{40}Ar and ^{40}Ca have masses 39.952524 amu and 39.951639 amu, respectively. One can see that the ^{40}Ar cross section is larger than the ^{40}Ca cross section. The small difference in mass is not enough to explain the difference in cross section. Instead the difference can be attributed to the larger neutron number of ^{40}Ar . This nucleus contains 18 protons and 22 neutrons as opposed to ^{40}Ca , which contains 20 protons and 20 neutrons. Therefore, ^{40}Ar has a larger squared weak charge Q_W^2 .

Regarding CE ν NS detectors, the increase of the cross section with mass and weak charge has an important implication. In section 4.1, we saw that the maximum recoil increases for lighter nuclei. The choice of detector material is then a trade-off between larger cross section and larger maximum recoil, which translates to higher event rate or larger allowed detection thresholds. The latter means that the necessary threshold for detection is allowed to be higher.

4.2.2 Form factor

It is possible to look at the effect of the form factor on the cross section. Fig. 4.4 and 4.5 show the differential cross section and the cross section for ^{12}C , respectively, calculated using the HF+SkE2 wave functions. The corresponding weak charge density and form factor are shown in Fig. 4.6.

In Fig. 4.4, the form factor causes a reduction of the differential cross section. The points of intersection with the horizontal and vertical axes remain the same. The effect is larger for higher neutrino energies. In addition, note that the slope of the differential cross section becomes less steep with increasing energy of the incoming neutrino. This

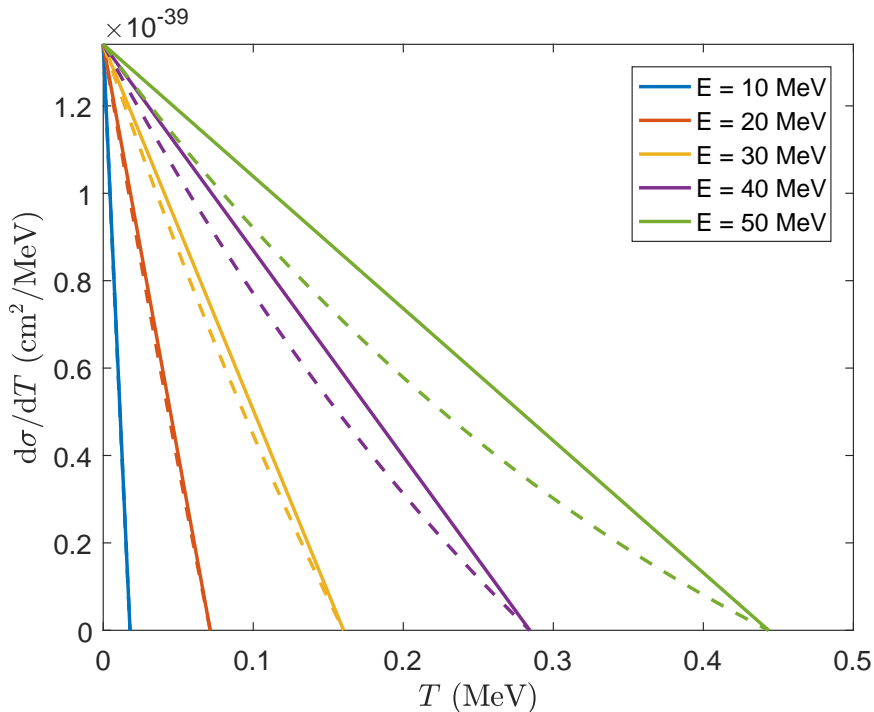


Figure 4.4: The differential cross section for a ^{12}C nucleus as a function of the nuclear recoil. The continuous lines represent a point-like particle, while the dashed lines include the form factor. The form factor was calculated using a HF + SkE2 approach.

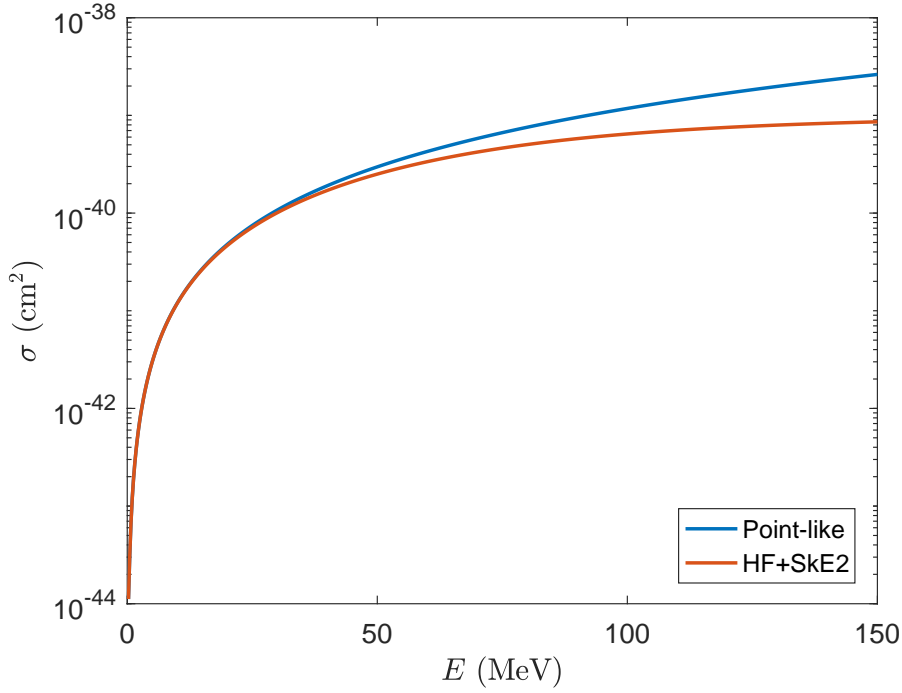


Figure 4.5: The cross section for a ^{12}C nucleus as a function of the energy of the incoming neutrino. The blue line represents the nucleus as a point-like particle, while the red line includes the form factor. The form factor was calculated using a HF + SkE2 approach.

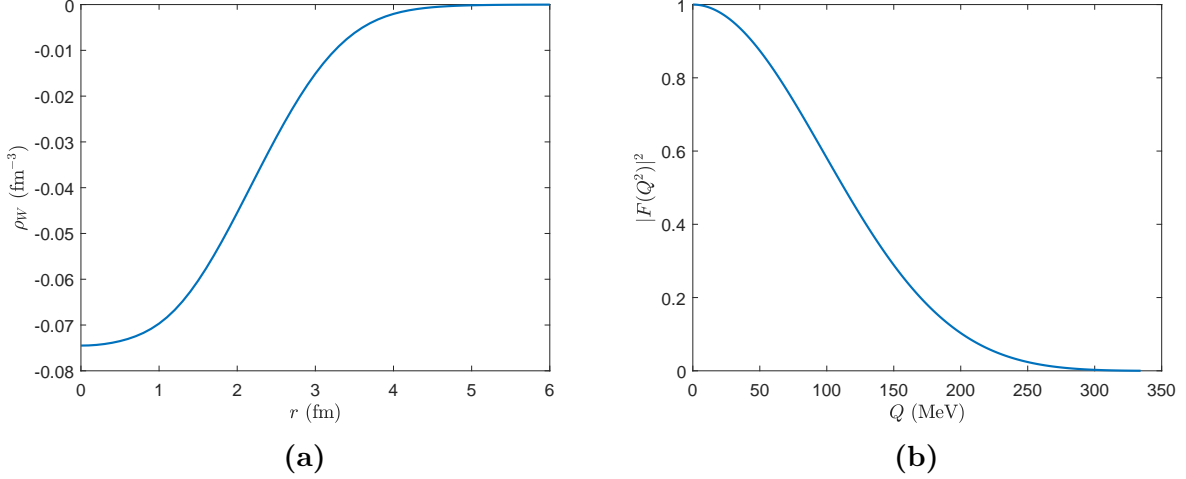


Figure 4.6: Left: Weak charge density distribution for a ^{12}C nucleus. Right: Square of the weak form factor of a ^{12}C nucleus. Both calculated using a HF + SkE2 approach.

indicates the increasing maximum recoil energy of section 4.1. The point of intersection with the horizontal axis moves to larger values of T , meaning that the allowed range of recoil energies after an interaction grows.

Per definition, the lowering of the differential cross section after inclusion of the form factor affects the total cross section. In general, the form factor lowers the cross section. For low energies of the incoming neutrino, the cross section remains approximately that of a point-like particle. For higher energies, the difference becomes larger.

This decrease reflects the spreading of the interaction owing to the finite size of the nucleus. In section 2.4, it was explained that the neutrino sees the nucleus more or less as a point-like particle when $|\mathbf{q}| < 1/R$. In the case of ^{12}C , the nuclear radius can be estimated from Fig. 4.6a, which gives $1/R \approx 70$ MeV. Since $|\mathbf{q}| = |\mathbf{k}_1 - \mathbf{p}_1| = 2E \sin \frac{\theta}{2}$ (with θ the scattering angle), the condition is satisfied for $E \approx 35$ MeV. Indeed, Fig. 4.5 shows that for energies below 35 MeV the cross section remains approximately point-like.

4.2.3 Combined results

Applying form factors (Fig. 4.9) to the nuclei of Fig. 4.2, results in Fig. 4.7. Fig. 4.8 shows the ratio of the cross sections.

The cross section increases more slowly due to the form factor. At low energies, the cross section remains approximately point-like. However, all cross sections have been flattened out at higher energies, i.e. they are lower. From the ratio, one can see that the form factor affects heavy nuclei more strongly. The ratios of ^{40}Ar , ^{40}Ca and ^{56}Fe to ^{12}C noticeably decrease at higher energies. This stems from the fact that these nuclei have larger weak charge distributions, as substantiated by the form factors in Fig. 4.9.

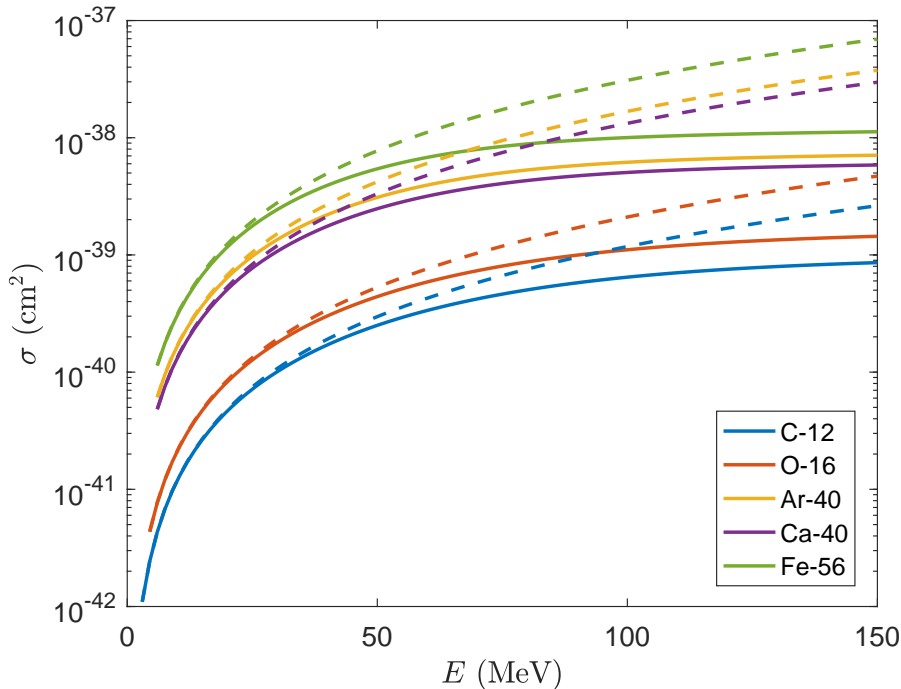


Figure 4.7: Comparison of the cross section for different nuclei as a function of the energy of the incoming neutrino. From low mass to high mass: ^{12}C (blue), ^{16}O (red), ^{40}Ar (yellow), ^{40}Ca (purple) and ^{56}Fe (green). The dashed lines are the point-like cross sections, while the full lines are the cross sections in a HF+SkE2 approach.

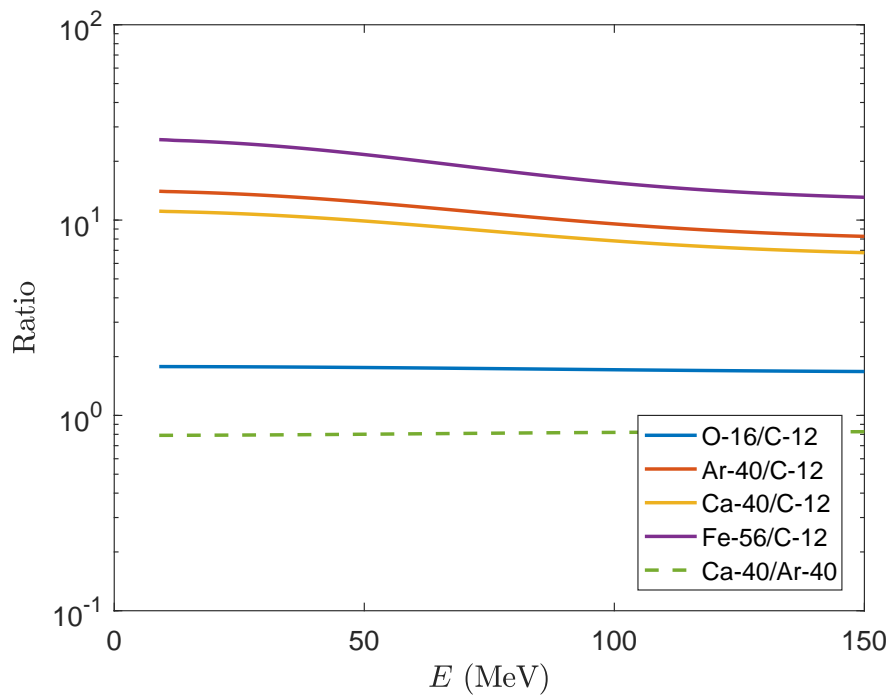


Figure 4.8: Comparison of the ratio of the cross sections of different nuclei as a function of the energy of the incoming neutrino. The cross sections correspond to those of Fig. 4.7.

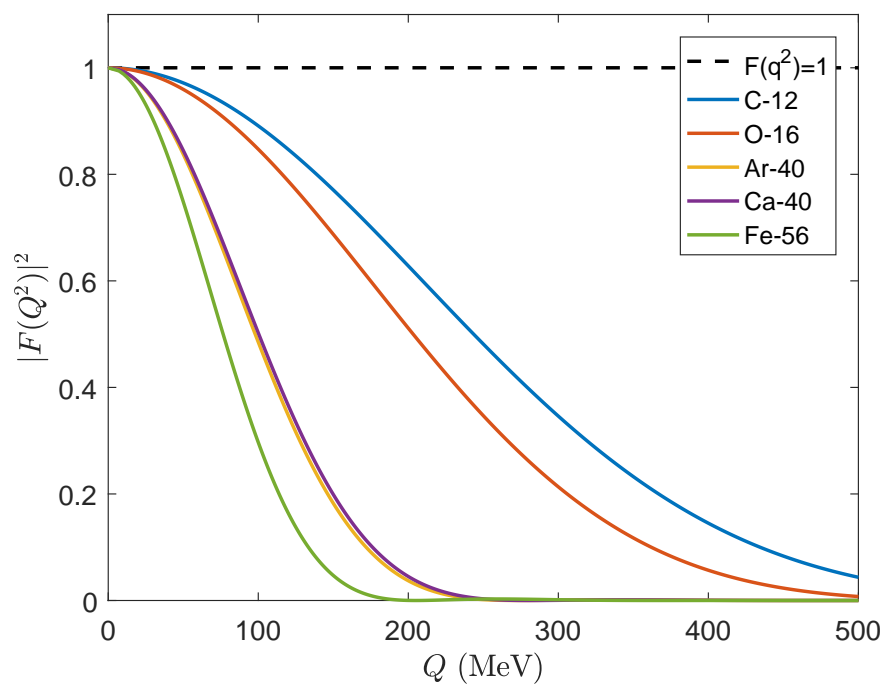


Figure 4.9: Comparison of the weak form factor of different nuclei as a function of the energy of the 4-momentum transfer.

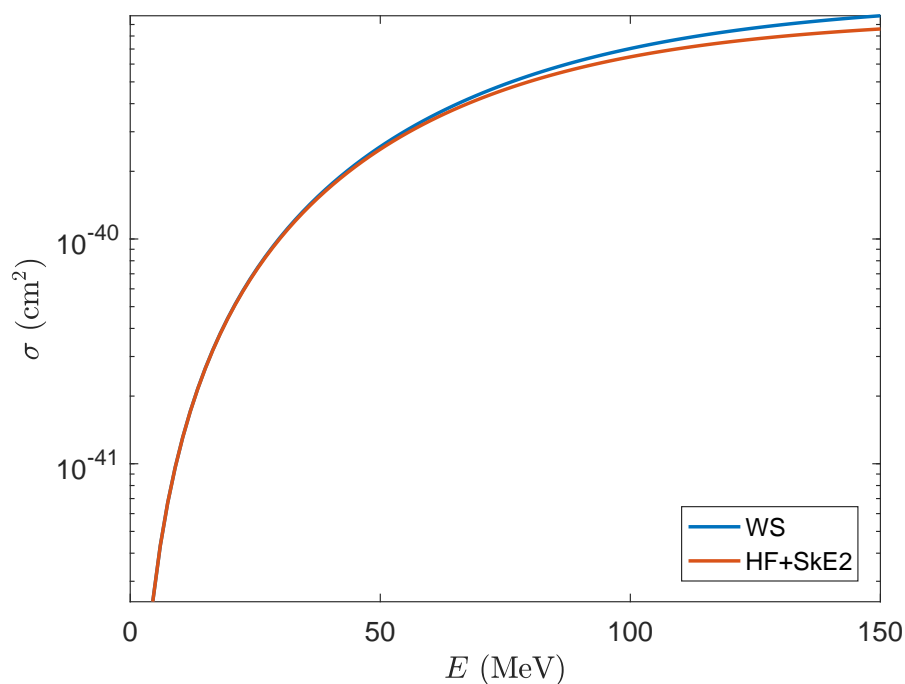


Figure 4.10: The cross section for a ^{12}C nucleus as a function of the energy of the incoming neutrino. The blue line is the Woods-Saxon cross section, while the red line is the SkE2 cross section. The form factor was calculated using a HF approach.

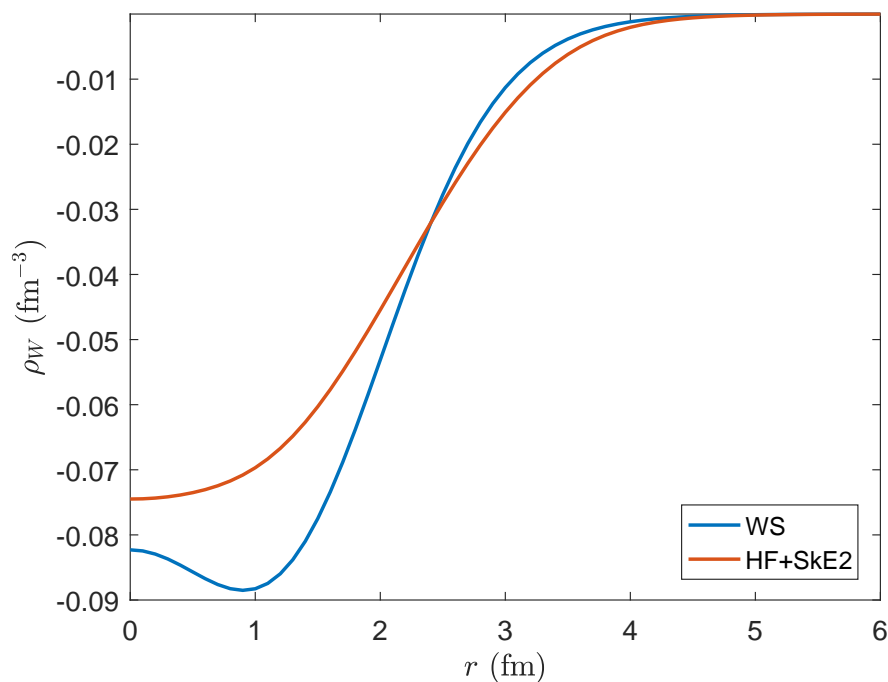


Figure 4.11: Weak charge density distribution for a ^{12}C nucleus as a function of the energy of the incoming neutrino. The blue line was calculated for the Woods-Saxon potential, while the red line was calculated for the SkE2 potential.

4.2.4 Woods-Saxon vs. Hartree-Fock + SkE2

In chapter 3, it was mentioned that the nucleus can be described through different approaches. Up till now, the nucleus has only been characterized through HF+SkE2. Fig. 4.10 shows a comparison of the cross section for ^{12}C , calculated using the Woods-Saxon approach with the one calculated using the HF+SkE2 approach. Corresponding weak charge density distributions are shown in Fig. 4.11.

The Woods-Saxon cross section is noticeably larger at higher energies. As seen in Fig. 4.11, the HF+SkE2 weak charge distribution is more diffuse, that is, the weak charge is more spread out. In turn, the HF+SkE2 cross section is smaller.

4.2.5 Influence of RPA effects

To get an estimate of what the results using the RPA wave functions will be, ground-state single particle occupation probabilities from the extended RPA, Eq. (3.39), using the Skyrme III (SkIII) force were used. The occupation numbers for ^{16}O are given in Tab. 4.2 [49].

The cross section for ^{16}O using occupation numbers is shown in Fig. 4.12. The respective weak charge density distributions are shown in Fig. 4.13. The obtained cross section does not appear to diverge largely from the HF+SkE2 cross section. Furthermore, the weak charge distributions are roughly identical in diffuseness.

As a result, the RPA wave functions are not expected to alter the cross section greatly. A verification using a consistent RPA is necessary to confirm this, i.e. one that uses the SkE2 force.

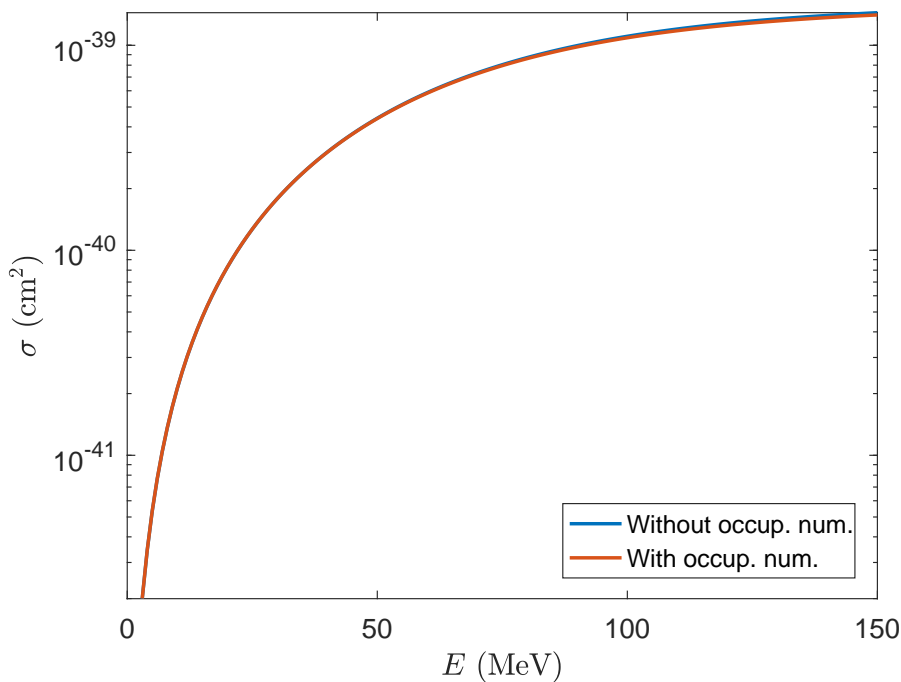


Figure 4.12: The cross section for a ^{16}O nucleus as a function of the energy of the incoming neutrino. The blue line was calculated without occupation numbers, while the red line was calculated with occupation numbers.

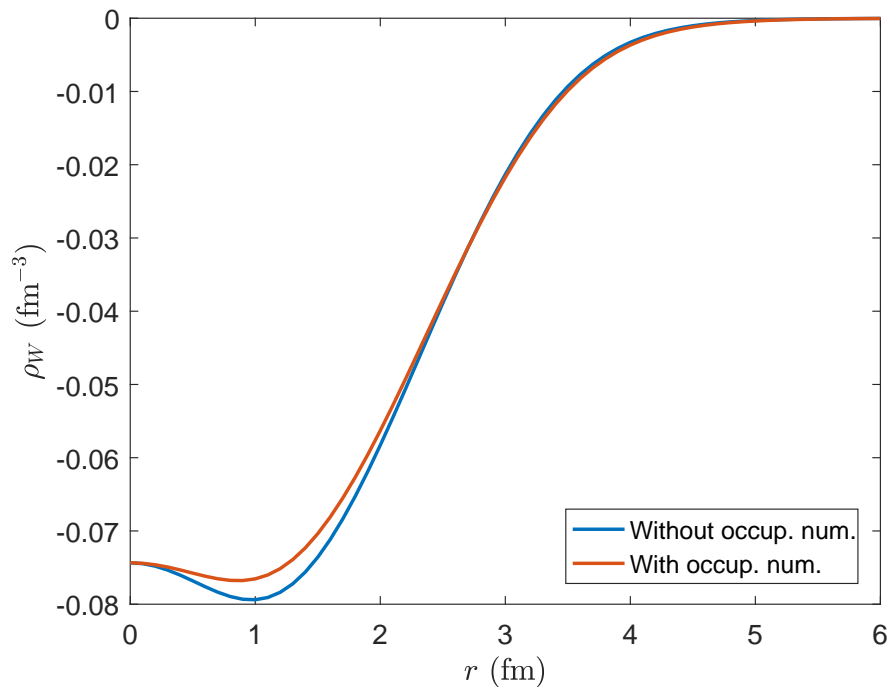


Figure 4.13: Weak charge density distribution comparison for a ^{16}O nucleus as a function the radial distance. The blue line was calculated without occupation numbers, while the red line was calculated with occupation numbers.

Table 4.2: Occupation probabilities $n_{\alpha\alpha}$ calculated through TDDM with SkIII. Values taken from [49].

Orbit	Proton	Neutron
$1s_{1/2}$	1	1
$1p_{3/2}$	0.894	0.893
$1p_{1/2}$	0.868	0.865
$1d_{5/2}$	0.108	0.109
$2s_{1/2}$	0.019	0.021

4.2.6 Comparison with literature

The results have been compared to the literature. Fig. 4.14 shows a comparison of the cross section for ^{12}C . The blue, continuous line shows the cross section from L. Alvarez Ruso (2016) [55]. Alongside this are the point-like (blue, dashed) and HF+SkE2 cross sections (blue, dotted). The cross section from literature displays a slight difference from the HF+SkE2 cross section. For this reason, the ratio (red, continuous) between the result of [55] and the HF+SkE2 cross section has been plotted. This line is more or less constant. Therefore, the difference is expected to originate from a constant factor in the form factor.

Fig. 4.15 shows a comparison of the cross section for ^{40}Ar . The yellow line shows the cross section from [56]. Alongside this are the point-like (blue) and HF+SkE2 cross sections (red). The cross sections match rather well. The result from [56] was produced by the SNOwGLoBES software from Duke University [57].

Lastly, Fig. 4.16 shows a comparison of the cross section for a number of different nuclei. The dashed lines show the cross sections from [58]. Alongside this are HF+SkE2 cross sections (continuous) and the point-like (dotted) cross section for ^{12}C . The cross sections from literature display a difference from the HF+SkE2 cross section. This is likely due to the fact that the form factors from [58] are derived using quasiparticle RPA (QRPA) calculations. The ground-state wave functions were obtained by iteratively solving the Bardeen-Cooper-Schrieffer (BCS) equations using a Coulomb-corrected Woods-Saxon potential as well as Bonn charge-dependent potential.

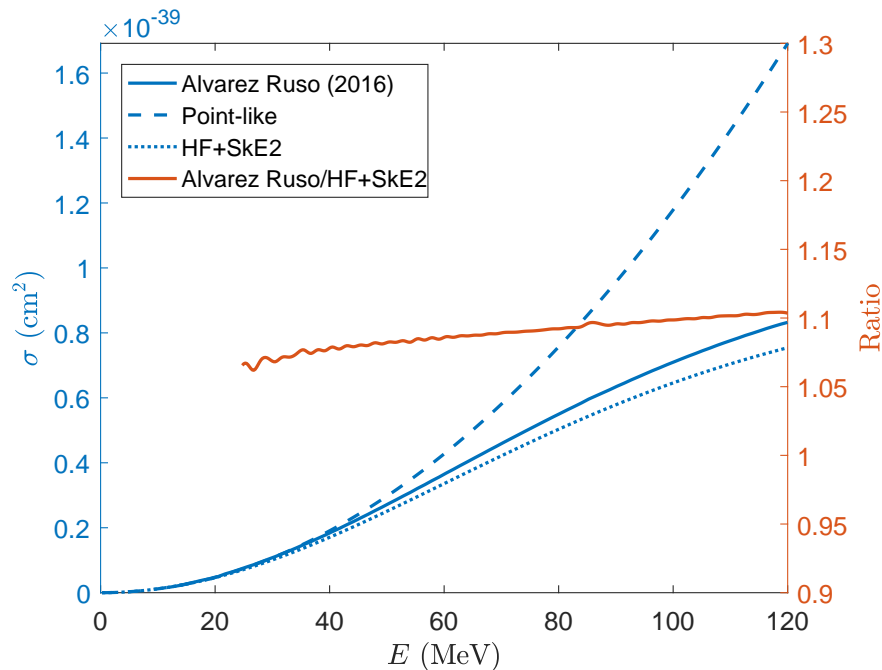


Figure 4.14: The cross section for a ^{12}C nucleus as a function of the energy of the incoming neutrino. The blue, continuous line is the cross section as calculated by L. Alvarez Ruso (2016) [55], the dashed line represents a point-like particle and the dotted line includes the form factor. The red line is the ratio between the cross section by [55] and the cross section with form factor.

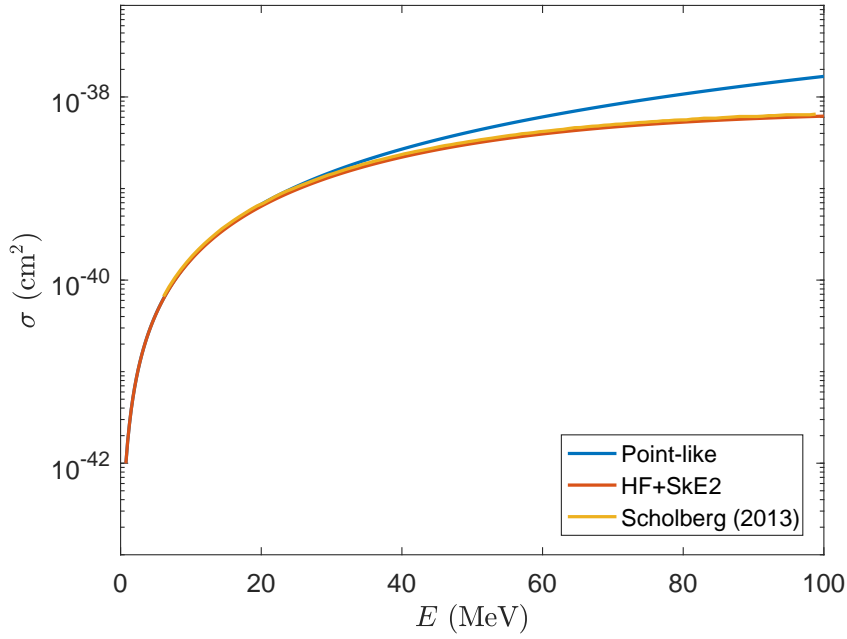


Figure 4.15: The cross section for a ^{40}Ar nucleus as a function of the energy of the incoming neutrino. The blue line represents a point-like particle, the red line uses the HF+SkE2 form factor and the yellow line is the cross section from K. Scholberg (2014) [56].

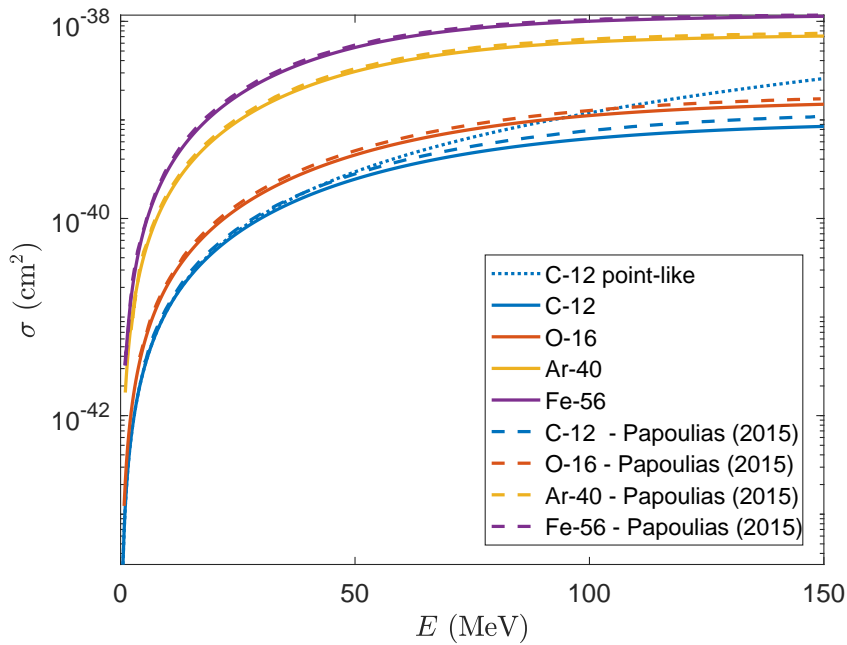


Figure 4.16: Comparison of the cross section of a number of nuclei as a function of the energy of the incoming neutrino with the results of D. K. Papoulias and T. S. Kosmas (2015) [58]. The blue, dotted line is the ^{12}C point-like cross section. The continuous lines are cross sections calculated in a HF+SkE2 approach, while the dashed lines denote the cross sections from [58].

4.3 Comparison to other interactions

CE ν NS can be compared to the reaction channels discussed in section 2.5. Figures 4.17, 4.18, 4.19 and 4.20 show the CE ν NS (blue) cross section compared to the ν NCQE (red), $\bar{\nu}$ NCQE (yellow), ν CCQE (purple) and $\bar{\nu}$ CCQE (green) cross sections for ^{12}C , ^{16}O , ^{40}Ar and ^{40}Ca .

The dominance of CE ν NS at low energies is clearly visible. Its cross section is about an order of magnitude larger than both the NCQE and CCQE cross section at 40 MeV for all nuclei. It remains larger until around 90 MeV for ^{12}C , 100 MeV for ^{16}O , 110 MeV for ^{40}Ar and 120 MeV for ^{40}Ca . As the energy increases, CCQE scattering becomes larger until it finally overtakes CE ν NS. The same is true for the NCQE cross section, but at higher energies. In all cases CCQE is the first reaction channel to overtake CE ν NS. The point of intersection depends on the model of the nucleus. It also lies at a different energy for the RPA than for HF.

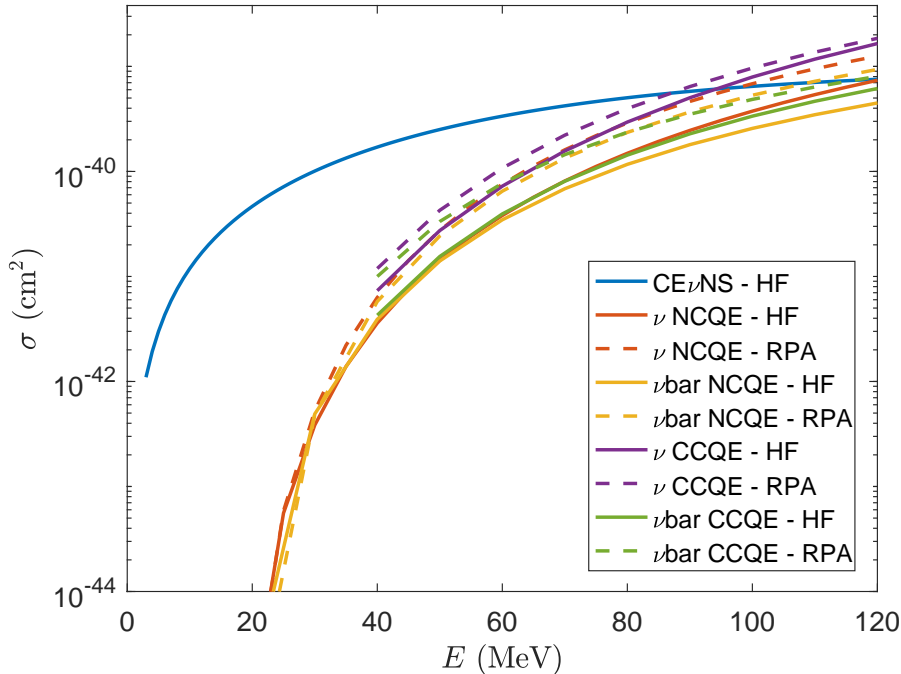


Figure 4.17: Comparison of the cross section for ^{12}C as a function of the energy of the incoming neutrino with other reaction channels. The CE ν NS cross section was calculated in the HF+SkE2 approach, the CCQE and NCQE cross sections for neutrinos and antineutrinos in both the HF+SkE2 and RPA+SkE2 frameworks.

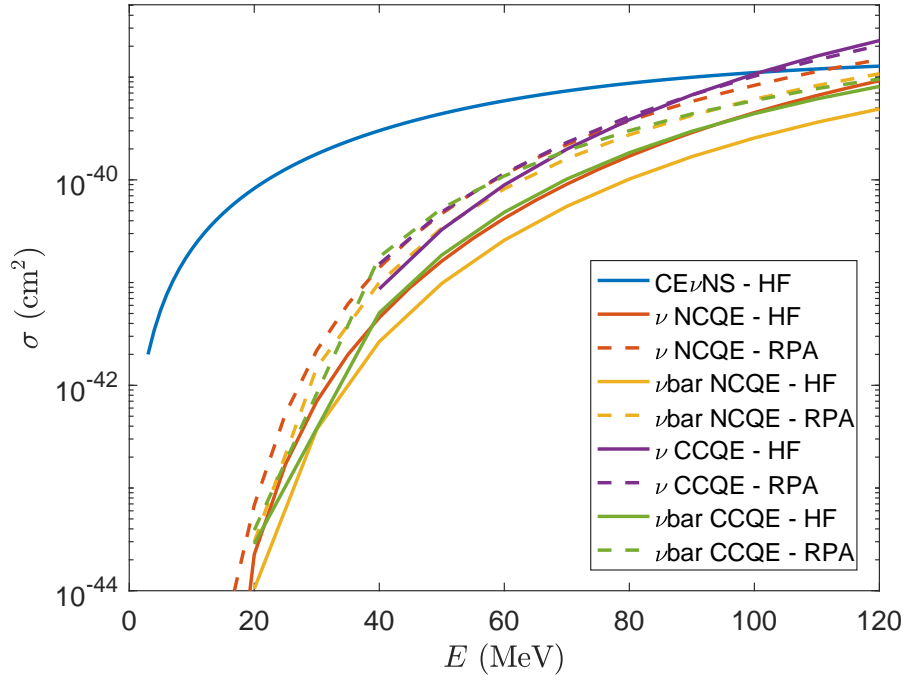


Figure 4.18: Comparison of the cross section for ^{16}O as a function of the energy of the incoming neutrino with other reaction channels. The cross sections were calculated using the same models as in Fig. 4.17.

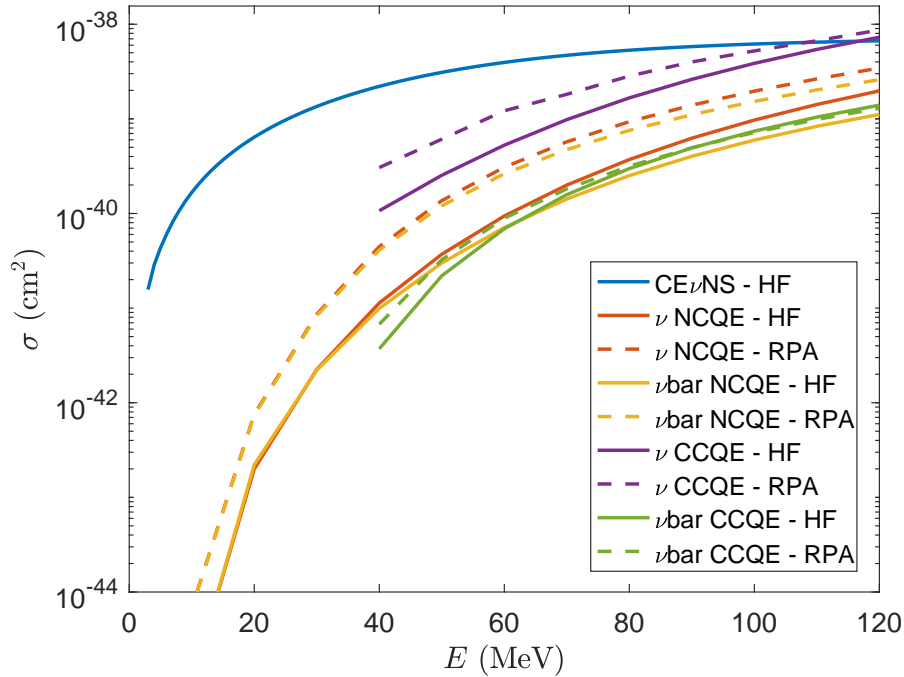


Figure 4.19: Comparison of the cross section for ^{40}Ar as a function of the energy of the incoming neutrino with other reaction channels. The cross sections were calculated using the same models as in Fig. 4.17.

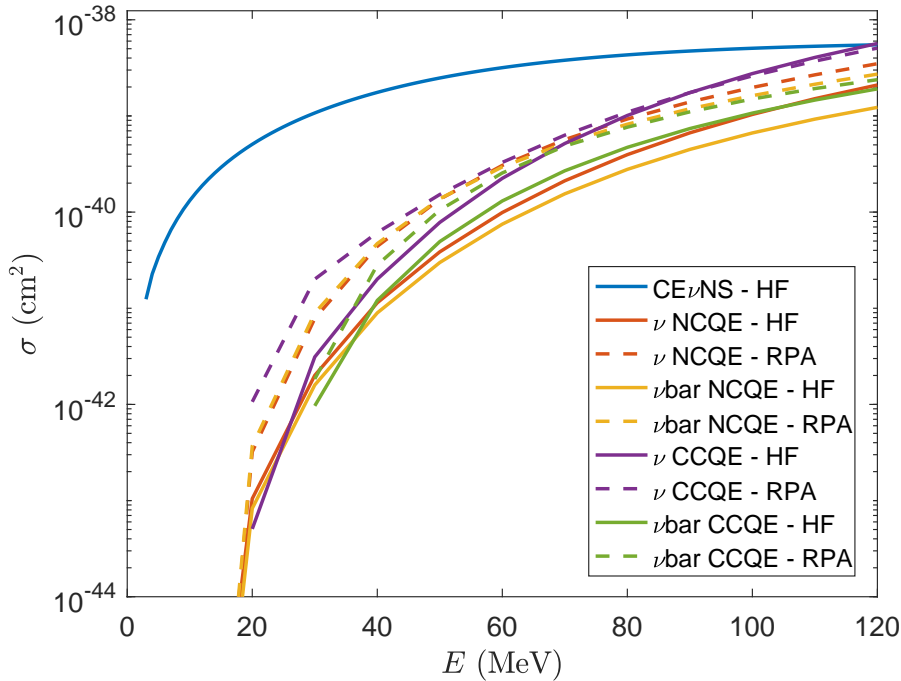


Figure 4.20: Comparison of the cross section for ^{40}Ca as a function of the energy of the incoming neutrino with other reaction channels. The cross sections were calculated using the same models as in Fig. 4.17.

4.4 Sensitivity to the weak mixing angle

In section 1.4 it was mentioned that $\text{CE}\nu\text{NS}$ could be used to test certain parameters in the Standard Model, in particular the weak mixing angle θ_W . The theoretical value of the weak mixing angle depends on the scheme in which it is calculated. In general, the value of $\sin^2 \theta_W$ is stated. CODATA [1] gives the value 0.2223(21) determined from

$$\sin^2 \theta_W = 1 - \left(\frac{M_W}{M_Z} \right)^2. \quad (4.3)$$

The Particle Data Group (PDG) [59] gives the value 0.23129(5) determined through the modified minimal subtraction ($\overline{\text{MS}}$) scheme.

Figures 4.21 and 4.22 show the cross section in a HF+SkeE2 approach for different values of $\sin^2 \theta_W$ for ^{12}C and ^{56}Fe . The values plotted are from CODATA, from PDG and 0.25. The reason for the latter is that for this value the effect of the protons vanishes and only that of the neutrons remains. Also the cross section for the CODATA value with standard uncertainty above and below has been plotted.

Figures 4.23 and 4.24 show the ratio of different values to the CODATA value. Including the standard uncertainty gives a 1.5 – 2% difference. The difference between the CODATA and PDG values is about 7 – 8%. The difference with $\sin^2 \theta_W = 0.25$ is around 22 – 27%.

Differences such as these will likely be within experimental error margins and, therefore, not be distinguishable. However, the effect can possibly be maximized if one, for

instance, studies cross section asymmetries for different nuclei with equal neutron numbers. This way, the effect of the neutrons is minimized and, hence, $\sin^2 \theta_W$ sensitivity enhanced.

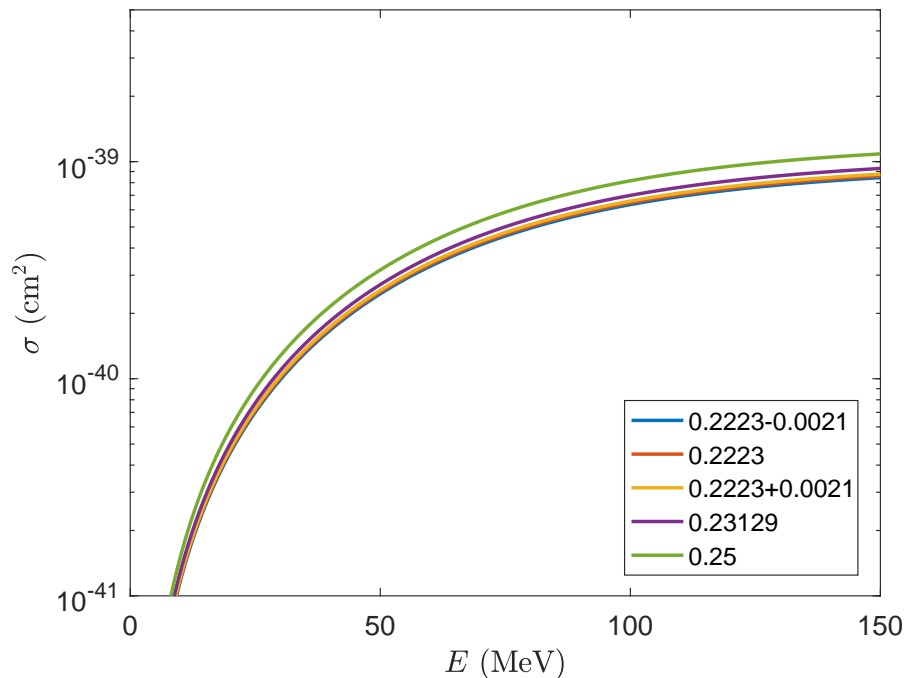


Figure 4.21: Cross section for ^{12}C in a HF+SkE2 approach for different values of $\sin^2 \theta_W$.

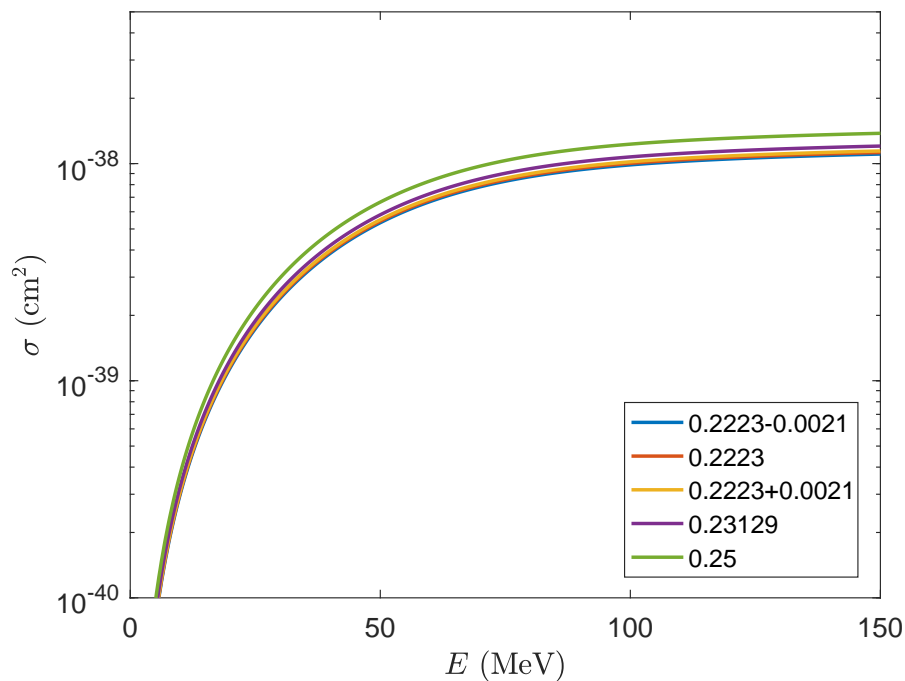


Figure 4.22: Cross section for ^{56}Fe in a HF+SkE2 approach for different values of $\sin^2 \theta_W$.

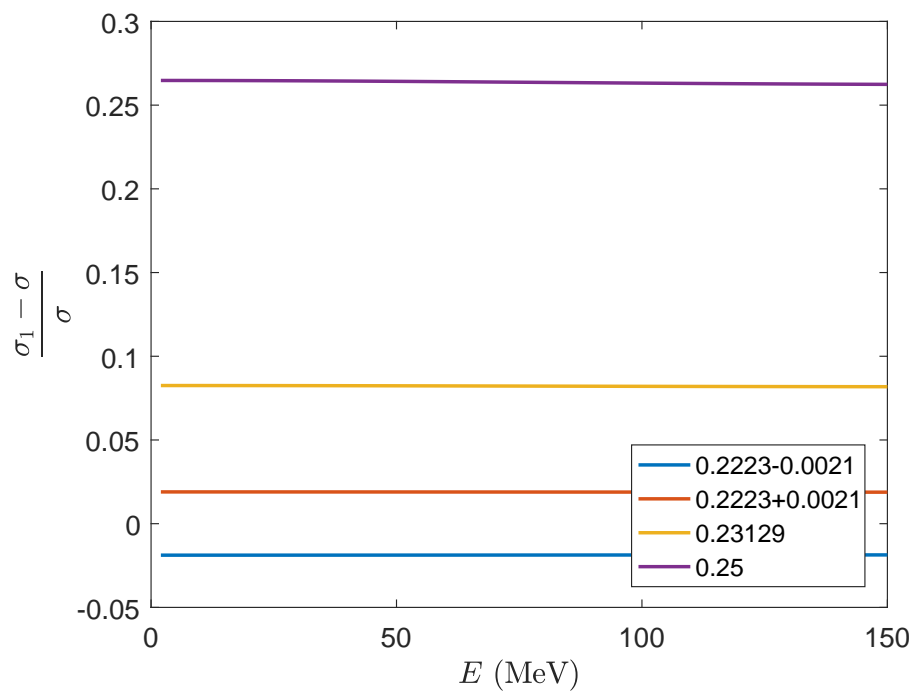


Figure 4.23: Ratio of cross sections for ^{12}C in a HF+SkE2 approach for different values of $\sin^2 \theta_W$ to the CODATA value.

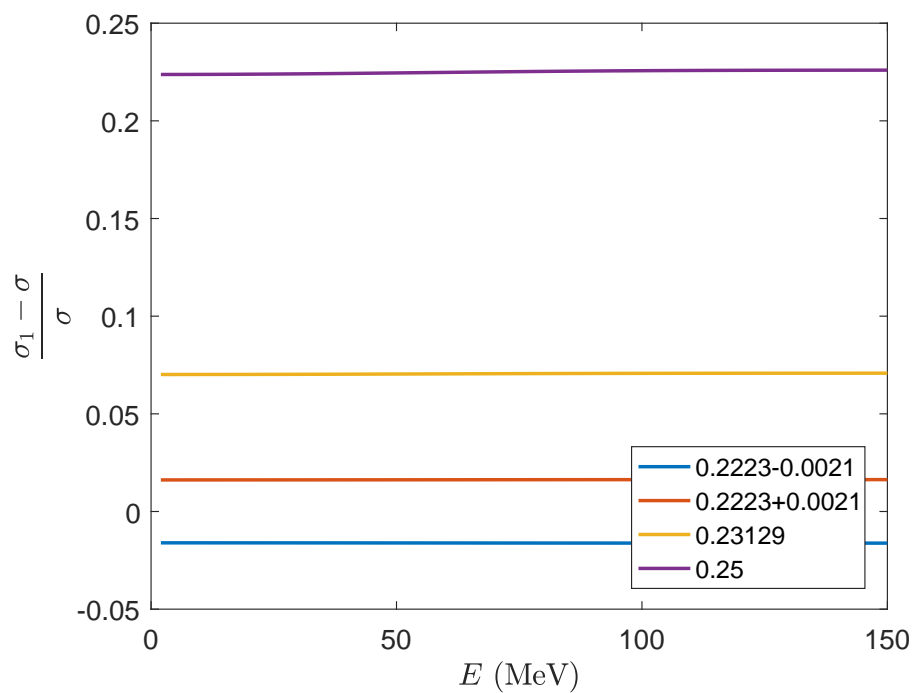


Figure 4.24: Ratio of cross sections for ^{56}Fe in a HF+SkE2 approach for different values of $\sin^2 \theta_W$ to the CODATA value.

5 | Conclusion and future prospects

A good understanding of neutrino-nucleus interactions is necessary in order to both accurately reproduce neutrino effects in astrophysical models and study neutrino properties. Neutrino-nucleus interactions play a big role in the neutrino heating mechanism of core-collapse supernovae. Furthermore, the large $\text{CE}\nu\text{NS}$ cross section could pave the way for a new generation of neutrino detectors.

In this thesis, the maximum recoil energy T_{max} was calculated for different nuclei. It was shown that T_{max} increases as the energy of the incoming neutrino increases. In addition, lighter nuclei gave a larger maximum recoil energy.

The cross section was calculated for different nuclei. Results showed that the cross section is larger for heavier nuclei. Moreover, in the case of isobaric nuclei, the nucleus with the largest neutron number had the largest cross section. The latter was attributed to the fact that the neutron has a larger absolute weak charge than the proton.

Comparison of the Woods-Saxon with the Hartree-Fock + Skyrme interaction model for the description of the nucleus yielded a larger cross section for the HF+SkE2 approach, in the case of a ^{12}C nucleus. The weak charge distribution of the Woods-Saxon approach was less diffuse. Therefore, the size of the nucleus is smaller in this description. Comparison of the Hartree-Fock + Skyrme interaction model with one altered through the use of RPA occupation numbers on the nucleon orbitals gave no substantial difference. In turn, the weak charge distribution showed no substantial difference in diffuseness.

In general, the results displayed a rather good correspondence to those found in literature. The cross sections from literature employed different models for the nucleus. This brought about a slight deviation from the calculated value.

The $\text{CE}\nu\text{NS}$ cross section was compared to the neutral current quasielastic and charged current quasielastic cross sections. The $\text{CE}\nu\text{NS}$ cross section was larger for energies up to around 60 MeV. This showed its dominance at low energies and demonstrates its importance in physical models with neutrinos at low energy.

Lastly, the sensitivity of the $\text{CE}\nu\text{NS}$ cross section to the weak mixing angle was demonstrated. The cross sections calculated for different values of the weak mixing angle did not display any significant difference. As such, cross section asymmetries for different nuclei with equal neutron numbers may be used to enhance the sensitivity.

An appealing extension to this work is the calculation of the cross section using a consistent RPA approach. Many neutrino-nucleus cross sections stated in literature [44, 46, 60, 61] make use of the RPA. This is thanks to its success in describing collective excitations of nuclei, particularly in the prediction of giant resonances in nuclei with more than 10 nucleons [62]. A comparison of $\text{CE}\nu\text{NS}$ in this model with other reaction channels would be a consistent way to examine the contrast.

Besides varying the nuclear model, it may be possible to account for additional effects in the form factor. Strangeness content of the nucleon has been shown to influence neutral current neutrino-nucleus cross sections [63]. Further research can be performed in order to investigate the effect in the case of $CE\nu NS$.

Application of the models described in this work to astrophysical models is another objective. As mentioned in section 1.3, neutrino-nucleus interactions are expected to be important for energy transport to stellar material above the PNS and reviving the shock. $CE\nu NS$ has the largest cross section at neutrino energies involved in core-collapse supernovae. Including this interaction is, therefore, recommended.

Finally, the ultimate goal is to verify the theoretically obtained results with experiments.

A | Evaluation of $|\mathcal{M}|^2$

In this chapter, $|\mathcal{M}|^2$ will be evaluated, starting from expression (2.32),

$$i\mathcal{M}_{rr'} = -\frac{G_F}{\sqrt{2}}Q_W F(q^2)g_L^\nu \bar{u}^{r'}(p_1)\gamma^\mu(1-\gamma^5)u^r(k_1)(k_2+p_2)_\mu. \quad (\text{A.1})$$

Multiplying by its complex conjugate and summing over the spin states gives

$$\begin{aligned} \sum_{rr'} |i\mathcal{M}_{rr'}|^2 &= \sum_{rr'} \frac{G_F^2}{2} Q_W^2 |F(q^2)|^2 (g_L^\nu)^2 (k_2+p_2)_\mu (k_2+p_2)_\nu \\ &\quad \times \bar{u}^{r'}(k_1)\gamma^\mu(1-\gamma^5)u^r(p_1)\bar{u}^r(p_1)\gamma^\nu(1-\gamma^5)u^{r'}(k_1). \end{aligned} \quad (\text{A.2})$$

Writing spinor indices makes it so that we can move all the factors around and use the completeness relations

$$\sum_r u^r(p)\bar{u}^r(p) = \not{p} + m, \quad \sum_r v^r(p)\bar{v}^r(p) = \not{p} - m. \quad (\text{A.3})$$

The neutrino part, writing spinor indices so that they can be moved around, can then be written as

$$\begin{aligned} \sum_{rr'} \bar{u}_a^{r'}(k_1)\gamma^\mu_{ak}(1-\gamma^5)_{kb}u_b^r(p_1)\bar{u}_c^r(p_1)\gamma^\nu_{cl}(1-\gamma^5)_{ld}u_d^{r'}(k_1) \\ = (k_1 + m)_{da}\gamma^\mu_{ak}(1-\gamma^5)_{kb}(\not{p}_1 + m)_{bc}\gamma^\nu_{cl}(1-\gamma^5)_{ld} \\ = \text{tr}[\not{k}_1\gamma^\mu(1-\gamma^5)\not{p}_1\gamma^\nu(1-\gamma^5)] + \text{tr}[m^2\gamma^\mu(1-\gamma^5)\gamma^\nu(1-\gamma^5)] \\ = 2\text{tr}[\not{k}_1\gamma^\mu\not{p}_1\gamma^\nu(1-\gamma^5)] \\ = 8(k_1^\mu p_1^\nu + k_1^\nu p_1^\mu - g^{\mu\nu}k_1 \cdot p_1 - i\epsilon^{\rho\mu\sigma\nu}k_{1\rho}p_{1\sigma}). \end{aligned} \quad (\text{A.4})$$

The expression becomes

$$\begin{aligned} |\mathcal{M}|^2 &= 4G_F^2 Q_W^2 |F(q^2)|^2 (g_L^\nu)^2 [2k_1 \cdot (k_2+p_2) p_1 \cdot (k_2+p_2) \\ &\quad - (k_2+p_2)^2 k_1 \cdot p_1 - i\epsilon^{\mu\nu\rho\sigma}k_{1\mu}(k_2+p_2)_\nu p_{1\rho}(k_2+p_2)_\sigma]. \end{aligned} \quad (\text{A.5})$$

Note that in the last term inside the brackets, the Levi-Civita symbol is contracted with a tensor that is symmetric in the indices ν and σ . Since contraction of an antisymmetric tensor with a symmetric tensor yields zero, the last term in brackets becomes zero. Rewriting the previous expression gives

$$\begin{aligned} |\mathcal{M}|^2 &= 8G_F^2 Q_W^2 |F(q^2)|^2 (g_L^\nu)^2 [k_1 \cdot k_2 p_1 \cdot k_2 + k_1 \cdot k_2 p_1 \cdot p_2 \\ &\quad + k_1 \cdot p_2 p_1 \cdot k_2 + k_1 \cdot p_2 p_1 \cdot p_2 - (M^2 + k_2 \cdot p_2) k_1 \cdot p_1]. \end{aligned} \quad (\text{A.6})$$

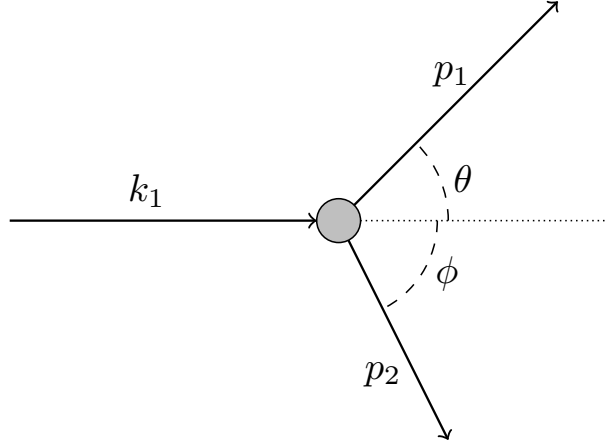


Figure A.1: Collision diagram of 2 particle \rightarrow 2 particle scattering in the lab frame.

In the lab frame (figure A.1), the 4-momenta are given by

$$k_1 = (E, \mathbf{k}_1), \quad k_2 = (M, \mathbf{0}), \quad p_1 = (E - T, \mathbf{p}_1), \quad p_2 = (T + M, \mathbf{p}_2) \quad (\text{A.7})$$

and

$$q = k_1 - p_1 = k_2 - p_2 = (T, \mathbf{q}). \quad (\text{A.8})$$

By doing some simple algebra, one can work out the following dot products:

$$k_1 \cdot k_2 = EM \quad (\text{A.9})$$

$$p_1 \cdot p_2 = \frac{1}{2}((p_1 + p_2)^2 - p_1^2 - p_2^2) = \frac{1}{2}((k_1 + k_2)^2 - M^2) = EM \quad (\text{A.10})$$

$$k_2 \cdot p_1 = M(E - T) \quad (\text{A.11})$$

$$k_2 \cdot p_2 = M(T + M) \quad (\text{A.12})$$

$$k_1 \cdot p_1 = (p_1 + p_2 - k_2) \cdot p_1 = MT \quad (\text{A.13})$$

$$k_1 \cdot p_2 = k_1 \cdot (k_1 + k_2 - p_1) = M(E - T) \quad (\text{A.14})$$

$$q^2 = (k_1 - p_1)^2 = -2MT \quad (\text{A.15})$$

Using these, the amplitude $|\mathcal{M}|^2$ results in

$$|\mathcal{M}|^2 = 32G_F^2 Q_W^2 |F(q^2)|^2 (g_L^\nu)^2 E^2 M^2 \left(1 - \frac{T}{E} - \frac{MT}{2E^2}\right). \quad (\text{A.16})$$

B | Derivation of $\frac{d\sigma}{dq^2}$

In this chapter, the origin of equation (2.34) will briefly be explained.

Fermi's golden rule for cross sections is [64]

$$d\sigma = \frac{|\mathcal{M}|^2}{2E_a 2E_b |v_a - v_b|} (2\pi)^4 \delta(p_a + p_b - \sum_f p_f) \prod_f \frac{d^3 p_f}{(2\pi)^3 2E_f}, \quad (\text{B.1})$$

where the spatial parts of p_a and p_b , i.e. \mathbf{p}_a and \mathbf{p}_b , are chosen to lie along the z -axis. For two particles in the final state, this becomes

$$d\sigma = \frac{|\mathcal{M}|^2}{2E_a 2E_b |v_a - v_b|} (2\pi)^4 \delta(p_a + p_b - p_1 - p_2) \frac{d^3 p_1}{(2\pi)^3 2E_1} \frac{d^3 p_2}{(2\pi)^3 2E_2}. \quad (\text{B.2})$$

When it is evaluated in the center-of-mass frame, $\mathbf{p}_a = -\mathbf{p}_b$ and $\mathbf{p}_1 = -\mathbf{p}_2$, so that

$$d\sigma = \frac{|\mathcal{M}|^2}{16(2\pi)^2 (E_a + E_b)^2} \frac{|\mathbf{p}_1|}{|\mathbf{p}_a|} d\Omega_{\text{CM}} \quad (\text{B.3})$$

where the following relation was used:

$$\begin{aligned} 2E_a 2E_b |v_a - v_b| &= 4E_a E_b \left| \frac{p_a^z}{E_a} - \frac{p_b^z}{E_b} \right| \\ &= 4E_a E_b \left| \frac{\mathbf{p}_a}{E_a} - \frac{\mathbf{p}_b}{E_b} \right| \\ &= 4|\mathbf{p}_a| (E_a + E_b). \end{aligned} \quad (\text{B.4})$$

In order to write the cross section in a form that is Lorentz invariant, $d\Omega_{\text{CM}}$ can be written in terms of the variable dq^2 , which gives

$$d\Omega_{\text{CM}} = d\phi d(\cos \theta_{\text{CM}}) = -\frac{d\phi dq^2}{2|\mathbf{p}_a||\mathbf{p}_1|}. \quad (\text{B.5})$$

The resulting equation is

$$\frac{d\sigma}{dq^2} = -\frac{|\mathcal{M}|^2}{64\pi (E_a + E_b)^2 |\mathbf{p}_a|^2}. \quad (\text{B.6})$$

Writing $|\mathbf{p}_a|$ in the form

$$|\mathbf{p}_a|^2 = \frac{1}{4(E_a + E_b)^2} ((E_a + E_b)^2 - (m_1 + m_2)^2)((E_a + E_b)^2 - (m_1 - m_2)^2) \quad (\text{B.7})$$

and using eqs. A.7, as well as specifying the mass of the particles $m_1 = 0$ and $m_2 = M$, yields

$$(E_a + E_b)^2 |\mathbf{p}_a|^2 = E^2 M^2. \quad (\text{B.8})$$

The final result is equation 2.34.

C | Second quantization formalism

C.1 Many-body states

The Fock space \mathcal{F} is the direct sum of Hilbert spaces \mathcal{H}_i with fixed particle number i : [65]

$$\mathcal{F} \equiv \mathcal{H}_0 \oplus \mathcal{H}_1 \oplus \dots \oplus \mathcal{H}_n \oplus \dots \quad (\text{C.1})$$

Herein, \mathcal{H}_0 is the Hilbert space which has basis $\mathcal{B} = \{|0\rangle\}$, where $|0\rangle$ is the vacuum state, and \mathcal{H}_1 is the Hilbert space with basis $\mathcal{B} = \{|\mu\rangle\}$. This way, an n -particle state is given by the direct product of the single particle state $|i : \mu\rangle$ of each particle i :

$$|1 : \alpha; 2 : \beta; \dots\rangle \equiv |1 : \alpha\rangle \otimes |2 : \beta\rangle \otimes \dots \quad (\text{C.2})$$

In the case of bosons or fermions, \mathcal{H}_n can be reduced to the subspace of totally symmetric or totally antisymmetric states, respectively. Since bosons do not appear in the description of the nucleus, further discussion will be limited to the case of fermions [65].

A normalized and totally antisymmetric state is constructed through [65]

$$|\Phi\rangle \equiv |\alpha\beta\dots\rangle \equiv \frac{1}{\sqrt{n!}} \begin{vmatrix} |1 : \phi_\alpha\rangle & |1 : \phi_\beta\rangle & \dots & |1 : \phi_\mu\rangle & \dots \\ |2 : \phi_\alpha\rangle & |2 : \phi_\beta\rangle & \dots & |2 : \phi_\mu\rangle & \dots \\ \vdots & \vdots & \ddots & \vdots & \vdots \\ |n : \phi_\alpha\rangle & |n : \phi_\beta\rangle & \dots & |n : \phi_\mu\rangle & \dots \\ \vdots & \vdots & & \vdots & \ddots \end{vmatrix} \quad (\text{C.3})$$

where as opposed to a regular determinant, the elements have to be multiplied through the direct product. Note that,

$$|\alpha\beta\dots\mu\nu\dots\rangle = -|\alpha\beta\dots\nu\mu\dots\rangle. \quad (\text{C.4})$$

It is convenient to define the creation and annihilation operators a_μ^+ and a_μ on \mathcal{F} . These operators have the following properties [65]:

- a_μ^+ creates a particle in the state μ , so that $\mathcal{H}_n \rightarrow \mathcal{H}_{n+1}$:

$$\begin{cases} \text{if } \mu \text{ is not occupied} & a_\mu^+ |\alpha\beta\dots\rangle = |\mu\alpha\beta\dots\rangle \\ \text{if } \mu \text{ is occupied} & a_\mu^+ |\alpha\beta\dots\mu\dots\rangle = 0 \end{cases} \quad (\text{C.5})$$

- a_μ annihilates a particle in the state μ , so that $\mathcal{H}_n \rightarrow \mathcal{H}_{n-1}$:

$$\begin{cases} \text{if } \mu \text{ is not occupied} & a_\mu |\alpha\beta\dots\rangle = 0 \\ \text{if } \mu \text{ is occupied} & a_\mu |\mu\alpha\beta\dots\rangle = |\alpha\beta\dots\rangle \end{cases} \quad (\text{C.6})$$

- a_μ^+ is the Hermitian conjugate of a_μ :

$$a_\mu^+ = (a_\mu)^\dagger \quad (\text{C.7})$$

- the anticommutation relations:

$$\{a_\mu^+, a_\nu^+\} = 0, \quad \{a_\mu, a_\nu\} = 0, \quad \{a_\mu, a_\nu^+\} = \delta_{\mu\nu}. \quad (\text{C.8})$$

With this definition, a single particle basis can also be written as $\mathcal{B} = \{a_\mu, a_\mu^+\}$ [65]. Additionally, a many-body state can be constructed from the particle vacuum using creation operators: [65]

$$|\alpha\beta\dots\rangle = a_\alpha^+ a_\beta^+ \dots |0\rangle. \quad (\text{C.9})$$

A change of basis from $\mathcal{B} = \{a_\mu, a_\mu^+\}$ to $\mathcal{B}' = \{b_\xi, b_\xi^+\}$ can be achieved through [65]

$$|\mu\rangle = \sum_\xi |\xi\rangle C_{\xi\mu}, \quad \langle\mu| = \sum_\xi \langle\xi| C_{\xi\mu}^*, \quad (\text{C.10})$$

or in terms of creation and annihilation operators:

$$a_\mu^+ = \sum_\xi b_\xi^+ C_{\xi\mu}, \quad a_\mu = \sum_\xi b_\xi C_{\xi\mu}^*, \quad (\text{C.11})$$

with $C_{\xi\mu} = \langle\xi|\mu\rangle$ [65].

C.2 Operators

Operators defined in first quantization on their respective Hilbert space \mathcal{H}_N ,

$$F = \sum_{i=1}^N f(i) \quad (\text{C.12})$$

$$G = \sum_{i<j}^N g(i, j), \quad (\text{C.13})$$

can be rewritten in their second quantized form through

$$F = \sum_{\alpha\beta} f_{\alpha\beta} a_\alpha^+ a_\beta \quad (\text{C.14})$$

$$G = \sum_{\alpha\beta\gamma\delta} g_{\alpha\beta\delta\gamma} a_\alpha^+ a_\beta^+ a_\gamma a_\delta \quad (\text{C.15})$$

with $f_{\alpha\beta} = \langle 1 : \alpha | f | 1 : \beta \rangle$ and $g_{\alpha\beta\delta\gamma} = \langle 1 : \alpha; 2 : \beta | f | 1 : \delta; 2 : \gamma \rangle$. The sums in the second quantized expressions do not run over physical particles, but rather over the single particle basis states [65].

Bibliography

- [1] P. J. Mohr, D. B. Newell, and B. N. Taylor, “CODATA Recommended Values of the Fundamental Physical Constants: 2014,” *Rev. Mod. Phys.* **88** no. 3, (2016) 035009, [arXiv:1507.07956](https://arxiv.org/abs/1507.07956) [physics.atom-ph].
- [2] **COHERENT** Collaboration, D. Akimov *et al.*, “The COHERENT Experiment at the Spallation Neutron Source,” [arXiv:1509.08702](https://arxiv.org/abs/1509.08702) [physics.ins-det].
- [3] K. Scholberg, “Coherent elastic neutrino-nucleus scattering,” *Journal of Physics: Conference Series* **606** no. 1, (2015) 012010. <http://stacks.iop.org/1742-6596/606/i=1/a=012010>.
- [4] A. Drukier and L. Stodolsky, “Principles and applications of a neutral-current detector for neutrino physics and astronomy,” *Phys. Rev. D* **30** (Dec, 1984) 2295–2309.
- [5] B. Zeitnitz, “KARMEN: neutrino physics at ISIS,” *Progress in Particle and Nuclear Physics* **32** (1994) 351 – 373.
- [6] C. Athanassopoulos *et al.*, “The liquid scintillator neutrino detector and LAMPF neutrino source,” *Nuclear Instruments and Methods in Physics Research Section A: Accelerators, Spectrometers, Detectors and Associated Equipment* **388** no. 1, (1997) 149 – 172.
- [7] I. R. Barabanov, G. Ya. Novikova, V. V. Sinev, and E. A. Yanovich, “Research of the natural neutrino fluxes by use of large volume scintillation detector at Baksan,” [arXiv:0908.1466](https://arxiv.org/abs/0908.1466) [hep-ph].
- [8] J. N. Bahcall, A. M. Serenelli, and S. Basu, “New solar opacities, abundances, helioseismology, and neutrino fluxes,” *Astrophys. J.* **621** (2005) L85–L88, [arXiv:astro-ph/0412440](https://arxiv.org/abs/astro-ph/0412440) [astro-ph].
- [9] C. Spiering, “Towards high-energy neutrino astronomy. A historical review,” *European Physical Journal H* **37** (Aug., 2012) 515–565, [arXiv:1207.4952](https://arxiv.org/abs/1207.4952) [astro-ph.IM].
- [10] J. Barranco, O. Miranda, and T. Rashba, “Probing new physics with coherent neutrino scattering off nuclei,” *JHEP* **12** (2005) 021, [arXiv:hep-ph/0508299](https://arxiv.org/abs/hep-ph/0508299) [hep-ph].

- [11] D. Freedman, D. Schramm, and D. Tubbs, “The Weak Neutral Current and its Effects in Stellar Collapse,” *Annual Review of Nuclear Science* **27** no. 1, (1977) 167–207.
- [12] D. McKinsey and J. Doyle, “Liquid Helium and Liquid Neon-Sensitive, Low Background Scintillation Media for the Detection of Low Energy Neutrinos,” *Journal of Low Temperature Physics* **118** no. 3, (2000) 153 – 165.
- [13] C.J. Horowitz, K.J. Coakley, and D.N. McKinsey, “Supernova observation via neutrino-nucleus elastic scattering in the CLEAN detector,” *Phys. Rev. D* **68** (July, 2003) 023005.
- [14] C. Hagmann and A. Bernstein, “Two-phase emission detector for measuring coherent neutrino-nucleus scattering,” *IEEE Trans. Nucl. Sci.* **51** (2004) 2151–2155, [arXiv:nuc1-ex/0411004](https://arxiv.org/abs/nuc1-ex/0411004) [nuc1-ex].
- [15] L. Oberauer, “Coherent neutrino nucleus scattering,” *Progress in Particle and Nuclear Physics* **48** no. 1, (2002) 301 – 304.
- [16] K. Scholberg, “Prospects for measuring coherent neutrino-nucleus elastic scattering at a stopped-pion neutrino source,” *Phys. Rev.* **D73** (2006) 033005, [arXiv:hep-ex/0511042](https://arxiv.org/abs/hep-ex/0511042) [hep-ex].
- [17] **COHERENT** Collaboration, D. Akimov *et al.*, “COHERENT Experiment: current status,” *Journal of Physics: Conference Series* **798** no. 1, (2017) 012213. <http://stacks.iop.org/1742-6596/798/i=1/a=012213>.
- [18] J. Newby, “The COHERENT Experiment: Overview and Update of Results.” 2016 Fall Meeting of the APS Division of Nuclear Physics, Vancouver, B.C., *slides*, 2016.
- [19] J. Zettlemoyer, “Detector Technologies for the COHERENT Experiment.” 2017 APS April Meeting, Washington, D.C., Indiana University, *slides*, 2017.
- [20] S. J. Brice *et al.*, “A method for measuring coherent elastic neutrino-nucleus scattering at a far off-axis high-energy neutrino beam target,” *Phys. Rev.* **D89** no. 7, (2014) 072004, [arXiv:1311.5958](https://arxiv.org/abs/1311.5958) [physics.ins-det].
- [21] **CoGeNT** Collaboration, J. Collar, “Coherent neutrino detection in the year 2008,” *Journal of Physics: Conference Series* **136** no. 2, (2008) 022009. <http://stacks.iop.org/1742-6596/136/i=2/a=022009>.
- [22] B. Cabrera-Palmer and D. Reyna, *Development of coherent germanium neutrino technology (CoGeNT) for reactor safeguards*. Sep, 2012. <http://www.osti.gov/scitech/servlets/purl/1055611>.
- [23] H. T. Wong, “Ultra-Low-Energy Germanium Detector for Neutrino-Nucleus Coherent Scattering and Dark Matter Searches,” *Mod. Phys. Lett.* **A23** (2008) 1431–1442, [arXiv:0803.0033](https://arxiv.org/abs/0803.0033) [hep-ex].
- [24] H. T.-K. Wong, “Taiwan EXperiment On Neutrino,” *The Universe* **3** no. 4, (2015) 22–37, [arXiv:1608.00306](https://arxiv.org/abs/1608.00306) [hep-ex].

- [25] A.B. Balantekin and G.M. Fuller, “Supernova neutrino nucleus astrophysics,” *Journal of Physics G: Nuclear and Particle Physics* **29** no. 11, (2003) 2513. <http://stacks.iop.org/0954-3899/29/i=11/a=007>.
- [26] J. Beacom, “Neutrinos from the next galactic supernova,” in *Neutrinos in the new millennium. Proceedings, 23rd Johns Hopkins Workshop on current problems in particle theory, Baltimore, USA, June 10-12, 1999*, pp. 357–383. 1999. [arXiv:hep-ph/9909231](https://arxiv.org/abs/hep-ph/9909231) [hep-ph].
- [27] T. Fischer, S. C. Whitehouse, A. Mezzacappa, F.-K. Thielemann, and M. Liebendörfer, “Protoneutron star evolution and the neutrino-driven wind in general relativistic neutrino radiation hydrodynamics simulations,” *A&A* **517** (2010) A80.
- [28] Janka, H.-Th., “Conditions for shock revival by neutrino heating in core-collapse supernovae,” *A&A* **368** no. 2, (2001) 527–560.
- [29] T. Yamasaki and S. Yamada, “Standing Accretion Shocks in the Supernova Core: Effects of Convection and Realistic EOS,” *Astrophys. J.* **650** (2006) 291–298, [arXiv:astro-ph/0606504](https://arxiv.org/abs/astro-ph/0606504) [astro-ph].
- [30] H. A. Bethe, “Supernova mechanisms,” *Rev. Mod. Phys.* **62** (Oct, 1990) 801–866. <https://link.aps.org/doi/10.1103/RevModPhys.62.801>.
- [31] J. Blondin, A. Mezzacappa, and C. DeMarino, “Stability of standing accretion shocks, with an eye toward core collapse supernovae,” *Astrophys. J.* **584** (2003) 971–980, [arXiv:astro-ph/0210634](https://arxiv.org/abs/astro-ph/0210634) [astro-ph].
- [32] L. Wolfenstein, “Neutrino oscillations in matter,” *Phys. Rev. D* **17** (May, 1978) 2369–2374.
- [33] L. Wolfenstein, “Neutrino oscillations and stellar collapse,” *Phys. Rev. D* **20** (Nov, 1979) 2634–2635.
- [34] O. G. Miranda and H. Nunokawa, “Non standard neutrino interactions: current status and future prospects,” *New J. Phys.* **17** no. 9, (2015) 095002, [arXiv:1505.06254](https://arxiv.org/abs/1505.06254) [hep-ph].
- [35] M. Lindner, W. Rodejohann, and X.-J. Xu, “Coherent Neutrino-Nucleus Scattering and new Neutrino Interactions,” *JHEP* **03** (2017) 097, [arXiv:1612.04150](https://arxiv.org/abs/1612.04150) [hep-ph].
- [36] J. Dorenbosch *et al.*, “Experimental verification of the universality of electron-neutrino and muon-neutrino coupling to the neutral weak current,” *Physics Letters B* **180** no. 3, (1986) 303 – 307.
- [37] **Particle Data Group** Collaboration, J. Beringer *et al.*, “Review of Particle Physics,” *Phys. Rev. D* **86** (Jul, 2012) 010001.
- [38] D. Jaud, “Effective Field Theories.” Ludwig-Maximilians-University Munich, *unpublished*, 2012.

- [39] M. Schwartz, “Lecture 9 - Scalar QED.” Lecture notes, Harvard University, *unpublished*, 2009.
- [40] F. Mandl and G. Shaw, *Quantum Field Theory*. A Wiley-Interscience publication. Wiley, 1984. <https://books.google.be/books?id=pJQxmwEACAAJ>.
- [41] K. Krane, *Introductory Nuclear Physics*. Wiley, 1987. <https://books.google.be/books?id=ConwAAAAMAAJ>.
- [42] D. Vautherin and D. Brink, “Hartree-Fock Calculations with Skyrme’s Interaction. I. Spherical Nuclei,” *Phys. Rev. C* **5** (Mar, 1972) 626–647.
- [43] T. van Cuyck, “Short-range correlations and meson-exchange currents in neutrino-nucleus scattering.” University of Gent, *unpublished*, 2017.
- [44] N. Jachowicz, S. Rombouts, K. Heyde, and J. Ryckebusch, “Cross sections for neutral-current neutrino-nucleus interactions: Applications for ^{12}C and ^{16}O ,” *Phys. Rev. C* **59** (Jun, 1999) 3246–3255.
- [45] J. L. Herraiz, M. C. Martnez, J. A. Caballero, and J. M. Udas, “Overview of neutrino-nucleus quasielastic scattering,” *AIP Conference Proceedings* **1189** no. 1, (2009) 125–132.
- [46] V. Pandey, N. Jachowicz, T. Van Cuyck, J. Ryckebusch, and M. Martini, “Low-energy excitations and quasielastic contribution to electron-nucleus and neutrino-nucleus scattering in the continuum random-phase approximation,” *Phys. Rev. C* **92** (Aug, 2015) 024606.
- [47] T. Duguet, “Theoretical Nuclear Structure.” University of Leuven, *slides*, 2015.
- [48] D. Rowe, “Equations-of-Motion Method and the Extended Shell Model,” *Rev. Mod. Phys.* **40** (Jan, 1968) 153–166.
- [49] M. Tohyama, “Application of extended random-phase approximation with ground-state correlations to collective excitations of ^{16}O ,” *Journal of Physics: Conference Series* **529** no. 1, (2014) 012026. <http://stacks.iop.org/1742-6596/529/i=1/a=012026>.
- [50] M. Waroquier, “Hoger Aggregaatsthesis.” University of Gent, *unpublished*, 1982.
- [51] M. Waroquier, K. Heyde, and G. Wenes, “An effective Skyrme-type interaction for nuclear structure calculations,” *Nuclear Physics A* **404** no. 2, (1983) 269 – 297.
- [52] N. Schwierz, I. Wiedenhover, and A. Volya, “Parameterization of the Woods-Saxon Potential for Shell-Model Calculations,” [arXiv:0709.3525](https://arxiv.org/abs/0709.3525) [nucl-th].
- [53] G. Co’ and S. Krewald, “A model for particle emission induced by electron scattering,” *Nuclear Physics A* **433** no. 3, (1985) 392 – 426.
- [54] M. Wang *et al.*, “The AME2016 atomic mass evaluation (II). Tables, graphs and references,” *Chinese Physics C* **41** no. 3, (2017) 030003. <http://stacks.iop.org/1674-1137/41/i=3/a=030003>.

- [55] L. A. Ruso, *Neutrinos and their interactions in the Standard Model*, 2016. 52nd Winter School of Theoretical Physics, Ladek Zdroj, *slides*.
- [56] K. Scholberg, “COHERENT Neutrino Physics at the Spallation Neutron Source.” University of Virginia HEP seminar, Duke University, *slides*, 2014.
- [57] K. Scholberg, “SNOwGLoBES: SuperNova Observatories with GLoBES,” in *APS Meeting Abstracts*. Apr., 2011.
- [58] D. Papoulias and T. Kosmas, “Standard and Nonstandard Neutrino-Nucleus Reactions Cross Sections and Event Rates to Neutrino Detection Experiments,” *Adv. High Energy Phys.* **2015** (2015) 763648, [arXiv:1502.02928](https://arxiv.org/abs/1502.02928) [nucl-th].
- [59] C. Patrignani and P. D. Group, “Review of Particle Physics,” *Chinese Physics C* **40** no. 10, (2016) 100001. <http://stacks.iop.org/1674-1137/40/i=10/a=100001>.
- [60] E. Kolbe, K. Langanke, and P. Vogel, “Weak reactions on C-12 within the continuum random phase approximation with partial occupancies,” *Nucl. Phys.* **A652** (1999) 91–100, [arXiv:nuc1-th/9903022](https://arxiv.org/abs/nuc1-th/9903022) [nucl-th].
- [61] N. Jachowicz, K. Heyde, J. Ryckebusch, and S. Rombouts, “Continuum random phase approximation approach to charged-current neutrino-nucleus scattering,” *Phys. Rev. C* **65** (Jan, 2002) 025501.
- [62] G. Co’, “Random phase approximation and neutrino-nucleus cross sections,” *Acta Phys. Polon.* **B37** (2006) 2235–2242, [arXiv:nuc1-th/0605051](https://arxiv.org/abs/nuc1-th/0605051) [nucl-th].
- [63] N. Jachowicz, P. Vancraeyveld, P. Lava, C. Praet, and J. Ryckebusch, “Strangeness content of the nucleon in quasielastic neutrino-nucleus reactions,” *Phys. Rev.* **C76** (2007) 055501, [arXiv:0708.4135](https://arxiv.org/abs/0708.4135) [nucl-th].
- [64] M. Peskin and D. Schroeder, *An Introduction to Quantum Field Theory*. Advanced book classics. Avalon Publishing, 1995.
https://books.google.be/books?id=_H-oPv1raioC.
- [65] T. Duguet, “Course in Theoretical Nuclear Physics - KU Leuven *Preliminaries..*” Lecture notes, University of Leuven, *unpublished*, 2015.

DEPARTEMENT OF PHYSICS AND ASTRONOMY
Celestijnenlaan 200d bus 2412
3001 HEVERLEE, BELGIË
tel. + 32 16 32 71 24
fys.kuleuven.be

